POLITECNICO DI MILANO
DEPARTMENT OF CIVIL AND ENVIRONMENTAL ENGINEERING
DOCTORAL PROGRAM IN STRUCTURAL, SEISMIC AND
GEOTECHNICAL ENGINEERING

MODELLING AND SIMULATION OF PIEZOELECTRIC MICROMACHINED ULTRASONIC TRANSDUCERS

Doctoral Dissertation of:
Gianluca Massimino

Supervisors:
Prof. Alberto Corigliano
Prof. Raffaele Ardito

Tutor:
Prof. Attilio Alberto Frangi

The Chair of the Doctoral Program:
Prof. Umberto Perego

Cycle XXXII

Acknowledgements

The first acknowledgements go to the supervisors and tutor of the present thesis Professors Alberto Corigliano, Raffaele Ardito and Attilio Frangi. I'm really grateful for your support and collaboration.

Thanks to the company STMicroelectronics that fabricated the device I studied in this work. A very special thanks goes to Eng. Fabio Quaglia that gave me the possibility to meet and joint the MEMS design and characterization group for the experimental campaign, with which I really had enlightening discussions and always encouraged and empowered me in this work.

A big thanks to my family, colleagues and my friends. I'm so glad to have them close.

Abstract

Ultrasonography was the first and the most important civil ultrasound application appeared in the 1950s.

It is a non-invasive diagnostic technique, adopted to obtain images of human tissues by means of the principle of pulse-echo, that avoids the use of X-Rays scan, a technique that could be harmful because of the exposition to radiation.

Nowadays, array of several piezoelectric bulk wave resonators are employed in the commercial ultrasound imaging probes, in order to generate 3D real-time images. However, this technology is limited by the high probe manufacturing and material production cost.

Modern micromachining techniques allow for a much higher precision than the reticulation techniques, adopted for the fabrication of piezoelectric bulk ceramic elements and a more easily manageable fabrication of large 1D and 2D arrays that imply high resolution and real-time imaging capabilities, in spite of the very small amount of piezoelectric material.

Piezo-MEMS technology has revolutionized the actuators and sensors world, leading the micromachining and miniaturization advantages in the ultrasound systems.

Piezoelectric Micromachined Ultrasonic Tranducers (PMUTs), appeared in the first decade of the XXI century, consist of layered flexural plates with a piezoelectric thin film active layer, arranged in an array configuration, to emit and detect ultrasonic pressure waves. The possibility to replace the common piezoelectric bulk wave resonators with this novel technology, extremely increases the research interests in the study and the comprehension

of its capabilities.

The main purposes of the thesis regard the modelling and the simulation of the Piezoelectric PMUTs working behaviour, in order to deeply investigate the acoustic performances of this device. Several multiphysics numerical models predict the behaviour of the stand-alone diaphragm and the array of transducers.

The attention is focused on the effects of the residual stresses related to the fabrication process and the DC voltage bias, V_{DC}. They both play an important role in the determination of the starting deformed configuration and of the fundamental performing frequency, which are strongly affected by the geometric stiffness.

Additionally, the non-linear dynamic behaviour, due to the involved large displacements, is affected by the internal stress resultant and by the starting deflected configuration, as well. Subsequently, the non-linear response of the system changes with the imposed DC voltage bias. As a matter of fact, the PMUT center transversal oscillation shows a soft spring behaviour at V_{DC} equal to 2 V, while it becomes a hard spring response at V_{DC} equal to 12 V.

The effects of the protecting structure in the acoustic performance, are deeply investigated. To this purpose a 3D Finite Element (FE) model is used to study the role of the vibrating package on the pressure propagation, considering its elastic properties. Furthermore, the acoustic-structure interaction is imposed on the transducers acoustic interface and on the package surface boundaries, as well.

Different numerical modelling techniques are proposed to solve PMUTs problems, reporting the main features, advantages and drawbacks of each of them. The experimental and numerical comparisons are presented, in order to validate the numerical models, together with critical aspects and discussions on the electro-mechanical-acoustic coupled response of the device.

The comprehensive electro-mechanical-thermoacoustic 2D axisymmetric model of the single transducer, correctly captures the quality factor of the system. The 3D electro-mechanical-acoustic model successfully simulates the in frequency response of the device. Moreover, the proposed 3D acoustic vibrating piston-like array of transducers allow for the estimation of the in-time pressure field, by means of the common commercial FEM acoustics software.

Furthermore, a novel piezoelectric-acoustic coupled FE Model Order Reduction (MOR) technique is described and successfully implemented into a Fortran custom code, in order to obtain a Reduced Order Model

(ROM) of the PMUTs large array and to simulate the in-water response. To this purpose, the 11x11 PMUTs array transmitting (TX) phase and the 7x7 cluster of PMUTs receiving (RX) phase are simulated. The Reduced Order Model (ROM) custom code is characterized by extremely fast computational time with respect the hugely time-consuming standard full order FE approaches, implemented in the commercial software. Therefore, it represents a suitable tool to correctly evaluate the pressure propagation, the interference phenomena in the near-field and compute the response of the transducers in the actuation and sensing phases.

Contents

CHAPTER 1

Introduction

Micro-Electro-Mechanical-Systems (MEMS) [1] are complex devices with characteristic dimension of the order of micrometer. The first MEMS product was the accelerometer designed in 1979, at Stanford University. Engineers and scientists wanted to use some of the well controlled integrated circuits micromachining techniques to make movable mechanical structures at the micro scale, which could be connected to electronic circuits on the same chip. Subsequently, accelerometers become mainstream in the 1990s, as sensors to detect a crash for automotive airbag systems, where the mechanical and electronic portions were integrated on the same chip.

MEMS devices are able to measure accelerations [2], angular velocities [3], to detect pressure [4] and to provide the mechanical actuation in micro-actuators, micro-pumps [5] of inkjet print-heads or innovative Micromachined Ultrasonic Transducers (MUTs) for medical applications [6, 7]. Nowadays, MEMS are present in several smartdevices, in view of increasing the human-machine interaction [8], in energy harvesters [9] and medical diagnostic instruments [10].

In the framework of the MEMS physics, researchers are asked to solve problems involving different interacting coupled phenomena, in which the beauty and the complexity of this research field lies. The presented doc-

toral dissertation perfectly fits the goals of describing and predicting the behaviour of the Piezoelectric Micromachined Ultrasonic Transducers (PMUTs), appeared in the first decade of the XXI century, by means of mathematical modelling and simulation.

The thesis is organized as follows. Chapter 2 is devoted to the description of the ultrasound systems and the introduction of the state of the art of the micromachined ultrasonic transducers, together with the physical principles of the wave propagation and the pulse-echo on which the ultrasound scan is based.

In Chapter 3 the mathematical formulation of the linear piezoelectricity and acoustics are described. The attention is attracted to the equations that are implemented in the numerical PMUTs models.

Chapter 4 focuses on the air-coupled array of PMUTs performances. A proper multiphysics modelling via the Finite Element Method (FEM) is proposed for the stand-alone and the 4x4 array of transducers, by means of the commercial software COMSOL Multiphysics v5.2 and ANSYS v17.2.

In Chapter 5, the effects of the package on the acoustic performances are investigated through a 3D FEM ANSYS v17.2 numerical model for the complete packaged device. Different package geometries and configurations are proposed and deeply analysed.

In Chapter 6, the measured non-linearities in the dynamic behaviour of PMUTs and the effects of the DC bias voltage are shown. Hence, a COMSOL Multiphysics v5.2 numerical model is presented in order to simulate the non-linear vibrations by means of large displacements transient analyses in the presence of the acoustic coupled fluid. The acoustic performance of the complete device is, therefore, simulated through an only acoustic model in which a proper baffled piston modelling for the transducers is considered.

In Chapter 7, the mathematical reduced order technique for large PMUTs array is derived and implemented in a Fortran custom code. The effectiveness in the order reduction is studied and the comparison with the standard full order approach implemented in COMSOL Multiphysics v5.2 is shown. Applying the reduced model results in accurate and faster analyses. Indeed, the proposed numerical technique is applied to simulate the 11x11 PMUTs focusing transmitting (TX) phase and the 7x7 cluster of PMUTs in receiving (RX) phase.

In the end, Chapter 8 is devoted to closing remarks and conclusions on the studied PMUTs problems, together with possible future developments and works.

CHAPTER 2

Micromachined Ultrasonic Transducers (MUTs)

This chapter focuses on the description of the ultrasound systems and introduces the reader to the novel Micromachined Ultrasonic Transducers (MUT) devices based on the piezoelectric effect (Piezoelectric-MUTs also known as PMUTs) and the electrostatic interaction force (Capacitive-MUTs also known as CMUTs). Ultrasound scan is the most important medical diagnostic technique, appeared in the 1950s. Several ultrasound transducers are described, starting from the initial probes to the new MUTs used in ultrasound imaging and innovative applications, namely: fingerprint recognition and gesture recognition. The wave physical principles of pulse-echo and Time Of Flight (TOF), on which the spatial reconstruction is based, are presented according to the well known Snell-Descartes law. Subsequently, the working principle and concept-design of PMUTS and CMUT are described.

2.1 Ultrasound systems

Ultrasonic transducers are well known for their applications in medical ultrasonic imaging [11–13], exploiting the pressure propagation above 20 KHz inside the human tissue.

Ultrasonography was the first and the most important civil ultrasound application appeared in the 1950s. Before ultrasound scan, ultrasound pulses to echo-locate had been discovered by the British Board of Inven-

tion and Research in 1916 and exploited in the SONAR (SOund NAvigation and Ranging) instrument, developed for the ASDIC (Anti-Submarine Detection Investigation Committee) and started production in 1922, as submarine safety equipment called with the same acronym ASDIC.

Echography is a non-invasive diagnostic technique which is adopted to obtain images of human tissues by means of the principle of pulse-echo. Moreover, ultrasound sonography avoids the use of X-Rays scan, a technique that could be harmful if the patient were exposed to radiation for a long period.

The initial ultrasound imaging technique, appeared in the 1950s, was called A-mode (Amplitude mode) because the system was only able to provide a 1D information, associated with a thickness, based on the amplitude of the received echo. During the 1960s, the technique evolved towards the B-Mode (Brightness mode), where a probe consisting of an array of transducers scanned a part of the human body surface to get a 2D reconstruction, in which a gray-scale was adopted, where the intensity of the echo influences the brightness.

Several versions of probes, as shown in Fig. 2.1, are present on the market with different purposes. In fact, through the curved array probe (see Fig. 2.1 (b)) larger portions of tissue than the linear array probe in Fig. 2.1 (a) can be scanned. A second version of the B-mode, with the suffix RT (1970s), was based on the beamforming technique, by means of which the ultrasound propagation is focused in a small region of a proper focus with high intensity (refer to 2.1 (c)). The Doppler-Mode technique, introduced during the 1980s, generates images of the movement of tissues and body fluids (usually blood) through the Doppler effect implying the variation in frequency and wavelength. Moreover, to properly visualize the movement information, a velocity contour-map overlapped a B-mode image, consequently the technique was called Color Doppler-mode (1980s).

In the last ten years, new ultrasound probes (see Fig. 2.2) are coming, consisting of an array of transducers arranged in a 2D matrix and suitable imaging algorithms are available.

It is now possible generate 3D real-time images (sometimes called 4D) with satisfactory quality and fluidity. The 4D imaging techniques are currently devoted to few applications, as the in-time reconstruction of moving fetus presented in Fig. 2.3.

New standard probes exploit bulk wave resonator elements made of piezoelectric ceramics [14, 15]. However, the employment of this novel technique is mainly limited by development time and probe manufacturing cost. As a matter of fact, the ultrasound mechanical systems consist of sev-

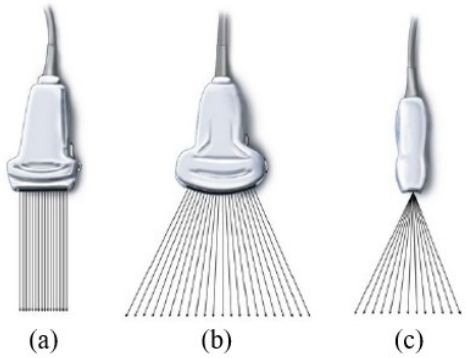

Figure 2.1: *Ultrasound probes: (a) linear array probe; (b) curved array probe; (c) phased array probe.*

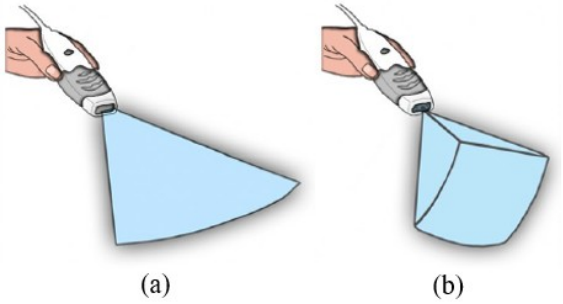

Figure 2.2: *Ultrasound probes: (a) 2D probe; (b) 3D probe.*

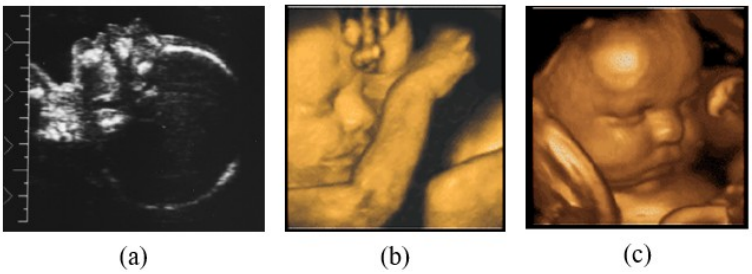

Figure 2.3: *Ultrasound fetus images: (a) 2D; (b) 3D; (c) 4D.*

eral inorganic compound bulk materials constituted of lead (Pb) zirconate (Zr) titanate (Ti) (PZT) [16], a material with a high production cost.

Nowadays, the discovery of novel microfabrication techniques allows for the introduction of piezoelectric thin films, namely PZT and aluminum nitride (AlN) and the fabrication of suspended structures large arrays. Modern micromachining techniques [17] allow for a much higher precision than the reticulation techniques adopted for the fabrication of bulk ceramic elements. Indeed, research activities and interest are mainly motivated by prospects of more easily managing the fabrication of large 1D and 2D arrays that would imply greater beam steering, focusing (phased array operation), high resolution and real-time imaging capabilities [18–20] in spite of the very small amount of piezoelectric material.

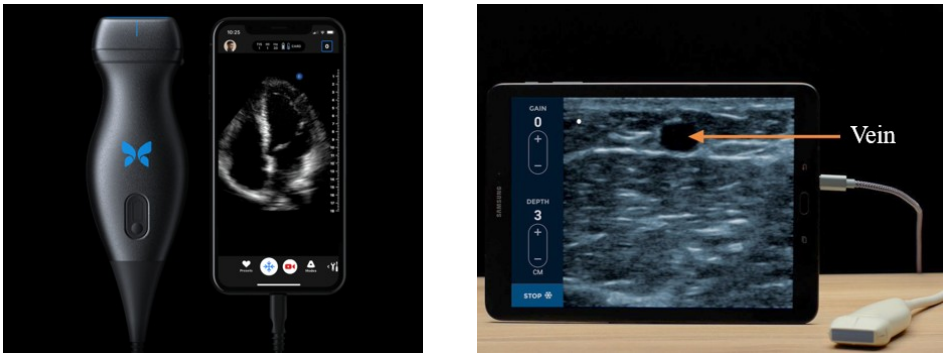

Figure 2.4: *MEMS-based ultrasound probes: Buttefly (left); EchoNous (right)*

Two examples of ultrasonic probes based on Micro-Electro-Mechanical-Systems (MEMS) are shown in Fig. 2.4.

More recently, this technology has been adopted to the fingerprint recognition, as safety device in smartphones (refer to Fig. 2.5 on the left) and gesture interpretation as reported in Fig. 2.5 on the right.

In this introductory chapter, the physical-based ultrasound principles and the common Micromachined Ultrasonic Transducers (MUTs) are briefly presented, focusing the attention on the Piezoelectric-MUTs, also known as PMUTs and the Capacitive-MUTs (CMUTs).

2.2 Physical ultrasound principles

The ultrasound identification and reconstruction technique merges the physical principles of pressure wave propagation with signal processing computation algorithms, based on the elaboration of the time between the acoustic emission and detection of the pressure pulses, called time of flight (TOF).


Figure 2.5: *MEMS-based ultrasound application: fingerprint recognition (left); gesture recognition (right)*

The goal of the ultrasound imaging [21] consists in internally inspecting the target and consequently providing a satisfactory image of the considered system. On the contrary, some ultrasound applications simply restrict their job to the identification of the distance between the transducer and the object (range-finders [22–25], gesture recognition [8, 26], fingerprint recognition [27, 28]).

2.2.1 Reflection, refraction and absorption

During the wave propagation, discontinuities in the material speed of sound imply the reflected and refracted waves. In fact, when the acoustic energy impinges on a discontinuity surface, it splits in two parts: the reflected one becomes the pressure echo of which the TOF is computed, the refracted one transmits inside the material with lower energy.

In Fig. 2.6 is sketched the Snell-Descartes law [29–31], governing the transmission and reflection, in which a plane wave hits a discontinuity plane surface with angle θ_i, between two material with sound velocities c_1 and c_2, and generates a reflected wave and a transmitted wave with angles respectively θ_r and θ_t. Hence, the well known equalities hold:

$$\theta_r = \theta_i$$
$$\left(\frac{\sin\theta_i}{c_1}\right) = \left(\frac{\sin\theta_t}{c_2}\right).$$

Going further, the quantity that characterizes the material ability to propagate the acoustic waves is called acoustic impedance and it is strictly related to the density ρ and speed of sound. In principle, the impedance is a complex quantity but for the plane wave propagation and far from the

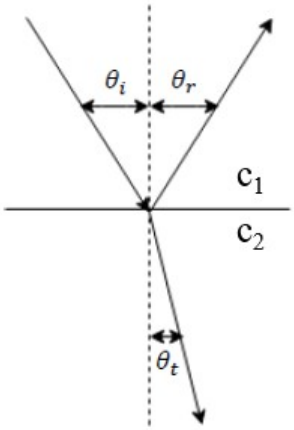

Figure 2.6: *Snell-Descartes law*

acoustic emitter (far-field), in which the imaginary part is negligible, the following expression holds

$$Z = \rho c$$

Values of the density, speed of sound and acoustic impedance are available in literature for several materials like human body tissues and fluids at different temperature [11]. The acoustic impedance ranges from 413 Rayl for air to $1.43 \cdot 10^6$ Rayl for water, at 20 °C and $3.75\text{-}7.38 \cdot 10^6$ Rayl for bones, with 1 Rayl = 1 Pa·s/m. Therefore, every times a pressure wave meets a discontinuity in the material density, meaning travelling in a heterogeneous domain, reflected and transmitted waves are generated. The described physical principles are exploited by ultrasound systems (see Fig. 2.7) in elaborating the coming back echos, each time the acoustic waves propagate through a non-homogeneous material and cross a discontinuity interface.

Hence, for the system sketched in 2.7, for human body ultrasonography, the distance Δx between the considered target and the emitting probe is estimated, by means of the so called principle of pulse-echo, as follows

$$\Delta x = \frac{c \cdot \Delta t}{2} \tag{2.1}$$

in which Δt is the waiting time between the emission and reception of the corresponding reflected wave. Values of the speed of sound c are reported in literature for several materials at different temperature. Typically, in human

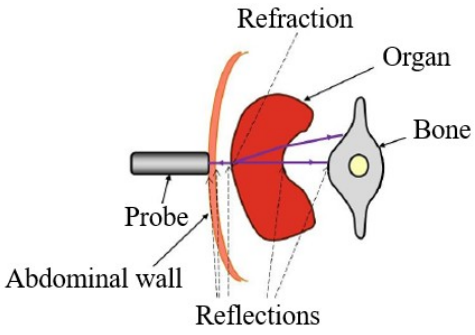

Figure 2.7: *Ultrasound propagation in human body [11]*

ultrasonography it is approximated to 1540 m/s which is close to 1546 m/s the value for sea water at 30 °C [32].

During the wave propagation in a homogeneous medium, part of the acoustic energy is transferred to the material and converted in heat, consequently temperature oscillations occur and the pressure amplitude attenuates with the covered distance. The described phenomenon is called absorption. Indeed, assuming a plane wave travelling along the direction x, according to the following absorptive exponential model [11], the pressure amplitude $P(x)$ behaves as

$$P(x) = P_0 \exp(-\alpha_1 f^y x)$$

where P_0 is the initial pressure amplitude at $x = 0$, f is the propagation frequency, α_1 and y absorption parameters depending on the material.

In Fig 2.8 the absorption factor $\alpha(f) = \alpha_1 f^y$ is reported for human blood, muscle and breast. The presented relation shows that the higher is the frequency content the higher is the attenuation in the pressure amplitude.

The presented physical phenomenon is directly related to the spatial resolution of the ultrasound system in terms of lateral resolution and axial resolution. In fact, axial resolution is defined as the minimum detected distance between two objects, placed along the propagation direction of the acoustic beam. While, lateral resolution is the minimum detected distance between two objects placed crosswise to the propagation direction of the acoustic beam.

In general, the spatial resolution increases with the decreasing of the wavelength, that means when the frequency of the transmitted wave increases and decreases if the attenuation in the material increases, which is several times associated with the increasing in frequency of the transmit-

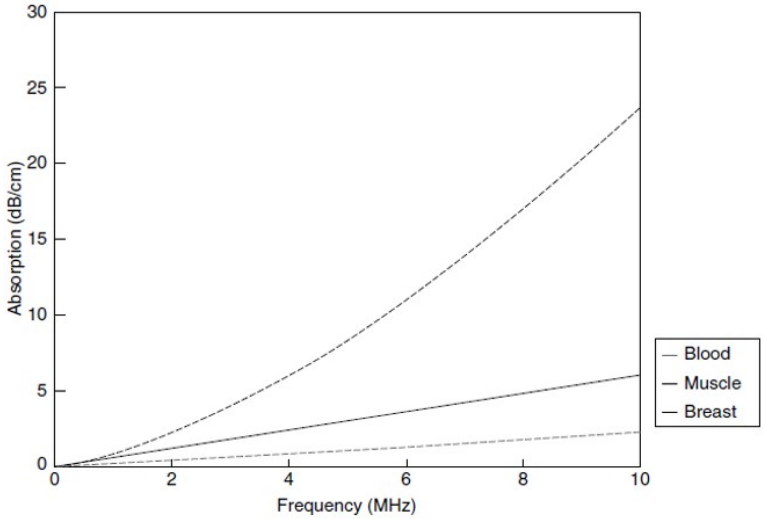

Figure 2.8: *Absorption factor [11]*

ted wave, as well. Hence, a compromise in the frequency content of the ultrasound emission, provided by the transducer and attenuation must be reached in view of the wanted spatial resolution.

2.3 Piezoelectric Micromachined Ultrasonic Transducers (PMUTs)

Piezoelectric Micromachined Ultrasonic Transducers (PMUTs) consist of layered flexural plates with a piezoelectric thin film active layer to actuate and detect the transversal vibrations. The frequency range of thin film bulk wave resonators is in the range of several hundreds of MHz to 10 GHz [33, 34], missing largely the range for ultrasound imaging, which is around 10 MHz [35, 36], and being impossible to use for in-air applications with frequency of the order of 100 kHz [23, 24]. A suspended flexural diaphragm is able to vibrate in the required range with high displacement amplitudes. Hence, the dome-shaped vibration of a resonating plate at the fundamental frequency couples well to a medium like water or air. Hereinafter, the principle of working is described, considering a circular laminated transducer with a PZT thin layer.

To actuate the vibration, the bending moment is provided by the electric field across the piezoelectric layer induced by the reverse piezoelectric effect due to the imposed alternate voltage difference between the electrodes ΔV. Conversely, when the system vibrates under a pressure load an electric field appears in the piezoelectric layer by means of the direct piezoelectric

effect and a voltage difference can be detected (see Fig. 2.9).

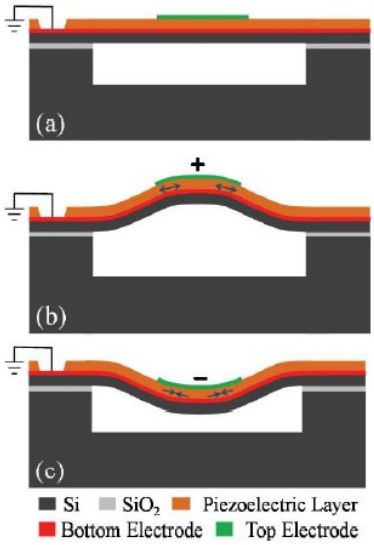

Figure 2.9: *PMUT cross-section: (a) rest configuration; (b) displacement due to $\Delta V > 0$; (c) displacement due to $\Delta V < 0$ [37].*

Considering a linear elastic laminated circular clamped diaphragm, shown in Fig. 2.10 with n-th thickness t_n, the fundamental resonance frequency is computed through the expression [38]

$$f_r = \frac{(3.19)^2}{2\pi a^2}\left(\frac{D}{\mu}\right)^{1/2}$$

where a is the radius, D is the laminate plate bending stiffness, depending on the neutral axis position z_s and elastic material properties of the layers and μ is the surface mass density depending on the volume mass density and thickness of the layers.

Arranging the transducers in a 2D matrix, implies the determination of the distance between the elements (pitch) according to the adopted scanning technique. The pitch of the ultrasound elements depends on either the required resolution or, if the beam steering technique is employed, on the space angle within which a unique solution for the radiation direction is attempted and no secondary lobes occur [32].

Usually, a standard pitch d is half the wavelength of the transmitted signal, $d = \lambda/2$. The presented solution is related to a unique emission direction in the half-space defined by the array plane. Indeed, considering a piston-like movement, the plate diameter is a direct proportional to the

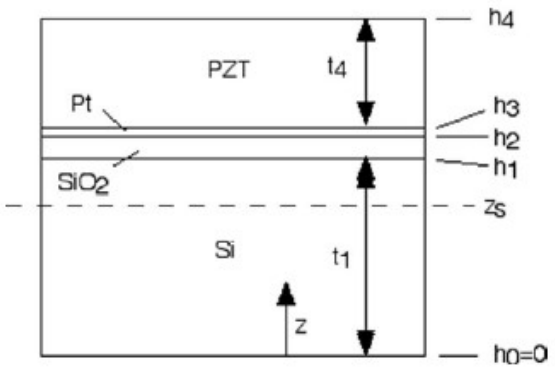

Figure 2.10: *PMUT layered cross-section [39].*

transmitted radiation power [32, 40]. Therefore, the $\lambda/2$ pitch requires that the diameter should follow a λ law, that means a $1/f$ law, whereby f is the frequency of the emitted wave. Hence, an ideal choice for beam steering is a diameter of $\lambda/2$.

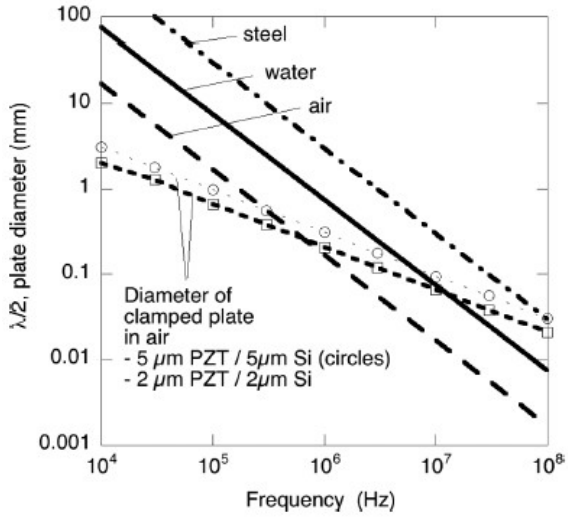

Figure 2.11: *Frequency-diameter relation of circular clamped PZT-Si plates compared to half the wavelength $\lambda/2$, with $\lambda = c/f$ (derived from speed of sound c and frequency f) wavelength of longitudinal waves in steel, air and water [39].*

The described relations are presented in Fig. 2.11, along with the diameter-frequency relation ($2a \propto \sqrt{f}$ law) of clamped plates. It is worth noting that, the frequency-dimension relations fit well to the 100 kHz–1 MHz range for in-air applications, which represents a suitable frequency range for short-

range airborne sensors. The matching zone with the waterline confirms that such transducers are potentially suited for 10-MHz medical applications.

Considering the case of the circular plate $\sqrt{D/\mu} \propto h$ and the fundamental resonance frequency behaves as $f_r \propto h/a^2$. Thus, both the radius and the frequency are defined by the application. Moreover, one needs to fit the thickness h of the diaphragm to achieve the two requirements on pitch and frequency. Additionally, given that the thickness ratio of PZT film and Si membrane are fixed for obtaining best electro-mechanical coupling [39], the design parameters are derived from the wanted application.

2.4 Capacitive Micromachined Ultrasonic Transducers (CMUTs)

Nowadays, Capacitive Micromachined Ultrasonic Transducers (CMUTs) are the most used and investigated MEMS devices for ultrasound applications. This technology consists of 2D array transducers made of a fixed metallic back plate (bottom electrode) and suspended structural laminated diaphragms, with a conductive layer (top electrode), defined by an air or vacuum closed cavity, as shown in Fig. 2.12 [41–43].

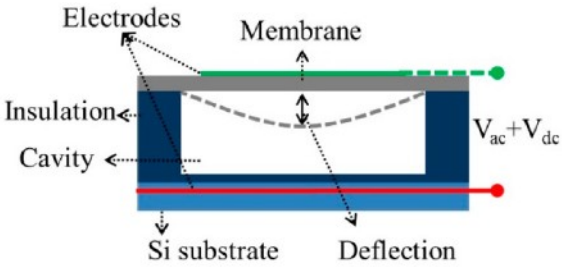

Figure 2.12: *CMUT cross-section [43].*

The transducer electrically works as a capacitor with finite dimensions and elastic stiffness. Considering the system in Fig. 2.13, under a voltage difference ΔV an electric field appears in the gap d between the two electrodes. Consequently, when the electric field is strong enough, the electrostatic force F_e deflects the diaphragm and the elastic restoring force F_s occurs. Hence, during the deformation the gap changes and the capacitance of the system varies as well, being defined as $C = \varepsilon_0 A/(d-z)$, where ε_0 is the dielectric permittivity of the vacuum and A is the plate area. In fact, in the transmitting phase, an alternate voltage difference is enforced between the electrodes, generating an alternate electric field and the diaphragm vibrates.

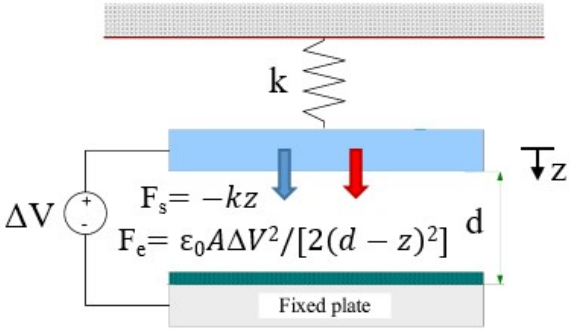

Figure 2.13: *1 dof CMUT model [1].*

Conversely, in the receiving phase, the pressure echo wave on the fluid-structure interaction surface acts as a mechanical load applied to the suspended plate inducing the vibration and as a consequence the gap and the capacitance variations. Usually, a DC voltage difference between the electrodes is imposed in order to generate a DC electric field, as a result of which the plate oscillates around a deformed reference configuration increasing the transmission performances [44].

CHAPTER 3

Linear piezoelectricity and acoustics

In this chapter the basic notions on piezoelectric materials and acoustics are presented. The PZT crystalline structure and the properties of the acoustic perturbations are discussed. Going further, the attention is focused on the linear mathematical model of piezoelectricity and the acoustics equations involved in the PMUT numerical models.

3.1 Piezoelectric materials

Piezoelectric materials are able to transform the mechanical energy in electric (direct piezoelectric effect) energy and vice versa, the electric energy in mechanical one (converse piezoelectric effect) [45]. They are hugely used as a transducer which produce charge (voltage) at the electrodes under the effect of mechanical stress. The latter behaviour is usually employed in inertial sensors (e.g. accelerometers, gyroscopes) [46] to detect the motion. Conversely, other applications include strain sensors, in which the change in length implies a voltage (current) output of piezoelectric gauges or micropumps and microphones [5, 47, 48], where the acoustic pressure wave excites piezoelectric diaphragms, as it occurs in PMUT.

Piezoelectricity is due to the particular crystalline structure of such materials characterized by asymmetric ions or charged molecular groups. Some piezoelectric materials, as PZT, belong to the class of ferroelectric materials which show a spontaneous polarization under the so called Curie temperature.

PZT is the most widely used ferroelectric material due to the high piezoelectric coefficients [49]. It is an oxide of lead, zirconium and titanium disposed in a Perovskite crystalline structure, shown in Fig. 3.1 on the left.

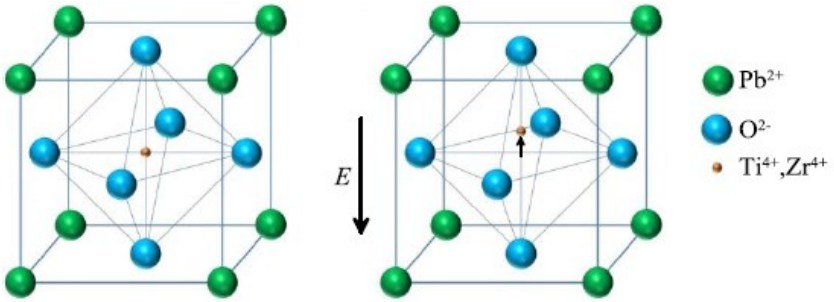

Figure 3.1: *Perovskite crystalline lattice of lead zirconate titanate (PZT) (left), effect of a enforced electric field (right).*

However, without any electric external field, internal dipoles are randomly oriented, consequently the total polarization is null. Imposing an external electric field, results in the reorientation of the electric dipoles and a global polarization occurs, due to the relative displacement of the positive ion of titanium with respect to the surrounding negative oxygen atoms (see Fig. 3.1 on the right).

3.1.1 Linear piezoelectricity: mathematical model

Let us consider a piezoelectric body Ω with volume mass density ρ, according to the standard piezoelectric notation [45], subjected to the acceleration $\ddot{\boldsymbol{u}}$ under the volume force $\boldsymbol{F}$ and the imposed traction $\boldsymbol{f}^D$ on the loaded surface S_T, the mechanical response follows the dynamic equations

$$\nabla \cdot \boldsymbol{T} + \boldsymbol{F} = \rho \ddot{\boldsymbol{u}} \qquad \text{in} \quad \Omega \tag{3.1}$$

$$\boldsymbol{T}\boldsymbol{n} = \boldsymbol{f}^D \qquad \text{on} \quad S_T \tag{3.2}$$

where, $\boldsymbol{n}$ is the outward normal on $\partial\Omega$ and $\boldsymbol{T}$ the second order stress tensor.

While, the deformation follows the well known compatibility relations

$$\boldsymbol{S} = \text{sym}(\nabla \boldsymbol{u}) \qquad \text{in} \quad \Omega \tag{3.3}$$

$$\boldsymbol{u} = \boldsymbol{u}^D \qquad \text{on} \quad S_u \tag{3.4}$$

in which $\boldsymbol{S}$ is the second order strain tensor and $\boldsymbol{u}^D$ are the displacement imposed data on S_u.

In the same domain Ω, the electric response follows the electrostatic relations, under the effects of the volume charge distribution ρ_c and surface charge distribution q_c on S_q

$$\nabla \cdot \boldsymbol{D} = \rho_c \qquad \text{in} \quad \Omega \tag{3.5}$$

$$\boldsymbol{D}\boldsymbol{n} = -q_c \qquad \text{on} \quad S_q \tag{3.6}$$

where, $\boldsymbol{D}$ is the electric displacement vector.

Moreover, for the conservative electrostatic field $\boldsymbol{E}$ is defined an electric potential φ and the expressions hold

$$\boldsymbol{E} = -\nabla \varphi \qquad \text{in} \quad \Omega \tag{3.7}$$

$$\varphi = \varphi^D \qquad \text{on} \quad S_\varphi. \tag{3.8}$$

Hence, in the framework of the mathematical description of the linear piezoelectricity, the electro-mechanical coupled constitutive model, in the so called stress-charge form, is presented

$$\boldsymbol{T} = \mathbf{C} : \boldsymbol{S} - \mathbf{e}^T \cdot \boldsymbol{E} = \mathbf{C} : \boldsymbol{S} + \mathbf{e}^T \cdot \nabla \varphi \qquad \text{in} \quad \Omega \tag{3.9}$$

$$\boldsymbol{D} = \mathbf{e} : \boldsymbol{S} + \boldsymbol{\varepsilon} \cdot \boldsymbol{E} = \mathbf{e} : \boldsymbol{S} - \boldsymbol{\varepsilon} \cdot \nabla \varphi \qquad \text{in} \quad \Omega \tag{3.10}$$

where $\mathbf{C}$ is the forth order elastic stiffness tensor at constant $\boldsymbol{E}$, $\boldsymbol{\varepsilon}$ is the second order dielectric permittivity tensor at constant $\boldsymbol{S}$ and $\mathbf{e}$ is the third order piezoelectric coupling tensor. Moreover, let $\boldsymbol{g}_j$ be the base vectors of the Cartesian 3D space, if $\mathbf{e} = e_{kij}\boldsymbol{g}_k \otimes \boldsymbol{g}_i \otimes \boldsymbol{g}_j$ then $\mathbf{e}^T$ is defined as the tensor $\mathbf{e}^T = e_{kij}\boldsymbol{g}_j \otimes \boldsymbol{g}_i \otimes \boldsymbol{g}_k$.

The presented linear piezoelectric model is adopted in chapter 7 in the mathematical formulation the reduced order piezoelectric problem model.

3.2 Acoustics

Acoustic waves consist of pressure small fluctuations that can propagates in a compressible fluid. Such pressure fields of moderate intensity can be generated by a moving object, like a vibrating speaker membrane that emits

sound in a concert room. Additionally, there are also ultrasonic (over 20 kHz) and infrasonic waves (below 20 Hz) whose frequencies lie beyond the limits of hearing. In compressible fluids any density variation is associated with a pressure variation that transmits to the other parts of the fluid, generating alternate compression and rarefaction regions [50]. Therefore, the result is the so called acoustic wave perturbation.

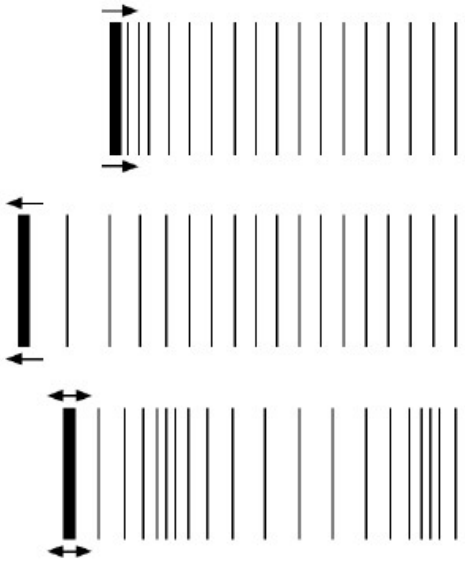

Figure 3.2: *Acoustic radiation in a fluid: compression region with concentration of lines, rarefaction region with dispersion of lines [50].*

As already, presented in chapter 2, acoustic perturbations are subjected to well known waves phenomena as transmission, reflection, absorption, dispersion and diffraction.

Hereinafter, the mathematical formulation of the acoustic problem for the pressure field, deeply described in the author's master thesis [51], is described together with the acoustic-structure interaction (ASI) conditions, largely used in the PMUT numerical modelling in the following chapters.

3.2.1 Linear acoustics: mathematical model

Let us consider a non-dissipative simple fluid Ω [29], with volume density ρ, moving with velocity $\boldsymbol{v}$ subjected to zero body forces and heat sources,

the conservation laws of mass, linear momentum and energy hold

$$\frac{\partial \rho}{\partial t} + \nabla(\rho \boldsymbol{v}) = 0 \qquad \text{in} \quad \Omega \tag{3.11}$$

$$\rho\left(\frac{\partial \boldsymbol{v}}{\partial t} + \boldsymbol{v}\cdot\nabla\boldsymbol{v}\right) + \nabla p = 0 \qquad \text{in} \quad \Omega \tag{3.12}$$

$$T\rho\left(\frac{\partial s}{\partial t} + \boldsymbol{v}\cdot\nabla s\right) = 0 \qquad \text{in} \quad \Omega \tag{3.13}$$

where, t is the time, p is acoustic pressure, T the temperature and s the specific entropy of the system.

Let us consider a neighborhood of a homogeneous rest reference configuration, the following equalities hold

$$\rho^0 = \text{const}, \quad \boldsymbol{v} = \boldsymbol{0}, \quad p^0 = \text{const}, \quad T^0 = \text{const}, \quad s^0 = \text{const}.$$

Let the first order variations in a neighborhood of the reference configuration of the acoustic quantities be

$$\rho^1, \quad \boldsymbol{v}^1, \quad p^1, \quad T^1, \quad s^1$$

such that,

$$\rho = \rho^0+\rho^1, \quad \boldsymbol{v} = \boldsymbol{v}^0+\boldsymbol{v}^1, \quad p = p^0+p^1, \quad T = T^0+T^1, \quad T = T^0+T^1.$$

in which the higher order terms are omitted for sake of brevity.

Developing (3.11) and truncating the expansion to the first order, the linear acoustics conservation equations are derived:

$$\frac{\partial \rho^1}{\partial t} + \rho^0\nabla\boldsymbol{v}^1 = 0 \qquad \text{in} \quad \Omega \tag{3.14}$$

$$\rho^0\frac{\partial \boldsymbol{v}^1}{\partial t} + \nabla p^1 = 0 \qquad \text{in} \quad \Omega \tag{3.15}$$

$$T^0\rho^0\frac{\partial s^1}{\partial t} = 0 \qquad \text{in} \quad \Omega \tag{3.16}$$

Hence, from (3.16) we get the isentropic fundamental property of the acoustic perturbation in a simple non-dissipative fluid, which means

$$s^1 = \text{const} \qquad \forall \text{t}.$$

Furthermore, the thermodynamic state equations are reported

$$\rho^1 = \chi_s^0\rho^0 p^1 \tag{3.17}$$

$$T^1 = \frac{\alpha_p^0 T^0}{C_p^0\rho^0}p^1 \tag{3.18}$$

where, C_p^0 is the specific heat and α_p^0 is the expansivity at constant pressure, $\chi_s^0 = 1/\kappa_s^0$ is the compressibility modulus, as the inverse of the bulk modulus κ_s^0 at constant specific entropy, computed at the reference state.

For sake of brevity, in order to present the wave equations for the acoustic quantities, the superscript 1 indicating the first variation, is omitted everywhere.

As the state relations (3.17) and (3.18) suggest, the density and the temperature variations are linearly proportional to the pressure variation p which represents the main acoustic field.

Therefore, taking $-\frac{\partial}{\partial t}$(3.14) + $\nabla\cdot$(3.15) the wave equation for the acoustic pressure is derived

$$-\frac{1}{c^2}\frac{\partial^2 p}{\partial t^2} + \nabla^2 p = 0 \qquad \text{in} \quad \Omega \tag{3.19}$$

in which the coefficient c corresponds to the wave velocity of sound, and the equality holds

$$c = \sqrt{\frac{\kappa_s^0}{\rho^0}}.$$

Furthermore, after some mathematical manipulations, the wave equation for the acoustic velocity fluctuation is presented

$$-\frac{1}{c^2}\frac{\partial^2 \boldsymbol{v}}{\partial t^2} + \nabla^2 \boldsymbol{v} = 0 \qquad \text{in} \quad \Omega. \tag{3.20}$$

In the end, (3.17) and (3.18) imply the wave propagation in terms of the first variations of density ρ and temperature T, as follows

$$-\frac{1}{c^2}\frac{\partial^2 \rho}{\partial t^2} + \nabla^2 \rho = 0 \qquad \text{in} \quad \Omega \tag{3.21}$$

$$-\frac{1}{c^2}\frac{\partial^2 T}{\partial t^2} + \nabla^2 T = 0 \qquad \text{in} \quad \Omega. \tag{3.22}$$

Dealing with the ASI problem, the coupling is due to the continuity of the normal stress and acceleration on the interaction surface S_p, with outward normal $\boldsymbol{n}$ for the fluid domain. Hence, the described condition is obtained by means of the equality

$$\nabla p \cdot \boldsymbol{n} = -\rho^0 \ddot{\boldsymbol{u}} \cdot \boldsymbol{n} \qquad \text{on} \quad S_p \tag{3.23}$$

$$-\boldsymbol{T}\boldsymbol{n} = p\boldsymbol{n} \qquad \text{on} \quad S_p \tag{3.24}$$

in which $\boldsymbol{T}$ and $\boldsymbol{u}$ are respectively the stress tensor and the displacement of the moving interacting structure [29].

Moreover, in the case of a perfectly rigid acoustic boundary S_{HW}, it is straightforward to deduce the relation

$$\nabla p \cdot \boldsymbol{n} = 0 \qquad \text{on} \quad S_{HW}. \tag{3.25}$$

which, is called hard wall condition.

Furthermore, the acoustic propagation into an infinite fluid medium is simulated enforcing the first order absorbing boundary condition (ABC) on S_{ABC} [52]

$$\nabla p \cdot \boldsymbol{n} = -\frac{1}{c}\frac{\partial p}{\partial t} \cdot \boldsymbol{n} \qquad \text{on} \quad S_{ABC}. \tag{3.26}$$

A simple verification shows that any travelling outward pressure wave, exactly respects (3.26). As a consequence, no reflected wave arises and the impinging waves are absorbed.

The mathematical models described in this chapter for the piezoelectricity and acoustics, along with the interaction conditions (3.24), (3.23) and infinite radiation (3.26), have been implemented in the PMUTs numerical models, presented throughout the work.

CHAPTER 4

Air-coupled array of PMUTs

In this chapter a multiphysics modelling via the finite element method of an air-coupled array of piezoelectric micromachined ultrasonic transducers and its experimental validation are presented. Two numerical models are described for the single transducer, axisymmetric and 3D, with the following features: the presence of fabrication induced residual stresses, which determine a non-linear initial deformed configuration of the diaphragm and a substantial fundamental mode frequency shift; the multiple coupling between different physics, namely electro-mechanical coupling for the piezo-electric model, thermo-acoustic-structural interaction and thermo-acoustic-pressure interaction for the waves propagation in the surrounding fluid.
The model for the single transducer is enhanced considering the full set of PMUTs belonging to the silicon die in a 4x4 array configuration.
The results of the numerical multiphysics models are compared with experimental ones in terms of the initial static pre-deflection, of the diaphragm central point spectrum and of the sound intensity at 3.5 cm on the vertical direction along the axis of the diaphragm.

4.1 Introduction

The present chapter deals with array of PMUTs, used for emitting and receiving ultrasonic waves [37, 53, 54]. They are widely employed in several applications: medical acoustic imaging [55, 56], underwater communications and hydrophones exploit the in-water wave propagation of ultrasonic

pulses [7, 57, 58]; finger-printing recognition [28] and range-finders use the in-air propagation [23, 24, 59–61]. Further applications are represented by non-destructive testing [62], velocity sensing [63, 64] and 3D obstacle recognition [65, 66].

Some of the results, shown herein, have been published in a previous work [67] and deal with an array of circular transducers with operating frequency of 100 kHz [68] for in-air application. The piezoelectric active layer is made of lead (Pb) zirconate (Zr) titanate (Ti) (PZT), and it is deposited with Sol-Gel technique [69–71] in circular configuration over the structural part of the diaphragm [36]. The most common air-coupled PMUTs in literature are characterized by operating frequency above 200 kHz: the difference in the operating frequency introduces many challenges due to the non-linearities activated by the high aspect ratio of the considered diaphragm.

The primary focus consists of a proper multiphysics Finite Element (FE) modeling of both the electro-mechanical and the acoustic behaviour of the PMUT [72]. The model gives a realistic estimation of the fundamental frequency and of the PMUT's quality factor through the adoption of large deformation analyses and by means of thermo-viscous modelling of the air, that induce the power dissipation in the so-called boundary layer at the fluid-structure interface.

The chapter is organized as follows. In section 2, the behaviour of a single circular fully-clamped diaphragm in an air-filled closed cylindrical cavity is analysed, while in the third section, 3D models are shown for the case of 4x4 transducers array. In section 4, to validate the numerical predictions for the single transducer, experimental tests are described and results are shown in the mechanical and in the acoustic domains. In the subsequent section 5, the numerical results for the array of PMUTs in parallel actuation are presented, compared with the single transducer ones. Finally, closing remarks are collected in section 6.

4.2 Numerical modelling for the single transducer

In this section three different numerical finite elements models related to the single PMUT are presented, built with COMSOL Multiphysics v5.2 and Ansys v17.2. The former is adopted for preliminary investigations using a 2D model, while the latter is used for more burdensome 3D analyses [55].

The diaphragm is depicted in Fig. 4.1: it has radius of 440 μm and an overall thickness equal to 8 μm, so that the diameter/thickness ratio is 110. The structural layer is made of silicon with thickness equal to 4.25 μm. The

piezoelectric active layer is made of PZT: it has thickness of 1 μm and is in a circular configuration with radius of 308 μm, coaxial with the diaphragm. The layered disc is clamped over an air-filled closed cylindrical cavity [55] with height of 400 μm and the same radius of the upper diaphragm. In all the considered models, the boundary conditions of the diaphragms are modelled in the most realistic way: in fact, the models incorporate a substantial portion of the silicon die which includes the PMUTs and the diaphragms are built in the die, in complete agreement with the fabrication process.

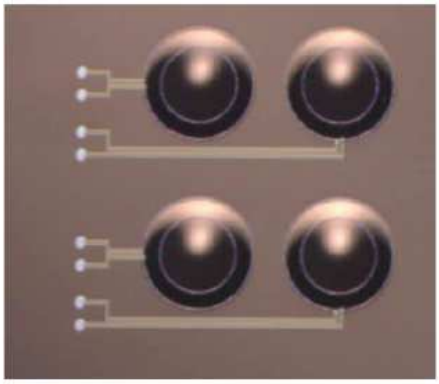

Figure 4.1: *Optical microscope image of four PMUTs belonging to the silicon die.*

The COMSOL model exploits the axial symmetry of the problem, to reduce the computational burden and to simulate the complete behaviour in the static and dynamic frequency regime of the stand-alone transducer surrounded by the fluid.

This numerical model, shown in Fig. 4.2, incorporates four physics and their mutual interactions, presented in chapter 3, namely: solid mechanics model of the diaphragm, piezoelectric effect in the PZT active layer, thermo-viscous acoustic model for the fluid near to the vibrating diaphragm and pressure acoustic model for the fluid far from the diaphragm. The layered plate includes not only the structural layer, made of silicon, and the active part, but also all the other layers that are introduced for fabrication purposes and, most importantly, the upper and lower electrodes on the two surfaces of the piezoelectric thin film. Each layer of the PMUT is considered as linear elastic and it is characterized by a certain amount of prestress acting in the radial direction of its plane, induced by the fabrication processes. Such residual stresses are introduced in the form of an initial non-equilibrated field. In the preliminary step of the analysis, the equilibrium equations are enforced iteratively, finally yielding the pre-deformed

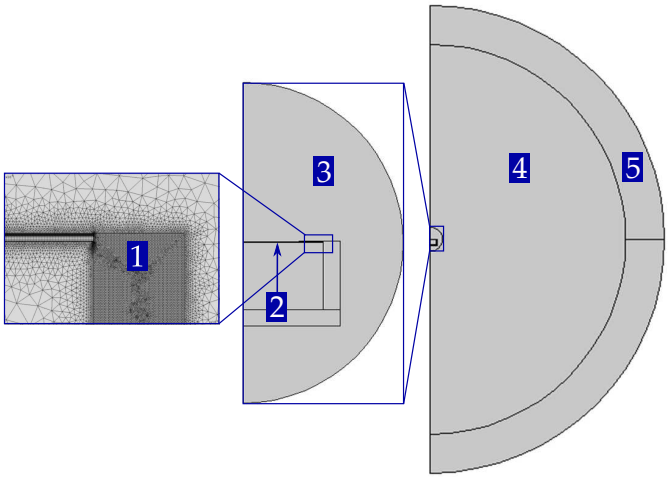

Figure 4.2: *COMSOL Multiphysics v5.2 axisymmetric model for the stand-alone transducer: solid domain (1) and mesh detail at the wet boundaries, electro-mechanical domain (2), thermo-acoustic domain (3), acoustic domain (4), perfectly matched layer (5).*

state of the diaphragm (clearly visibile in the optical microscope image reported in Fig. 4.1). The residual stresses are highly heterogeneous in the various layers, with different magnitude and sign.The silicon layer is the only one that presents a negligible initial stress. In the piezoelectric active layer the electro-mechanical coupling is enforced through linearized constitutive relations [1]. Furthermore, to take into account the structural damping effect (which incorporates the anchor losses, the surface and interface dissipation and the thermo-elastic losses) an isotropic structural loss factor is introduced.

The laminate system plus the cavity are inserted into a spherical thermo-viscous domain of radius equal to the wavelength $\lambda = c/f_0$, where $c = 343$ m/s is the sound velocity in the air at the reference state of $T_{ref} = 293.15$ K, $P_{ref} = 1$ atm and f_0 is the operating frequency of the system. This frequency coincides with the diaphragm fundamental eigenfrequency to maximize the acoustic efficiency for the case of the stand-alone transducer.

In the spherical thermo-acoustic domain, the full set of equations for a compressible viscid thermally conductive fluid are solved, namely: the momentum balance equation, the mass balance equation and the energy balance equation. It is necessary to adopt such a modelling for the fluid surrounding the vibrating diaphragm due to the fact that the maximum amplitude of vibration is comparable to the thickness of the diaphragm and to the viscous penetration depth at the operating frequency [73–75]. In such a way, the model gives an estimation of the fluid losses acting in the

boundary layers above and below the oscillating diaphragm together with the complete fluid-structure interaction for the wet boundaries.

The acoustic phenomenon far from the emitting source can be simplified by neglecting the thermo-viscous behaviour, thus reducing the governing relations to the Helmholtz equation. To reduce the degrees of freedom of the complete system, a spherical pressure acoustic domain of thickness 4λ has been modelled outside the thermo-viscous one. In this region, the lossy Helmholtz equation for the pressure acoustic field is solved, considering the attenuation properties of the fluid through the Stokes' attenuation factor for the viscous and thermally conductive case [40].

Finally, outside the pressure acoustic domain, a Perfectly Matched Layer (PML) of thickness equal to λ has been inserted, in order to simulate the wave radiation into an infinite medium.

The Ansys models are referred to a more realistic situation, characterized by a single transducer belonging to the silicon die that is glued onto a FR4 PCB board. This means that the axial symmetry is lost and a 3D model is considered. The first of the two Ansys models, shown in Fig. 4.3, describes the device sourrounded by the fluid and is characterized by a double symmetry condition on the two vertical planes of the system. The solid domain has been inserted into a spherical pressure acoustic domain of radius 3λ. The fluid-structure interaction is enforced by means of the continuity of the normal stresses and of the normal velocities at the wet boundaries. The damping effect for the structural oscillating diaphragm is taken into account through the introduction of the non-dimensional damping ratio defined by the inverse of twice the quality factor. Furthermore, the absorbing boundary condition is modelled by means of the Sommerfeld radiation condition at the external spherical surface of the fluid domain, to simulate the radial wave transmission into an infinite medium.

The second Ansys model builds up on the first one and it is characterized by a hard wall condition, which is necessary to simulate the operating configuration of the transducer connected to a smart device through its PCB board (refer to Fig. 4.4). In this case, the wave transmission occurs into a hemispherical pressure acoustic domain of radius 3λ, while the radiation into an infinite domain is due to the enforced absorbing boundary condition at its external surface.

The most important difference between the COMSOL and the Ansys modelling is about the dissipative behaviour of the fluid surrounding the solid domain. In the 2D axisymmetric COMSOL model for the stand-alone transducer a complete fluid-structure interaction is enforced, solving the linearized Navier-Stokes equations with the thermo-viscous description of

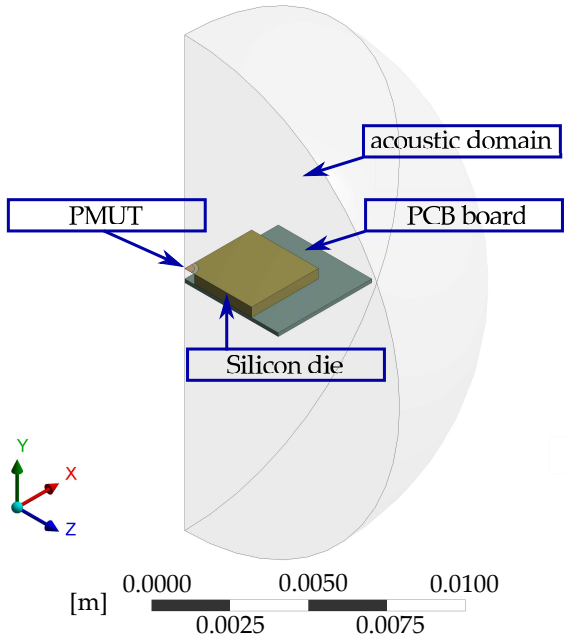

Figure 4.3: *3D double symmetric Ansys model for the quarter of single transducer belonging to the silicon die.*

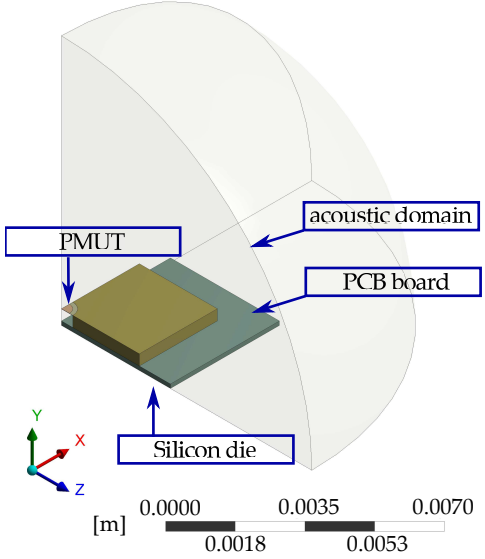

Figure 4.4: *3D double symmetric Ansys model for the quarter of single transducer in the operating configuration belonging to the silicon die.*

the fluid. Such a numerical modelling gives us the amount of power dissipation amplitude for the considered entropic process. In the Ansys model the 2D axisymmetric hypothesis has been removed, adopting a 3D description for the system. In such a way, the presence of the silicon die onto the PCB board has been taken into account providing a more accurate model. In this case, the fluid-structure interaction is enforced in a simplified manner by means of the vibro-acoustic coupling considering an inviscid fluid. Thus, the damping effects are modelled enforcing the damping ratio of the solid domain, keeping the same quality factor for the two models.

In all cases, the numerical electro-structural-acoustic frequency response is computed after a sequence of simulations, described in the following. An initial non-linear solid mechanics static analysis is performed to provide the pre-deflected configuration induced by the fabrication residual stresses. This analysis is necessary due to the high aspect ratio of the diaphragm. It is worth noting that the non-linearity is restricted to the geometric effects, while the materials behave in a linear fashion. At the end, an electro-mechanical-acoustic analysis is performed in the frequency domain [76,77] to simulate the behaviour of the entire system, under the harmonic voltage perturbation, account taken of the geometric non-linearities introduced before. This final step aims at the simulation of the small vibrations around the pre-stressed reference configuration. Therefore, a linear analysis is carried out, with the effect of geometric stiffness.

4.3 Numerical modelling for the 4x4 array of transducers

The Ansys model for the single transducer in the operating condition (refer to Fig. 4.4) is enhanced considering the full set of transducers belonging to the silicon die. The considered device is composed of 4x4 PMUTs organized in an array configuration with two orthogonal axes of symmetry. Such an arrangement allows us to model just a quarter of the system in the 3D space, shown in Fig. 4.5, using the symmetry conditions on the two vertical planes. The non-dimensional damping ratio has been enforced for the four vibrating transducers, and the absorbing boundary condition has been kept on the external surface of the fluid domain to ensure the infinite radiation.

Finally, in this case study, the transmitting phase can be simulated actuating in parallel the vibration of each transducer, applying the same voltage perturbation at the top electrodes of the piezoelectric layer and keeping the bottom ones at the common ground.

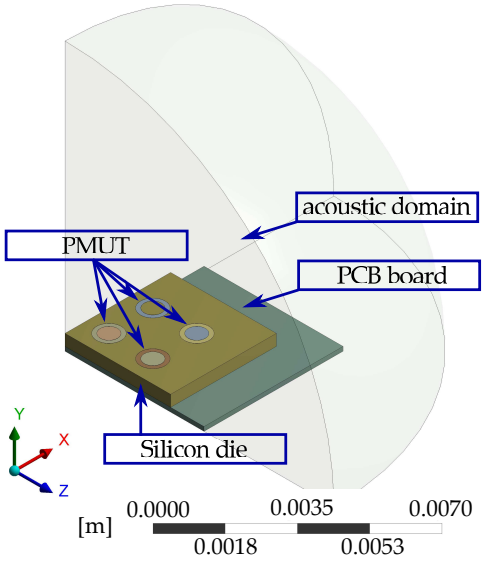

Figure 4.5: *3D double symmetric Ansys model for the quarter of array of transducers in the operating configuration belonging to the silicon die.*

4.4 Results and experimental validation for the single transducer

The results of the first study described in the previous section are presented in Fig. 4.6. The experimental initial static deflection of the layered system, due to residual stresses, is characterized by a maximum vertical displacement in the center of the diaphragm equal to 5.2 μm. The displacement measurements are executed via the Polytec MSA-500 Micro System Analyzer. The corresponding numerical value is 4.90 μm for the COMSOL model and 4.85 μm for the Ansys one. The mismatch is attributed to the uncertainty in the values of the residual stresses. In addition to the initial deformed shape, the residual stresses have another important effect: their contribution to the geometric stiffness of the diaphragm changes significantly the fundamental natural frequency of the PMUT. The same vibrating system in terms of geometry and materials, without the pre-stress state, shows a theoretical value for the fundamental natural frequency of 111.5 kHz, while taking into account the pre-stress state it shifts to 99.8 kHz, which is correctly captured by all the numerical models which reports a value of 100.0 kHz. To demonstrate the shift, a frequency sweep is carried out with a harmonic perturbation voltage amplitude of 3 V. A parametric analysis is introduced with the purpose of investigating the effect of resid-

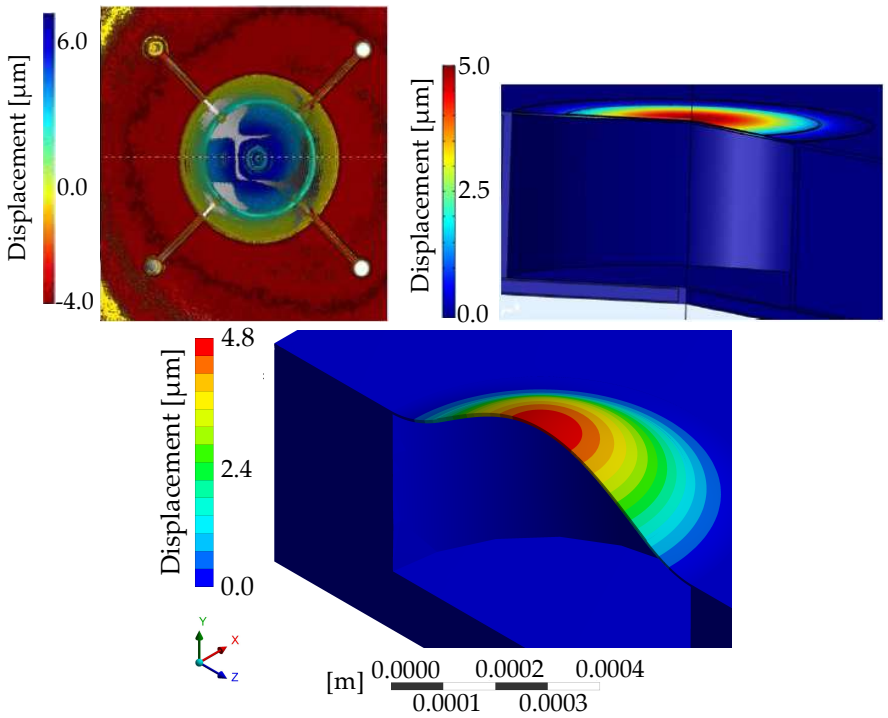

Figure 4.6: *Initial static deflection due to fabrication residual stresses in µm: experimental measurement by means of Polytec MSA-500 (above left), numerically computed by means of COMSOL Multiphysics v5.2 (above right), numerically computed by means of Ansys v17.2 (below).*

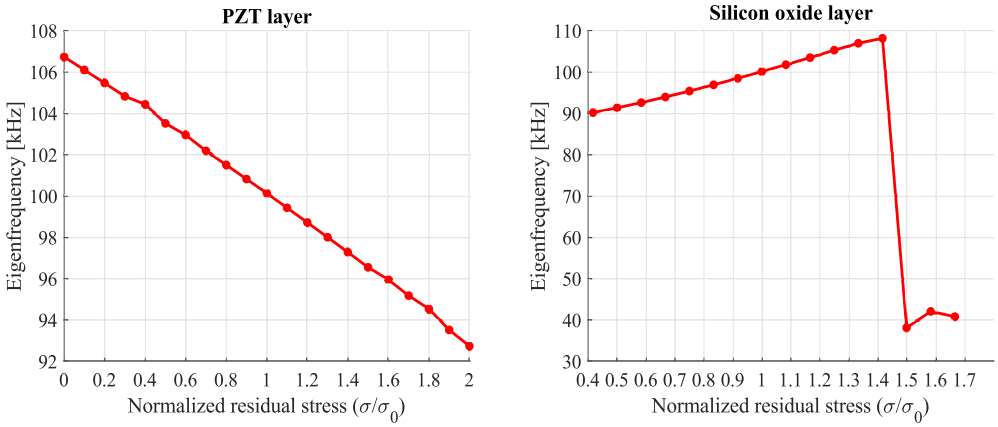

Figure 4.7: *Effect of the variation of the residual stress on the fundamental frequency, for two specific layers: PZT on the left, silicon oxide on the right. The values in abscissa are normalized with respect to the nominal value of residual stress in the specific layer, σ_0.*

ual stress on the fundamental frequency. Fig. 4.7 reports the results for the variation of the residual stress in two specific layers. For the case of PZT, that is characterized by a tensile residual stress, a roughly linear monotonic relationship is obtained: the fundamental frequency is smoothly reduced as the residual stress increases. Conversely, for the oxide layer there is an initial increase, followed by an abrupt reduction. Such a behavior is explained by the fact that the residual stress in the oxide is compressive, so that after a certain threshold the diaphragm buckles as a consequence of excessive compression. This is also confirmed by the examination of the deformed shape, that confirms the reversal of the configuration when the initial stress exceeds 1.4 times the nominal value. As a consequence, the final points on the curve are meaningless. The parametric analysis shows that the residual stresses play a paramount role in the PMUT operation: everything is additionally complicated by the complex interplay between the stresses in the various layers, with different magnitude and sign.

The complete numerical electro-mechanical-acoustic frequency sweep simulation runs in 40 minutes with i7 CPU @3.4 GHz and 16 GB RAM for the COMSOL dissipative axisymmetric model, while the same study requires 45 minutes with intel xeon CPU E5-1650 V4 @ 3.60GHz and 32 GB RAM for the 3D Ansys models.

The experimental validation is performed by means of a wave generator, providing the desired voltage excitation, and by the Polytec MSA-500 Micro System Analyzer to measure the vertical displacement of the center of the diaphragm. The comparison between the normalized vertical displacement spectra is reported in Fig. 4.8.

The Q-factor for the vertical oscillation around the fundamental eigenfrequency of the transducer has been measured by means of a free vibration decay test and its value is $Q_{tot} = 80$. This device Q-factor depends on several sources of energy losses: structural losses Q_{struct}, such as thermoelastic, support, surface layer losses, and fluid losses Q_{fluid}, related to the energy radiation into an infinite medium and to the thermo-viscous losses in the air. According to the COMSOL thermo-acoustics adopted modelling for the fluid domain in the region near to the vibrating diaphragm, it is possible to define, at least numerically, the amount of this last factor as $Q_{fluid} = f/\Delta f$, where Δf is the 3 dB bandwidth at the resonance frequency f, which results equal to $Q_{fluid} = 190$.

The fluid region in which the thermal and viscous losses are greater is the so-called boundary layer, which surrounds the diaphragm on the two sides above and below the diaphragm. The thickness of this layer is related to the penetration thermo-viscous depth and it is shown in Fig. 4.9, where the

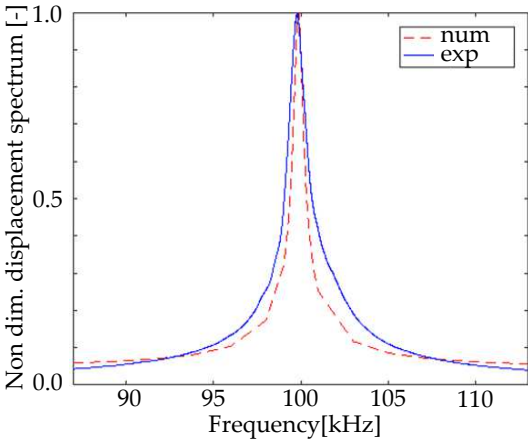

Figure 4.8: *Normalized vertical displacement spectra for the center point of the diaphragm: experimental measurement by Polytec MSA-500 (blue solid line) and numerical estimation by COMSOL Multiphysics v5.2 (red dashed line) and Ansys v17.2.*

map of the total power dissipation density amplitude at 100 kHz is reported.

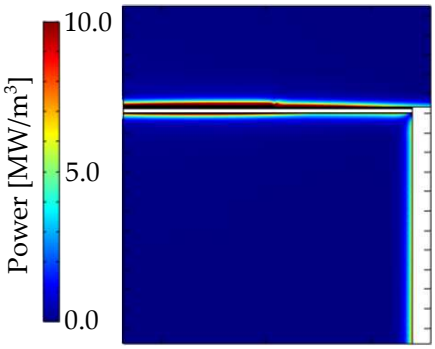

Figure 4.9: *Total thermo-viscous power dissipation density amplitude [W/m^3] at* 100 *kHz in the fluid domain, numerically computed by means of COMSOL Multiphysics v5.2. The region in which the losses are concentrated is the so-called boundary layer; in white the solid domain.*

The structural Q-factor Q_{struct}, which determines the value of the adopted isotropic structural loss factor $\eta_{struct} = 1/Q_{struct}$, is calculated subtracting the inverse of Q_{fluid} to the inverse of the measured Q_{tot}, and extracting the inverse of the result (as common in parallel impedance reduction) [78] thus obtaining $Q_{struct} = 138$.

The Sound Pressure Level (SPL) can be computed in every point of the acoustic domain and outside of it by means of the Helmholtz-Kirchhoff integral technique (the so-called far field calculation technique). The numerically estimated SPL polar plot at 100 kHz in the vertical plane at 3.5 cm

from the vertical axis of symmetry of the diaphragm is shown in Fig. 4.10 for the stand-alone transducer modelled in COMSOL; the Ansys plots are presented in the following Fig. 4.11, respectively for the device surrounded by the fluid and for the system in the operating configuration.

Moreover, the numerically estimated SPL frequency response at 3.5 cm on the vertical axis of symmetry of the diaphragm for the COMSOL model is shown in Fig. 4.12. It is possible to notice that the maximum value occurs in correspondence of the resonance frequency of the diaphragm and it is associated with a non-directional emitted pressure wave, which is typical of a PMUT device not inserted in a protecting packaging structure. For the operating frequency, the value of the computed SPL is compared with the measured one (refer to the red star in Figs. 4.10,4.11,4.12).

The experimental value is obtained setting a microphone, with sensitivity equal to 0.9 mV/Pa, in the same position of the calculated datum. The microphone output voltage and the input voltage provided to the PMUT are shown in Fig. 4.13.

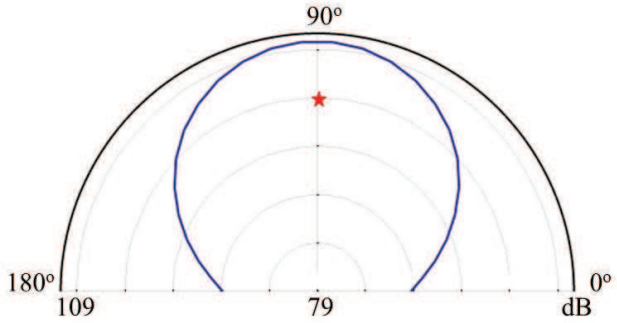

Figure 4.10: *COMSOL Multiphysics v5.2, SPL polar plot in dB at* 100 *kHz, in the vertical plane, at* 3.5 *cm from the center of the diaphragm. The experimental result is highlighted (red star).*

The SPL experimental value detected by the microphone is about 103.0 dB while the numerically predicted one is 109.0 dB for the COMSOL model. The over-estimation of the sound intensity by the model is due to the presence of other source of losses that cannot be taken into account (e.g. cross-talk among diaphragms belonging to the same die, presence of the silicon die), while the 3D Ansys modelling is more accurate giving us the value of 105.0 dB for the case of the single transducer belonging to the silicon die surrounded by the fluid and 104.7 dB for the operating configuration. This is due to the fact that the wave propagation in the horizontal direction is more emphasized than the stand-alone axisymmetric case, due to the presence of the silicon die glued onto the PCB board. According to

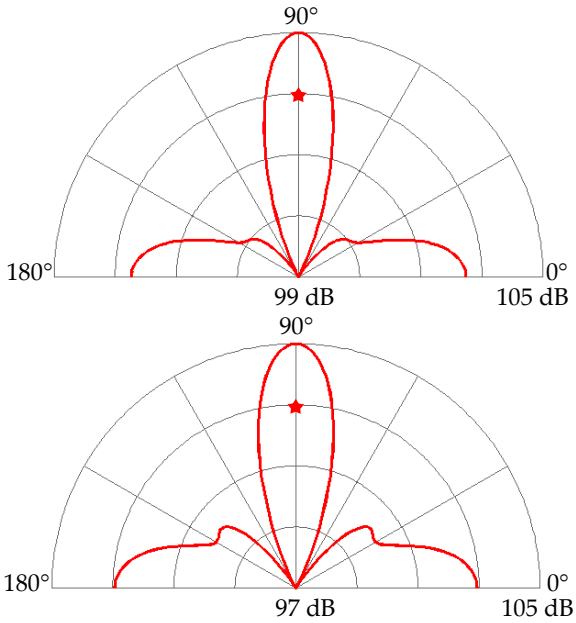

Figure 4.11: *Ansys v17.2, SPL polar plot in dB at* 100 *kHz, in the ZY vertical plane, at* 3.5 *cm from the center of the diaphragm. Single transducer belonging to the silicon die surrounded by the fluid (above), single transducer belonging to the silicon die in the operating configuration (below); the experimental result is highlighted (red star).*

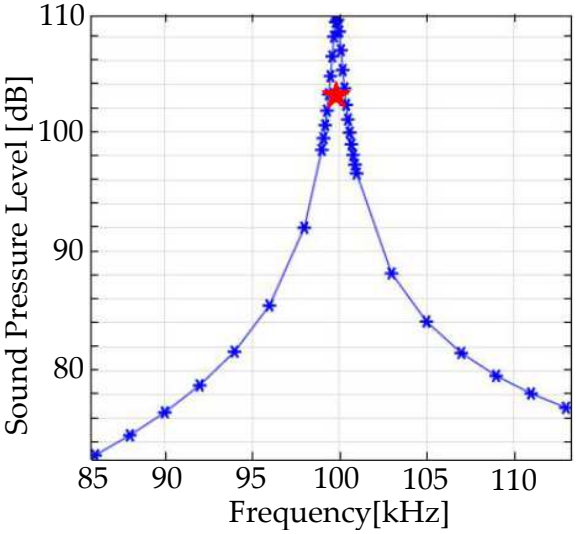

Figure 4.12: *Sound Pressure Level in dB at 3.5 cm on the vertical axisymmetric axis (blue asterisks) numerically computed by means of COMSOL Multiphysics v5.2; the experimental result is highlighted (red star).*

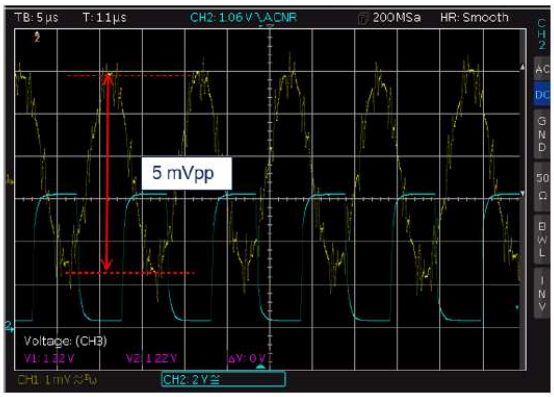

Figure 4.13: *Microphone output voltage in sound intensity measurement (yellow line) at* 3.5 *cm on the vertical axisymmetric axis, in which is highlighted the* 5 *mVpp. Input voltage 3 V amplitude square wave at* 100 *kHz provided to the PMUT.*

that the SPL values are reduced along the vertical direction.

Finally, it is possible to notice this situation also in the SPL polar plots for case of the transducers modelled in Ansys that show completely different shapes, with respect to the stand-alone transducer modelled in COMSOL, along the horizontal direction.

4.5 Numerical results for the 4x4 array of transducers

In this section the numerically computed results by means of Ansys v17.2 for the quarter of array of transducers are presented. The initial static deflection of the layered diaphragms belonging to the silicon die, due to the fabrication process residual stresses, is characterized by the typical predeformed shape and it is shown in Fig. 4.14. The maximum vertical displacement occurs in the center of each diaphragm with value equal to 4.8 μm.

In this case, the complete numerical electro-mechanical-acoustic frequency sweep simulation runs in 14 hours with intel xeon CPU E5-1650 V4 @ 3.60GHz and 32 GB RAM. The study has been carried out enforcing a harmonic voltage perturbation with amplitude of 3 V in parallel to each piezoelectric layer, around the fundamental eigenfrequency of the transducer. In the acoustic domain the Sound Pressure Level 3D map at 100 kHz is shown in Fig. 4.15, while the 3D map computed for the single transducer case in the operating configuration is presented in Fig. 4.16. It is possible to notice that the SPL values at the external boundary, in the case of the 4x4 array in parallel actuation, are much larger than the computed values for the single transducer. In this second case, the wave front approaches the

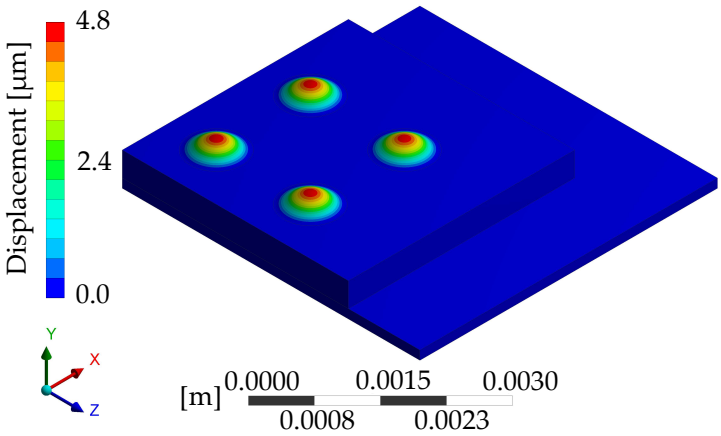

Figure 4.14: *Ansys v17.2, initial static deflection due to fabrication residual stresses in µm.*

hemispherical configuration in the near field, at a distance from the emitting source that is smaller than the array case.

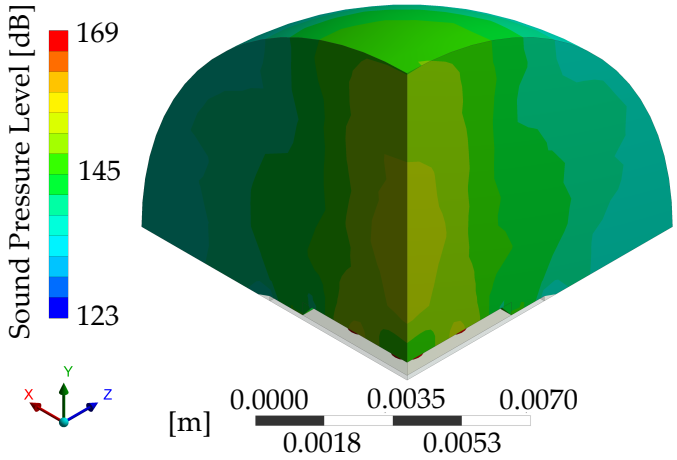

Figure 4.15: *Ansys v17.2, SPL map in dB at* 100 *kHz, for the array of transducers belonging to the silicon die.*

Finally, the SPL plot in the vertical ZY plane is reported in Fig. 4.17 for the 4x4 array of transducer.

The value at 3.5 cm from the silicon die on the vertical direction is 121 dB (refer to Fig. 4.17) in the case of the 4x4 array in parallel actuation, while the corresponding value for the single transducer is 104.7 dB. This is due to the presence of 16 acoustic sources for the case of the array of transducers. According to that the SPL polar shape in the ZY vertical plane is flatter along the vertical direction than the single transducer case.

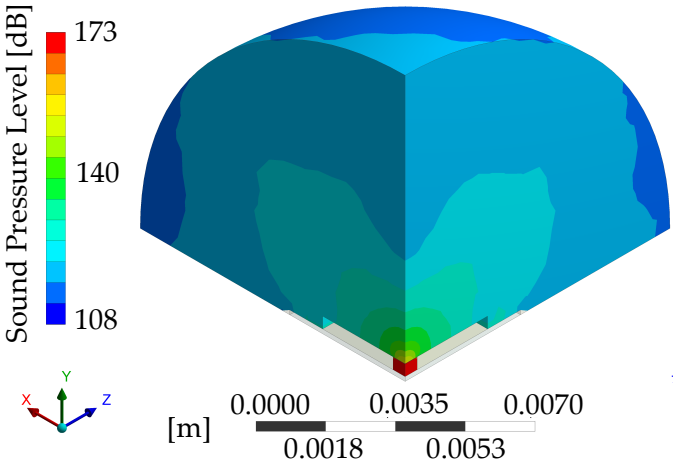

Figure 4.16: *Ansys v17.2, SPL map in dB at* 100 *kHz, for the single transducer belonging to the silicon die in the operating configuration.*

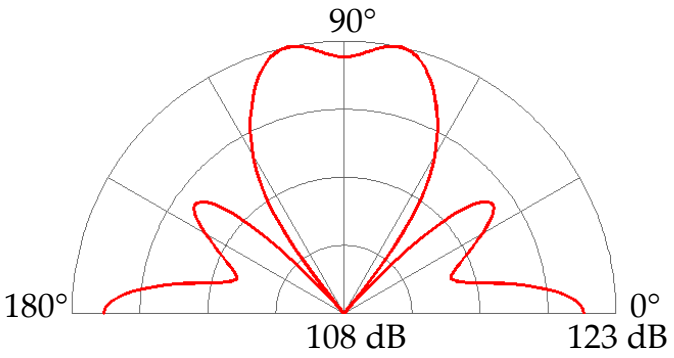

Figure 4.17: *Ansys v17.2, SPL polar plot in dB at* 100 *kHz in the ZY vertical plane, at* 3.5 *cm from the center of the silicon die, for the array of transducers belonging to the silicon die.*

4.6 Closing remarks on array of PMUTs

In this chapter, the results obtained with a comprehensive multiphysics modelling of an air-coupled array of PMUTs have been presented, together with their preliminary experimental validations for the mechanical and acoustic responses. Both axisymmetric and 3D models were analysed, and the results are in good agreement with experiments account taken of the non-linearities introduced by the high diaphragm aspect ratio.

The complete simulation of the device's behavior, considering the multiple couplings among the different physics involved, can guide the designers through the effective control of frequency and quality factor by means of the dissipative modelling of the fluid surrounding the vibrating diaphragm.

The 3D Ansys model for the 4x4 array of transducers is a very efficient numerical tool for the design of the device in the in-parallel actuation phase, giving the numerical estimation of the SPL map in the fluid domain and the computed far field polar plot. Moreover, we can argue that the COMSOL thermo-acoustic model doesn't allow us to simulate the behaviour of the system adopting the 3D geometry, due to the very expensive computational burden. This limitation can be overcome using the vibro-acoustic Ansys modelling with the introduction of a properly tuned non-dimensional damping ratio applied to the solid domain. Some improvements could be introduced with reference to the piezoelectric constitutive law, which is now considered in its standard linarized form. In the future developments, it would be desirable to introduce a non-linear model which account for several important phenomena in the piezoelectric material, i.e. poling, ageing and fatigue.

The adopted modelling, with a double symmetric hypothesis enforced in the vertical plane, is perfectly suited for the simulation of the transmission of waves from an unpackaged device, with vibrating diaphragms according to the fundamental eigenmode; conversely, to simulate the sensing phase, induced by the echo coming back from an obstacle with a generic geometry, a full 3D model of the whole array of transducers is required.

Finally, this kind of systems are usually packaged to protect the PMUT, with the result that the interaction between the fluid and the structure does not involve directly only the vibrating diaphragm but also the package [79]. According to this behaviour, the effects of the protecting cap above the silicon die are considering different package geometries, oriented to the determination of the maximum acoustic efficiency, are described in the next chapter 5.

CHAPTER 5

Effects of package on performances

In this chapter is presented a multiphysics numerical modelling via FEM of an air-coupled packaged array of piezoelectric micromachined ultrasonic transducers.
The proposed numerical model is fully 3D with the following features: the presence of the fabrication induced residual stresses, which determine a geometrically non-linear initial deformed configuration of the diaphragms and a remarkable shift of the fundamental frequency; the multiple coupling between different physics, namely electro-mechanical-coupling for the piezo-electric model, acoustic-structural interaction at the fluid-structure interface and pressure acoustics in the surrounding fluid.
The model takes into account the complete set of PMUTs belonging to the silicon die in a 4x4 array configuration and the protective package, as well. The results have been validated by experimental data, in terms of initial static pre-deflected configuration of the diaphragms and frequency response function of the PMUT.
The numerical procedure has been applied to analyze different package configurations of the device, to study the influence of the holes on the acoustic transmission in terms of SPL and propagation pattern and consequently extract a set of design guidelines.

5.1 Introduction

Several applications of this technology as range-finding [23, 24, 27, 66, 80], gesture recognition [8, 26, 65], finger-printing recognition [81, 82], non-destructive testing and velocity sensing [20, 64], involve the presence of a

flexible protecting cap against the external agents. This chapter builds upon a previous work [79] and deals with a fully 3D modelling of a 4x4 PMUTs array configuration [35, 72] presented in Fig. 5.1 in which the package has been modeled as an elastic vibrating part of the system. This is perfectly

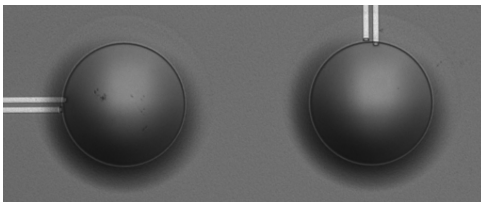

Figure 5.1: *Optical microscope image of two PMUTs.*

suited to simulate the presence of the flexible protecting package of any possible shape [83]. Moreover, the model is characterized by the acoustic-structure interaction enforced at each fluid-structure interface, so the interaction does not involve only the vibrating diaphragms but the package as well [83].

The primary aim of this chapter is to show the influence of the flexible protective package on the acoustic performances of the PMUTs devices [84]. As a matter of fact, different package shapes at different performing frequencies will be studied in terms of SPL maps and polar plots. Moreover, the effects of the package vibration modes on the pressure radiation lobes will be illustrated.

The chapter is organized as follows. The second section describes the multiphysics finite element (FE) modelling of both the electro-mechanical and the acoustic behavior of the transducers [85], account taken of the multiple interactions among the involved physics [67, 86–88]. The model gives a realistic estimation of the pre-deflected configuration, due to the residual stress state and of the fundamental frequency.

In the third section, the corresponding numerical results are reported showing a good agreement with the experimental ones. In section four, the stand-alone performances of the transducer in the transmitting phase, for the packaged and unpackaged device, are shown. Furthermore, the 4x4 array of PMUTs is considered [36, 89] and several package solutions are analyzed to define advantages and drawbacks for each simulated flexible protective cap shapes.

Section five is devoted to conclusions. Closing remarks are reported on the modelling technique and the different pressure scenarios related to the adopted package. Finally, possible future developments are presented.

5.2 Numerical modelling for the packaged device

The finite element model has been developed in ANSYS 17.2. In the numerical model the electro-mechanical-acoustic (EMA) coupling, presented in 3, has been taken into account, for a fully 3D modelling of the device and the surrounding fluid. The thermo-viscous acoustics model for the fluid near to the vibrating diaphragms [73, 90, 91], which has been considered in chapter 4, is here neglected since the primary focus is on the pressure and Sound-Pressure-Level (SPL) far-field responses.

Each circular transducer has radius of 440 μm and an overall thickness equal to 8 μm, such that the diameter/thickness ratio is 110. The structural layer is made of silicon with thickness equal to 4.25 μm. A thin piezoelectric film [92, 93], made of lead zirconate titanate (PZT) [94] is deposited via sol–gel technique, in hat configuration on the structural plate. The PZT layer has thickness of 1.06 μm and is placed in circular hat configuration with radius of 308 μm, coaxial with the diaphragm. The typical layered configuration is shown in Fig. 5.2 in which a cross-section, in the meridian plane of the geometry, is reported.

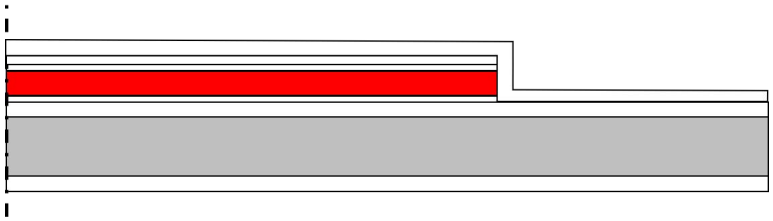

Figure 5.2: *PMUT layered configuration: PZT in red, Si structural layer in grey, other layers in white.*

The piezo-plate belongs to the silicon die [60, 84, 95]. Beneath the PMUT an air-filled closed cylindrical cavity with height of 400 μm and the same radius of the upper diaphragm is present.

The die is glued onto the printed circuit board (PCB) made of FR4 whose bottom face is modelled as a fixed constraint. The symmetry properties of the device is exploited to reduce the computational burden, modelling just a quarter of the device with 2x2 transducers and applying Symmetric Boundary Condition on the two vertical planes. To simulate the radiation into an infinite medium, the absorption condition at the fluid spherical boundary is enforced. On the horizontal surface boundary of the acoustic domain, on the contrary, a hard wall condition is imposed. The model, without the protecting cap, is presented in Figs. 5.3-5.4, in which the geometry

and the mesh details for the different physical domains are shown.

The physics describing the simulated phenomenon are: elastodynamics in the linear elastic layered system, silicon die and PCB, electrostatics in the piezoelectric layer with enforced linear stress-charge law and pressure acoustics in the fluid cavity and in the half-space fluid domain with radius equal to 3λ, where $\lambda = c/f_0 = 3434$ μm is the wavelength, $c = 343$ m/s is the speed of sound in the air at the reference state of T_{ref} = 293.15 K and P_{ref} = 1 atm and f_0 = 100 kHz is the performing frequency of the system, that coincides with the plate fundamental frequency in order to maximize the acoustic efficiency. Hence, the calculated Rayleigh distance is equal to $D_R = S/\lambda = 177.1$ μm, where S is the PMUT area [30, 40, 96, 97].

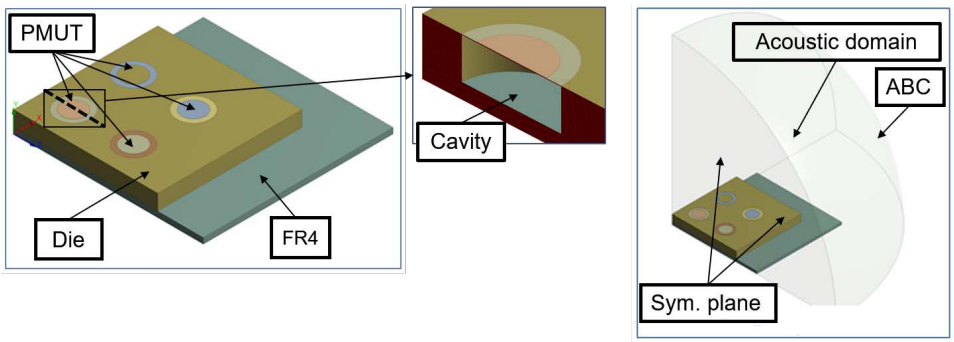

Figure 5.3: *Geometry for the electro-mechanical-acoustic model: a quarter of 4x4 array of PMUTs (left), cross section of the transducers with the cavity (center), solid and acoustic domain (right).*

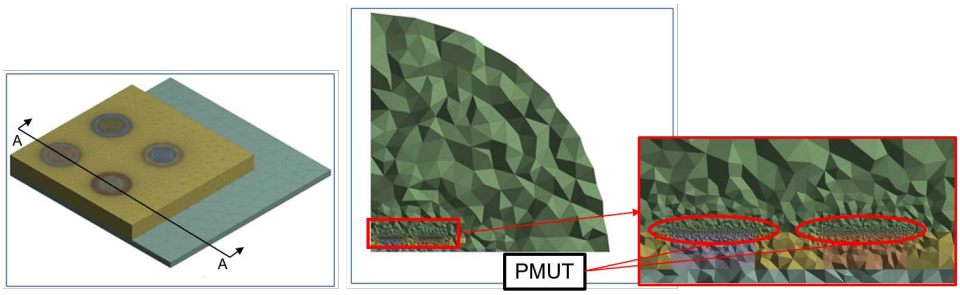

Figure 5.4: *Mesh details: solid domain (left), vertical cross-section along A-A of the solid and acoustic domains (center), structure-acoustic interface (right).*

The FR4 board and the silicon die have been discretized with SOLID226 linear tetrahedrons. The mesh of the plate has been obtained by means of the swept mesh generation technique with solid-like SOLSH190 linear wedge elements for all the layers but the PZT. The piezoelectric domain

has been modelled by means of three SOLID226 piezo linear wedge elements through the thickness. In the silicon structural layer, five wedge elements through the thickness have been used. Conversely, at least one element through the thickness has been inserted in the remaining diaphragm domain, adopting a minimum element size equal to the smallest thickness while the maximum size has been set equal to the thickness of silicon die.

The adopted model to study the pressure propagation in the presence of the protecting cap for the transducer, is shown in Fig. 5.5. Herein, the package is constituted of brass which has thickness of 150 μm and is discretized as a linear elastic material through SOLSH190 linear wedge elements, with one element through the thickness. Hence, the fluid-structure interaction is enforced not only at the vibrating diaphragms structural-acoustic interfaces but at the package wet surface as well.

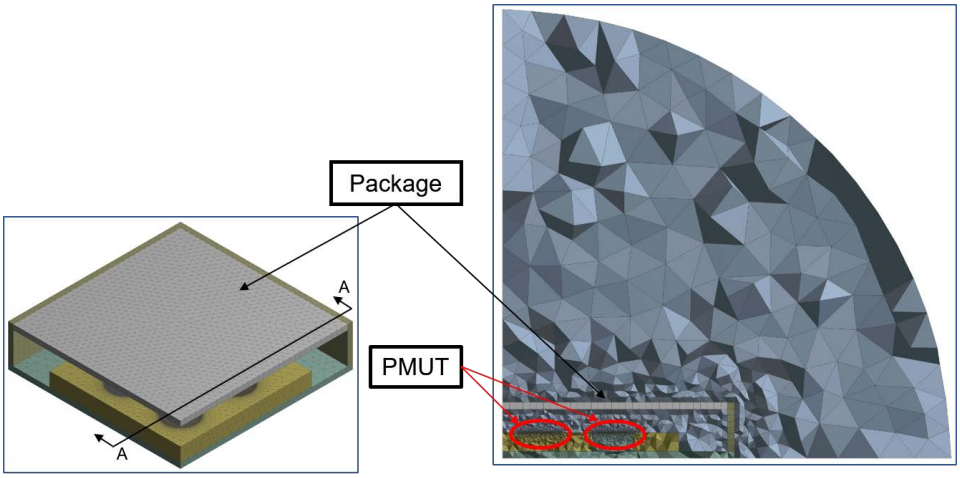

Figure 5.5: *Mesh details: packaged transducer with no hole (left), vertical cross-section along A-A of the solid and acoustic domains (right).*

The fabrication induced residual stresses are taken into account through an amount of pre-stress isotropically acting in the plane of each layer, so that the cross section is characterized by tensile and compressive initial stresses. They play an important role in the initial deformation and on the geometric stiffness of the structure in the large displacement formulation.

The quality factor of the system, related to the fundamental mode, has been measured by means of a free vibration decay test and corresponds to $Q_{tot} = 80$. It depends on several sources of energy losses, namely: structural losses Q_{struct}, which model the effects of the thermoelastic, support, surface layer losses, and fluid losses Q_{fluid}, related to the energy radiation into an infinite medium. In the EMA frequency analysis of the device, con-

sidering the adopted absorbing condition at the fluid boundary, the overall structural damping has been introduced by means of an enforced damping ratio, equal to $\zeta = 1/2Q_{struct}$ in the dynamic equations of motion, where a numerical $Q_{struct} = 100$ has been imposed to obtain the acceptable match between the numerical and the known experimental Q_{tot}. Accordingly, the numerical $Q_{fluid} = 258$ has been computed subtracting the inverse of Q_{struct} to the inverse of the Q_{tot} and extracting the inverse of the result (as common in parallel impedance reduction) [78, 98].

In the pressure acoustic hemisphere, the Helmholtz equation has been solved, adopting a discretization constituted of FLUID30 linear tetrahedral elements with maximum element size equal to $\lambda/6$. The Fluid-Structure Interaction (FSI) is enforced by means of the continuity of the normal stresses and of the normal accelerations at the wet boundaries. Moreover, Absorbing Boundary Condition (ABC) on the spherical pressure acoustic boundary has been modelled by means of FLUID130 linear triangular elements. Finally, outside the pressure acoustic domain, the far-field response has been computed through the Kirchhoff-Helmholtz integral technique [40, 99].

The electro-structural-acoustic response is computed at two different performing frequencies by means of a sequence of simulations: i) a geometrically non-linear static analysis has been performed to compute the pre-deflected configuration induced by the fabrication residual stresses, ii) an electro-mechanical static analysis has been performed to compute the starting performing configuration, considering two bias voltage levels of 3 V and 10 V, iii) an electro-mechanical eigenfrequency analysis, around the previously computed performing starting deformed configuration, has been carried out to evaluate the fundamental frequency of the device at the two bias levels, iv) an electro-mechanical-acoustic frequency analysis at the performing diaphragms fundamental frequency has been performed, around the stressed deformed starting configuration, to compare the solutions for a harmonic voltage perturbation with amplitude of 3 V account taken of the constant bias voltage. The goal has been to investigate the performances of the system in the transmitting phase at two different performing PMUTs fundamental frequencies, under the influence of the starting configuration due the combination of the pre-stresses and the bias voltage and of the adopted package geometry.

5.3 Numerical results and experimental validation

In this section, the comparison between the experimental and numerical results of the first study, described in the previous section, are shown (Fig.

5.6). To compute the starting configuration of the transducers, which is characterized by a high aspect ratio (diameter/thickness) of 110, a large displacements static analysis has been carried out under the influence of the residual stress state. The numerically computed displacement of the diaphragm is characterized by a maximum value of 4.85 μm, which occurs at the center point, in the vertical direction. The corresponding experimental measurement has been executed via the white-light interferometry by means of the Polytec MSA-500 microsystem analyzer. The related displacement contour plot map together with the plate profile along a diameter show a maximum value at the center equal to 5.2 μm.

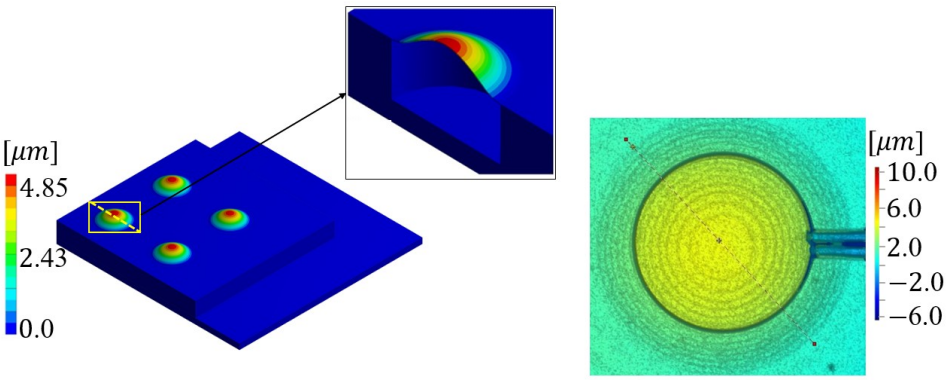

Figure 5.6: *Initial static configuration due to fabrication residual stresses: numerically computed by means of ANSYS 17.2 [μm] (left); experimental measurement by means of Polytec MSA-500, top view (right).*

In addition to the initial deformed shape, the residual stresses play the most important role in the geometric stiffness of the diaphragm. Indeed, the initial state of stress significantly changes the fundamental frequency of the PMUT. It is worth noting that the diaphragm without the residual stresses presents a theoretical fundamental eigenfrequency of 111.55 kHz; taking into account the contribution to the geometric stiffness due to the pre-stress state, it decreases to 99.9 kHz and is correctly captured by the numerical model that predicts 100.0 kHz. To identify the shift, the electro-mechanical-acoustic frequency sweep analysis has been performed with a harmonic voltage excitation with amplitude of 3 V and zero DC voltage bias, around the fundamental frequency. The result of the study in terms of vertical displacement amplitude of the center of the plate, is reported in Fig. 5.7. The corresponding measurements are shown in Fig. 5.8 in which the first three axisymmetric modes are presented. The experimental results, obtained through the Polytec MSA-500 laser-doppler vibrometer, are related

to a frequency sweep test with the excitation of 1 V amplitude and zero DC voltage bias [100, 101], provided to the PZT electrodes, ranging from 10 kHz to 1 MHz.

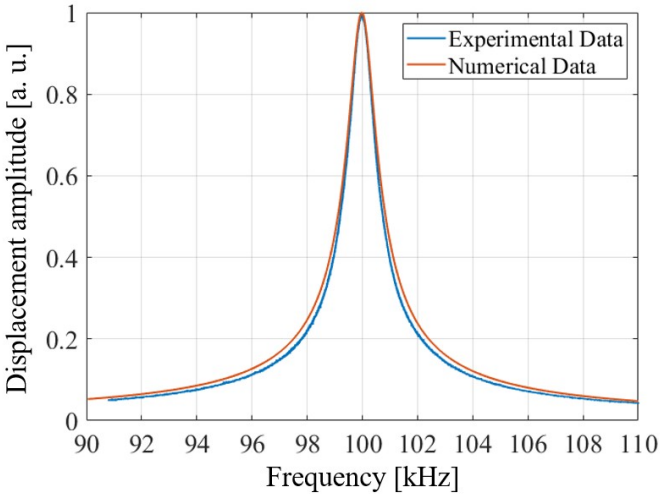

Figure 5.7: *Comparison between experimental and numerically computed transversal normalized displacement frequency amplitude spectrum at the center of the PMUT by means of ANSYS 17.2.*

5.4 Analyses in presence of package

In this section, different package configurations are presented with the effects on the transducer performance in terms of acoustic intensity and wave propagation pattern.

5.4.1 Stand-alone device vs. packaged device

The effect of the protecting cap on the acoustic performances of the transducer is studied through the numerical comparison between the stand-alone device and the packaged.

The adopted acoustic finite element modelling of the surrounding fluid allows one to evaluate the acoustic efficiency [102] of the PMUT in the fluid domain in terms of Sound Pressure Level (SPL) at the distance of 3.5 cm from the center of the die, along the acoustic vertical axis of the device. Furthermore, the model has been used to get the pressure propagation map and the SPL radiation beam pattern in the polar plot, related to the analyzed package geometry and dynamic behavior. Hence, it represents a powerful

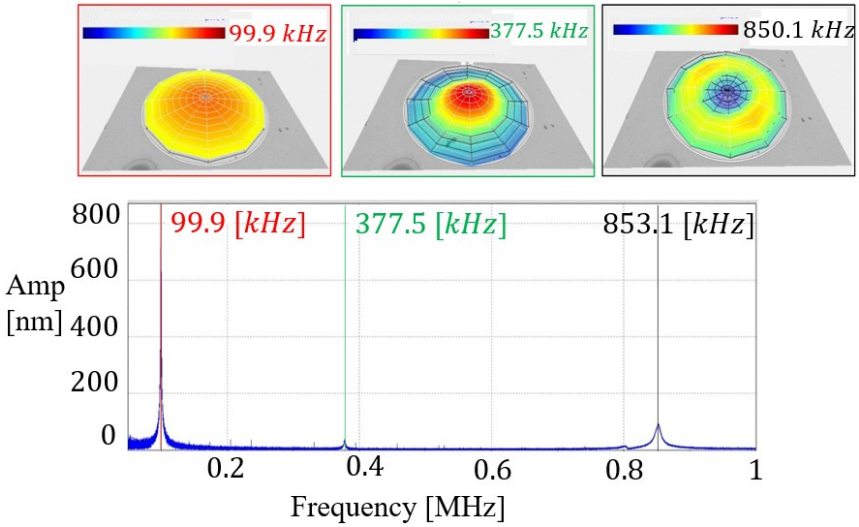

Figure 5.8: *Transversal displacement frequency amplitude spectrum at the center of the PMUT by means of the Polytec MSA-500: 1st mode shape (top, left), 2nd axisymmetric mode shape (top, center), 3rd axisymmetric mode shape (top, right).*

tool to study directivity and beam-forming problems involving the whole vibrating system.

To this aim, the pressure field has been computed in every point of the computational fluid domain and outside of it by means of the Kirchhoff-Helmholtz integral technique (the so called far-field calculation technique), based on the pressure values and gradients evaluated on an integration surface which encompass the entire device.

The parameters which define the protecting cap are illustrated in Fig. 5.9. The distance H_{cap}, from the top surface of the die to the bottom surface of the cap, is equal to 500 μm. In the presence of the holed package configuration the parameter R_{hole} refers to the radius of the vent and it is expressed in terms of the PMUT radius R_{PMUT}.

The two limit situations, illustrated in Fig. 5.10, have been simulated, in which the transducer is not protected by any system and in the presence of the package with no vent ($R_{hole} = 0$ μm), characterizing the maximum protection against any external agent.

To investigate the dynamic behavior of the device in the two cases, a non-linear electromechanical-eigenfrequency analysis has been performed, taking into account the presence of the residual stress state on the geometric stiffness. The results of the study are shown in the following two figures in terms of displacement eigenmode of the stand-alone and the packaged

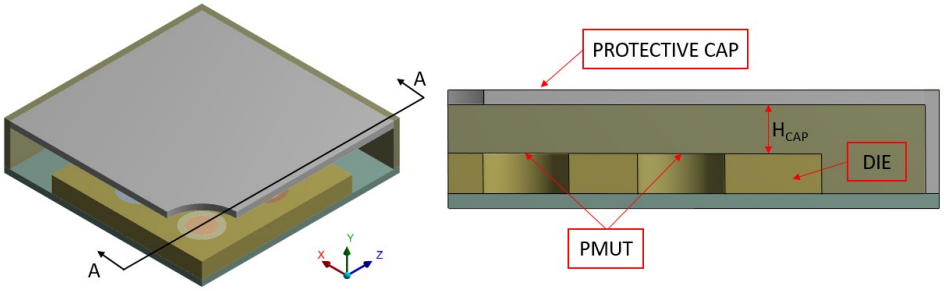

Figure 5.9: *Package configuration: geometry quarter (left), cross-section A-A and parameters (right).*

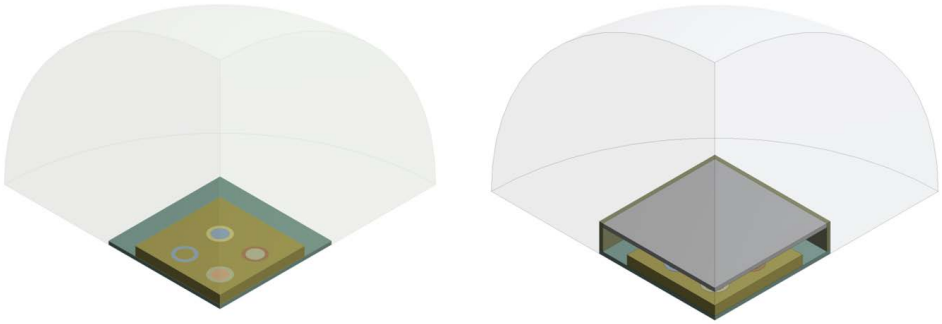

Figure 5.10: *Analyzed limit situations: stand-alone device (left), packaged device (right).*

device; the former (Fig. 5.11) corresponds to the performing fundamental frequency of the designed PMUTs taking into account the residual stresses and a constant bias voltage of 3 V and 10 V, while the latter (Fig. 5.12) shows the related package displacement eigenmodes, around the fundamental frequencies of the transducer for the two considered voltage bias.

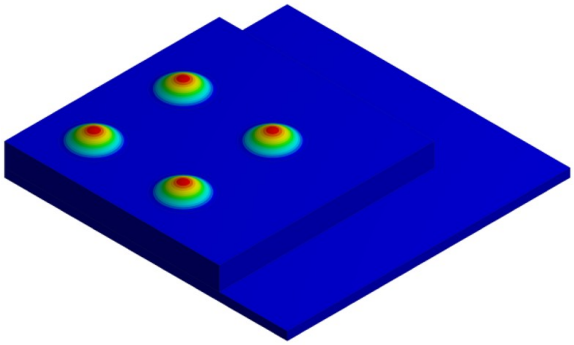

Figure 5.11: *Fundamental electro-mechanical displacement mode shape of the stand-alone device 93.0 kHz (3V bias), 85.5 kHz (10 V bias).*

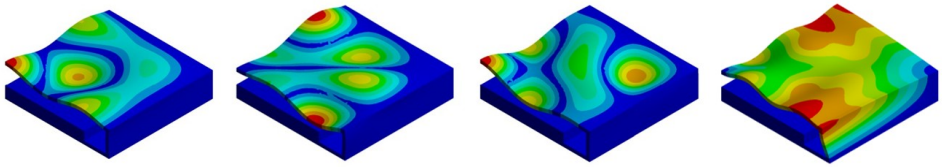

Figure 5.12: *Four package displacement eigenmodes around the fundamental frequency: 6th mode shape at 81.46 kHz (left), 7th mode shape at 104.18 kHz (center-left), 8th mode shape at 104.45 kHz (center-right) 16th mode shape at 158.110 kHz (right).*

Due to the presence of the protective package, the acoustic waves propagate inside the acoustic domain through the cap vibration. Therefore, it is useful to investigate the package eigefrequencies and the associated mode shapes to detect which ones are involved in the acoustic propagation, characterizing the device acoustic performances in terms of acoustic intensity and directivity. In Fig. 5.12 the attention is focused on the four package displacement eigenmodes, around the performing fundamental frequencies of the transducers 85.5 kHz (10 V bias) and 93.0 kHz (3 V bias) and together with the first package eigenmode with deformed walls. The shown package eigenfrequencies are not significantly affected by the applied static bais voltage. To investigate the SPL maps, the response has been obtained in the frequency domain, considering all the PMUTs actuated in parallel

with a harmonic voltage excitation of 3 V amplitude and two different bias voltage levels, respectively of 10 V and 3 V, at the corresponding fundamental frequencies of the plates equal to 85.5 kHz (applying 10 V bias) and 93.0 kHz (applying 3 V bias).

The comparison between unpackaged and package devices, in terms of numerically computed SPL contour plot, are presented in Figs. 5.13-5.14 for the cases of constant bias voltage of 10 V and 3 V.

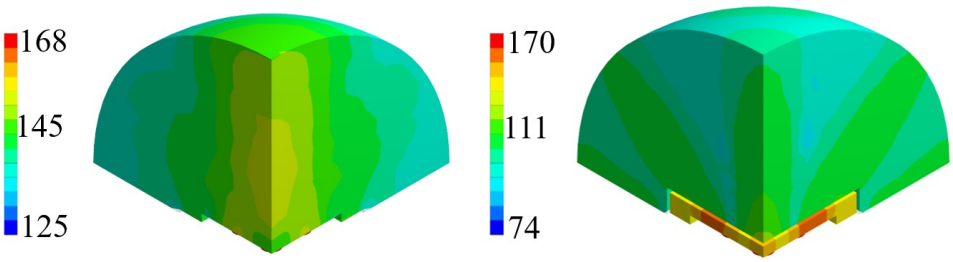

Figure 5.13: *SPL contour plot [dB] at the performing fundamental frequency of 85.5 kHz (10V bias): unpackaged device (left), packaged device (right).*

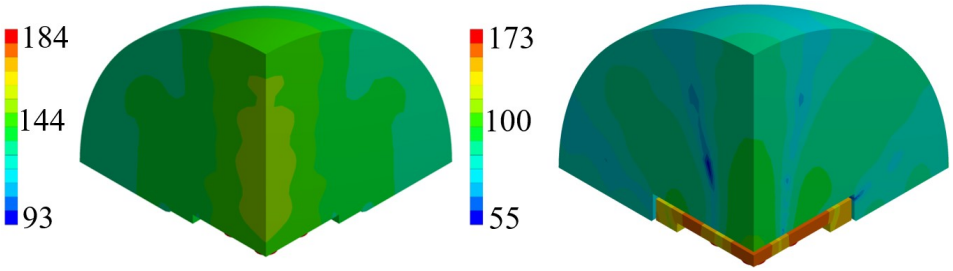

Figure 5.14: *SPL contour plot [dB] at the performing fundamental frequency of 93.0 kHz (3V bias): unpackaged device (left), packaged device (right).*

It is worth noting that, for both the analyzed scenarios, the maximum value in the SPL occurs in each cavity below the transducers. Moreover, in presence of packaging, there are high values of SPL in the acoustic domain in between the silicon die and the protective cap, which cause several reflections of the acoustic waves inside the device and the package vibration. Furthermore, the presence of the cap without holes reduces the maximum value of SPL along the vertical acoustic axis of the system passing through the center of the device, as it is reported, for both the actuation frequencies, in Figs. 5.15-5.16 as well. In these figures the SPL polar plots are sketched at a distance of 3.5 cm from the center of the die and in the vertical plane y-z passing through the center of the system at the analysis frequencies.

Considering the simulated package configuration, a vertical lobe and two side lobes of propagation, at 47 degrees from the vertical axis of 90 degrees in the y-z plane, are visible together with the horizontal one at 0-180 degrees, due to the package walls vibration.

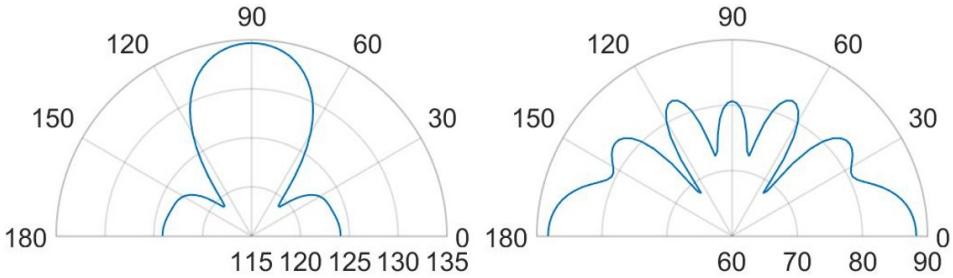

Figure 5.15: *SPL polar plot [dB] at the performing fundamental frequency of 85.5 kHz (10V bias), at 3.5 cm in the y(90 deg)-z(0 deg) plane: unpackaged device (left), packaged device (right).*

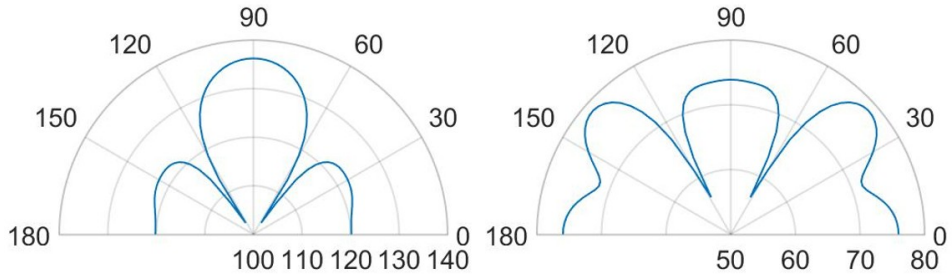

Figure 5.16: *SPL polar plot [dB] at the performing fundamental frequency of 93.0 kHz (3V bias), at 3.5 cm in the y(90 deg)-z(0 deg) plane: unpackaged device (left), packaged device (right).*

Concerning the unpackaged system, it exhibits the maximum value of SPL along the vertical direction of 90 degrees with the same intensity for the two analyzed fundamental frequencies [103]. This is basically in accordance with the lack of the protective cap, which reflects the acoustic waves inside the device and determines the wave propagation in the surrounding fluid according with its own excited vibration modes. In the cap-free configuration one can notice that the vertical lobe shape has no significant variation at the two frequencies of 85.5 kHz and 93.0 kHz. There are slightly different patterns and values at 30 degrees and the horizontal directions, due to the different initial deformed configurations, under the bias static voltage, around which the vibration starts. the applied bias voltage contracts the initial deformation due to the residual stresses, hence the most deformed configuration is associated with the lowest bias voltage of 3 V and fundamental frequency of 93.0 kHz. Consequently, at 93.0 kHz, the system

tends to spread the acoustic energy on spherical wavefronts along the horizontal direction and the transmission becomes more intense approaching the vertical direction, due to the waves composition coming from all the involved vibrating PMUTs.

Considering the packaged system, the acoustic intensity in the surrounding fluid is lower with respect to the unpackaged device, due to the obstructive effect induced by the protective cap without any vent. Further considerations about the wave propagation pattern are based on the SPL polar plots. As a matter of facts, Fig. 5.16 predicts a flat main vertical lobe between 70 and 110 degrees of 74 dB, at the frequency of 93.0 kHz. While, Fig. 5.15 shows three separate narrow lobes of propagations around the same interval of polar angle with local maxima of about 80 dB for the vertical one and 83 dB for the specular side ones.

Horizontal propagation of the acoustic waves characterizes both the analyzed cases, with higher values of SPL for the unpackaged system, due to the fact that there are no obstacle to the transmission, as the package walls are. The packaged system, indeed, is characterized by the SPL values of 88 dB along the direction of 0-180 degrees at the frequency of 85.5 kHz, while at 93.0 kHz, the SPL value along the horizontal direction is equal to 76 dB and the maximum intensity of 78 dB are reached along the directions of 43 and 137 degrees and related to the involved protecting cap eigenmodes.

5.4.2 Simulations for different package geometries

Going further, several simulations have been performed considering devices with different kind of protective caps. To investigate the propagation patterns in the far field. Six new configurations of the protective cap are sketched in Figures 5.17,5.18: (a) central hole of radius equal to $R_{hole} = R_{PMUT}/3$; (b) central hole of radius equal to $R_{hole} = 2R_{PMUT}$; (c) holes placed at the center of each transducer, with radius equal to $R_{hole} = R_{PMUT}/2$ and total holed surface equal to $A_{hole} = \pi \cdot (2R_{PMUT})^2$, as the case (b); (d) hole at the center of the package, suggested by the SPL shape on the outer cap surface in the case of the previously analyzed no-hole situation (see Fig. 5.10, right picture) and total holed surface $A_{hole} = 4\pi \cdot (2R_{PMUT})^2$, four times larger than case (b); (e) random holes of radius equal to $R_{hole} = R_{PMUT}/4$ and total holed surface equal to $A_{hole} = \pi \cdot (2R_{PMUT})^2$, as the case (b) and (c); (f) central hole of radius equal to $R_{hole} = \sqrt{A_{hole}/\pi}$ where A_{hole} is the holed area in the case (d) that implies $R_{hole} = 4R_{PMUT}$, two times greater than case (b). The SPL maps and the SPL polar plots, at the reference distance of 3.5 cm from the center of the die, in the vertical plane

y-z passing through the center of the system, have been computed at the performing fundamental frequencies of the transducers and they are showed in the following figures for the case (a)-(e). Case (f) will be described in the next section in which several comments on the acoustic transmission efficiency, considering the comparison plots between two analyzed situations, will be drawn.

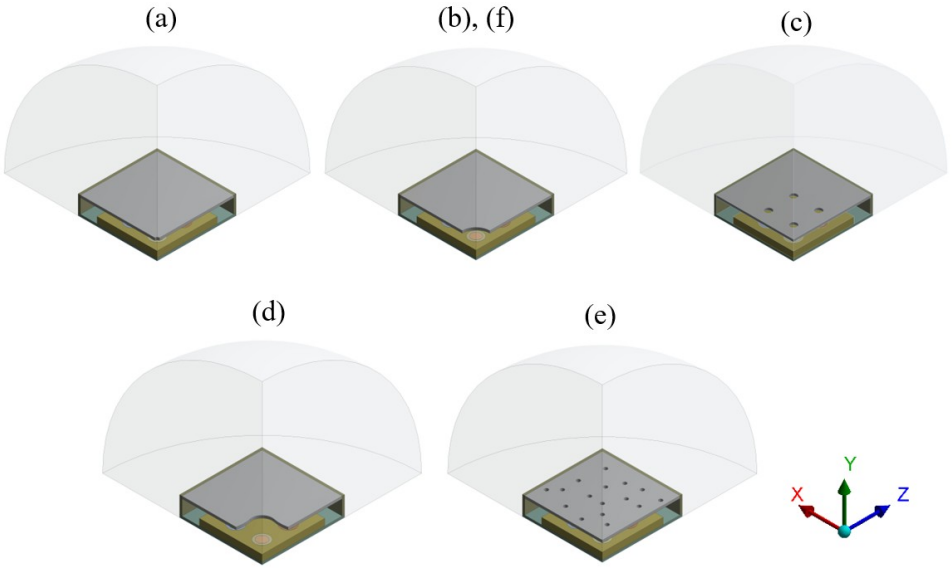

Figure 5.17: *Different cap geometries as described in the main text.*

To identify the modes of vibration involved in pressure waves propagation, an eigenfrequency analysis has been performed for the five cap configurations, taken into account the residual stress state and the applied static bias voltages; the results in terms of eigenmode shapes, around the transducers performing fundamental frequencies of 85.5 kHz (10 V bias) and 93.0 (3 V bias), together with the package eigenmode with deformed walls, are shown in Figs. 5.18-5.22.

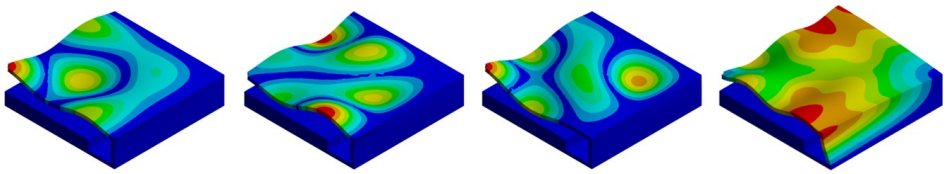

Figure 5.18: *Four package modes for case (a): 6th mode shape at 81.32 kHz (left), 7th mode shape at 104.13 kHz (center-left), 8th mode shape at 104.29 kHz (center-right), 16th mode shape at 157.53 kHz (right).*

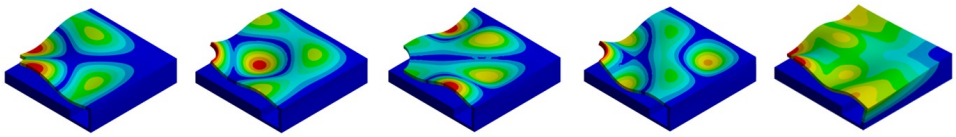

Figure 5.19: *Five package modes for case (b): 5th mode shape at 78.86 (left), 6th mode shape at 85.02 kHz (center-left), 7th mode shape at 103.45 kHz (center), 8th mode shape at 110.32 kHz (center-right), 13th mode shape at 136.14 kHz (right)).*

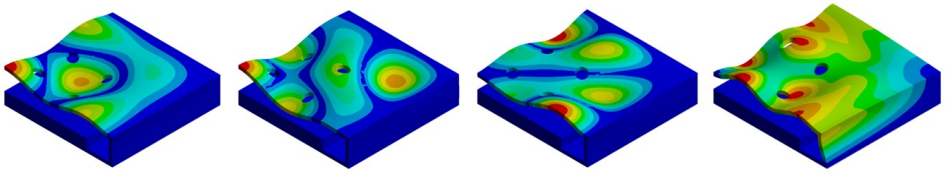

Figure 5.20: *Four package modes for case (c): 6th mode shape at 80.18 kHz (left), 7th mode shape at 102.66 kHz (center-left), 7th mode shape at 102.66 kHz (center-right), 16th mode shape at 151.01 kHz (right).*

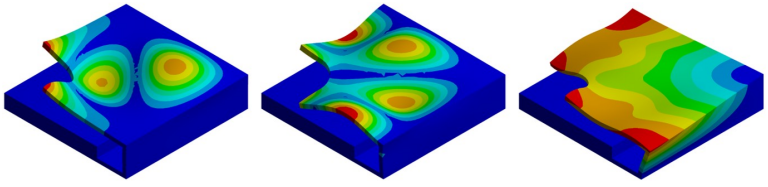

Figure 5.21: *Three package modes for case (d): 6th mode shape at 91.53 kHz (left), 7th mode shape at 101.82 kHz (center), 8th mode shape at 108.23 kHz (right).*

Fig. 5.18 shows that in terms of eigenfrequencies the differences are minimal between the package solution (a) and no-hole limit situation. One can notice that, (c) and (e) are characterized by lower frequencies due to the stiffness reduction of the package induced by the presence of the holes. While, case (d) in Fig. 5.21 shows the higher frequency associated with the sixth mode, because of the modal mass reduction due to the particular shape of the hole. It is worth noting that, during the functioning, the transducer performance involves the vibration of the package walls as well. Hence, the first eigenmode associated with the package walls deformation is reported. It is characterized by the higher eigenfrequency and determines high SPL values in the horizontal direction. The response, also in these cases, has been obtained in the frequency domain. All the PMUTs have been actuated in parallel with a harmonic voltage excitation of 3 V amplitude and two different bias voltage levels, respectively of 10 V and 3 V, at the cor-

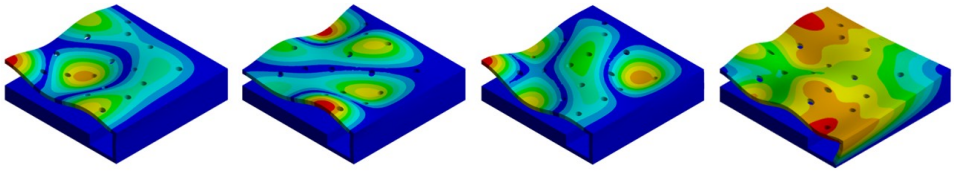

Figure 5.22: *Four package modes for case (e): 6th mode shape at 80.13 kHz (left), 7th mode shape at 102.43 kHz (center-left), 8th mode shape at 102.81 kHz (center-right), 16th mode shape at 154.38 kHz (right).*

responding fundamental frequencies of the plates equal to 85.5 kHz (10 V bias) and 93.0 kHz (3 V bias). The SPL maps are shown in the following Figs. 5.23-5.24 for the cases (a), (b), (c) and Figs. 5.27-5.28 for the cases (d), (e). While, the corresponding polar plots are presented in Figs 5.25-5.26 for the cases (a), (b), (c) and Figs 5.29-5.29 for the cases (d) and (e).

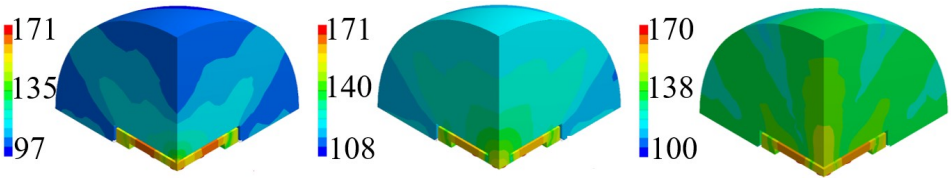

Figure 5.23: *SPL contour plot [dB] at the performing fundamental frequency of 85.5 kHz (10 V bias): (a) (left), (b) (center), (c) (right).*

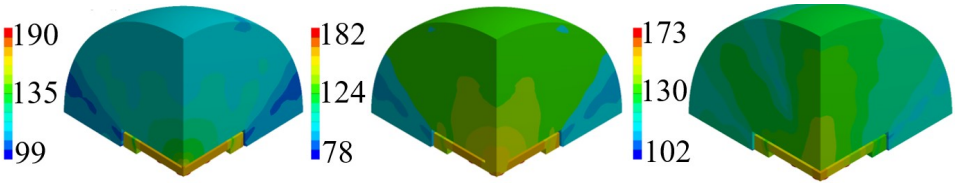

Figure 5.24: *SPL contour plot [dB] at the performing fundamental frequency of 93.0 kHz (3V bias): (a) (left), (b) (center), (c) (right).*

Considering the package configurations (a), (b) and (c) at the two analyzed frequencies, the maximum value in the SPL occurs inside each cavity below the transducers. Furthermore, there are high SPL values in the acoustic domain, between the top surface of the die and the protective cap for the case (a) and (b), as the previous no-hole package configuration showed with great reflections of acoustic waves. Regarding the case (c), the presence of a vent directly above each diaphragm let the waves propagate with lower obstructive effect. Consequently, higher acoustic energy is spread in the

surrounding fluid.

The case (a), with a central hole of $R_{hole} = R_{PMUT}/3$ is characterized by greater reflections of acoustic waves than the case (b) with $R_{hole} = 2R_{PMUT}$ and (c). This is due to the fact that the protective cap of configuration (a) is stiffer than the other ones. Hence, the highest SPL values inside the PMUTs cavity is about 166 dB and correspond to the situation (a), while in the cases (b) and (c) the maximum SPL values are respectively 164 dB and 160 dB.

Further remarks about the propagation of the acoustic waves and the SPL values are possible, considering the SPL polar plots, shown in Fig. 5.25-5.26, at a distance of 3.5 cm from the center of the die and in the vertical plane y-z, passing through the center of the system at the analysis frequencies. In the case (a) at the frequency of 85.5 kHz, Figs. 5.25 reports two narrow lobes around 45 degrees from the vertical acoustic axis of the device together with the vertical and the horizontal ones, related to the involved protective cap eigenmodes of vibration. Hence a strongly directivity is reported with maximum 99.5 dB along the vertical direction, 96 dB at 45-135 degrees and 97 dB at 0-180 degrees. In the case (b) at 85.5 kHz, one can notice that higher SPL values and a wider polar plot (Fig. 5.25), due to the fact that there is a larger hole, but the same preferential ways of propagation are still present. Therefore, the maximum is in correspondence of 90 degrees and equal to 112.5 dB, at 45.135 degrees the SPL is 110 dB and at 0-180 degrees it is 108 dB. Regarding the configuration (c) at 85.5 kHz, characterized by the presence of a vent placed above the center of each transducer, the acoustic waves propagate with less reflections inside the fluid domain between the die and the protective cap, resulting in higher SPL values. In this situation the main vertical lobe, with maximum of 121 dB, is in between the unpackaged and the no-holed package configuration ones (see Fig. 5.16). Moreover, two propagation lobes at around 45 degrees from the vertical axis appear, as well, with local maxima of 115 dB. It is worth noting that a strongly horizontal propagation is reported with SPL value of around 117 dB. As matter of facts, part of the energy excites eigenmodes associated with the vibration of the package walls. The holes placed directly above each transducer reduce the package stiffness and produces a lower obstructive effect for the acoustic propagation.

Actuating the diaphragms at 93.0 kHz, produce wider lobes of propagation with the same shape. In the cases (a) the narrow lobes disappear leaving place to a larger lobe around 90 degrees, with maximum value equal to 104 dB, that reaches the two side lobes at 45-135 degrees with local maxima of 103 dB. Furthermore, the horizontal propagation is still present with

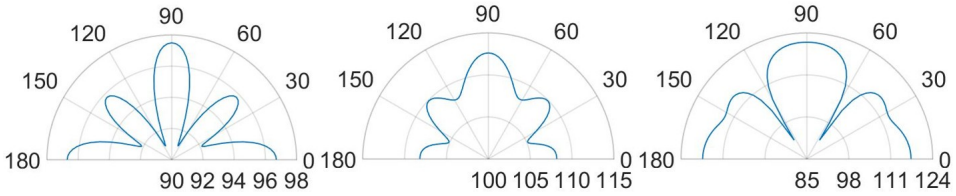

Figure 5.25: *SPL polar plot [dB] at the performing fundamental frequency of 85.5 kHz (10V bias), at 3.5 cm in the y(90 deg)-z(0 deg) plane: (a) (left), (b) (center), (c) (right).*

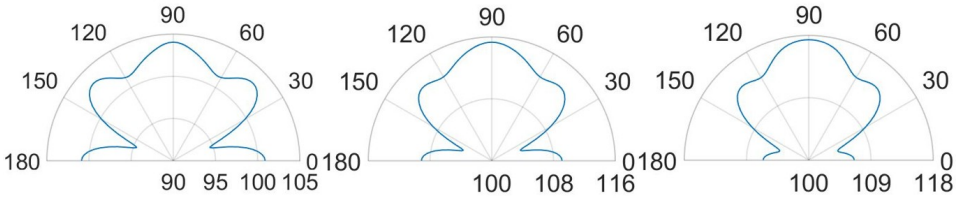

Figure 5.26: *SPL polar plot [dB] at the performing fundamental frequency of 93.0 kHz (3V bias), at 3.5 cm in the y(90 deg)-z(0 deg) plane: (a) (left), (b) (center), (c) (right).*

SPL local maxima equal to 101 dB. The case (b) represents the enlarged situation (a) with maximum SPL of 115 dB along the vertical direction, side lobes at 45-135 degrees with local maxima of 113 dB and horizontal propagation with local maxima of around 109 dB. The case (c) is characterized by a reduced horizontal propagation with local maxima of 106.5 dB. While, the main vertical lobe is present with maximum value equal to 117.5 dB and reaches the two side lobes at 45-135 degrees with local maxima of 114.5 dB.

The numerically computed SPL contour plots for the cases (d) and (e), are presented in Figs. 5.27-5.28, respectively at the analysis frequencies of 85.5 kHz and 93.0 kHz.

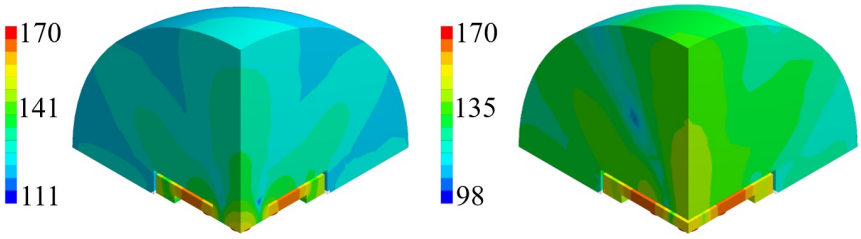

Figure 5.27: *SPL contour plot [dB] at the performing fundamental frequency of 85.5 kHz (10V bias): (d) (left), (e) (right).*

In the case (d) the hole suggested by the SPL shape on the cap surface, let the acoustic waves follow their natural propagation, generating lower

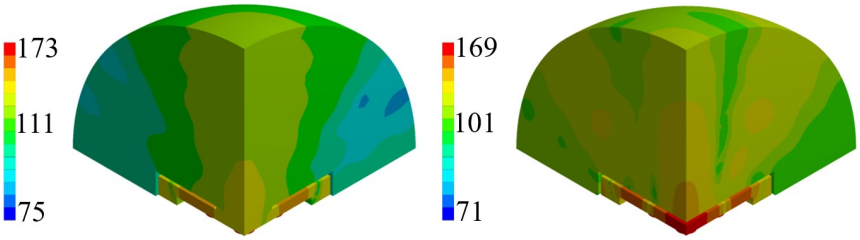

Figure 5.28: *SPL contour plot [dB] at the performing fundamental frequency of 93.0 kHz (3V bias): (d) (left), (e) (right).*

reflections inside the fluid domain between the protective cap and the die. The maximum SPL value, reached into the transducers cavities is about 160 dB and 5 dB lower than that one in correspondence of the limit situation with no hole. Further, greater acoustic energy is spread in the surrounding fluid domain because of a lower obstructive effect. It is worth noting that, the wave propagation at 90 degrees and at 45-135 degrees, in the vertical plane, is still present in the case (d), due to the vibration of the cap. While, but for the packaging solution (e) in the near field the symmetry is completely lost due to the randomness configuration of the holes.

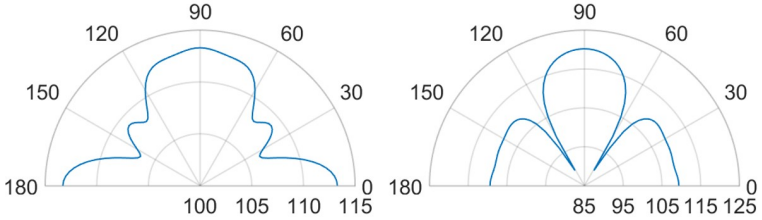

Figure 5.29: *SPL polar plot [dB] at the performing fundamental frequency of 85.5 kHz (10V bias), at 3.5 cm in the y(90 deg)-z(0 deg) plane: (d) (left), (e) (right).*

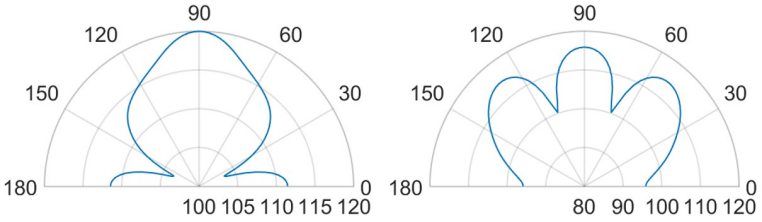

Figure 5.30: *SPL polar plot [dB] at the performing fundamental frequency of 93.0 kHz (3V bias), at 3.5 cm in the y(90 deg)-z(0 deg) plane: (d) (left), (e) (right).*

Further considerations about the propagation of the acoustic waves and

the SPL values are related to the SPL polar plots, shown in Fig. 5.29-5.30, at a distance of 3.5 cm from the center of the die and in the vertical plane y-z, passing through the center of the system at the analysis frequencies. At the frequency of 85.5 kHz, Figs. 5.29 reports, in the case (d), one wide lobe in the range of 70-110 degrees with local maximum of 113 dB along the vertical direction related to the involved protective cap eigenmodes. Furthermore, the horizontal propagation at 0-180 degrees is due to the package lateral walls vibration with maxima of 113.5 dB. Two narrow specular side lobes around the directions of 40-150 degrees are present with local maxima of 108.5 dB. The case (e), at 85.5 kHz, tends to the case (c), in which there is a coaxial vent directly above each diaphragm, with a wide single vertical lobe with maximum value of 120 dB along the vertical direction and two wide side lobes with local maxima equal to 109 dB along the horizontal direction due to the lateral package walls mode of vibration. Considering the analysis frequency of 93 kHz, the case (d) shows a SPL polar plot characterized by a wide vertical lobe with maximum value at 90 degrees equal to 120 dB and two narrow horizontal side lobes with local maxima equal to 112 dB. The case (e), at 93 kHz, is characterized by higher directivity due to the presence of a narrower vertical lobe with maximum value equal to 116 dB and two specular side lobes with local maxima of 114 dB at 50-130 degrees, related to the protecting cap eigenmodes combination.

5.4.3 SPL polar comparison among different package configurations

Finally, in Fig. 5.31-5.34 the comparisons of SPL polar plots are reported, at a distance of 3.5 cm from the center of the die and in the vertical plane y-z, passing through the center of the system. To investigate the influence of the SPL shaped hole and compare the packaging solution with the same total holed area A_{hole} of the case (d), a new case (f) characterized by a single circular central hole as case (b) but with a larger hole radius equal to $R_{hole} = \sqrt{A_{hole}/\pi}$, has been considered, as well. The numerically compared packaging solutions are: case (d) with SPL shaped hole versus case (b) with protective cap hole of radius $R_{hole} = 2R_{PMUT}$ in which the total holed area is four times smaller than the case (d); case (d) versus case (f) with the same total holed area; case (a) with small hole of radius $R_{hole} = R_{PMUT}/3$ versus case (b); case (c) with a coaxial hole placed directly above the center of each transducer versus case (e) with random holes with the same total holed area. Two different analysis frequencies of 85.5 kHz and 93.0 kHz have been considered, corresponding to the fundamental performing frequencies of the PMUTs applying respectively 10 V and 3 V

bias.

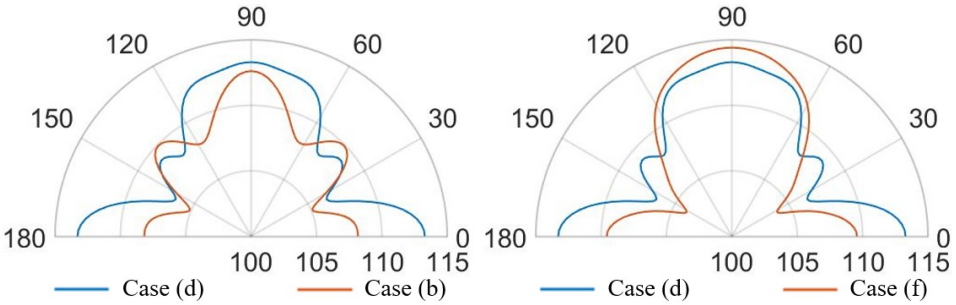

Figure 5.31: *SPL polar plot [dB] at the performing fundamental frequency of 85.5 kHz (10V bias), at 3.5 cm in the y(90 deg)-z(0 deg) plane: (d) vs (b) (left), (d) vs (f) (right).*

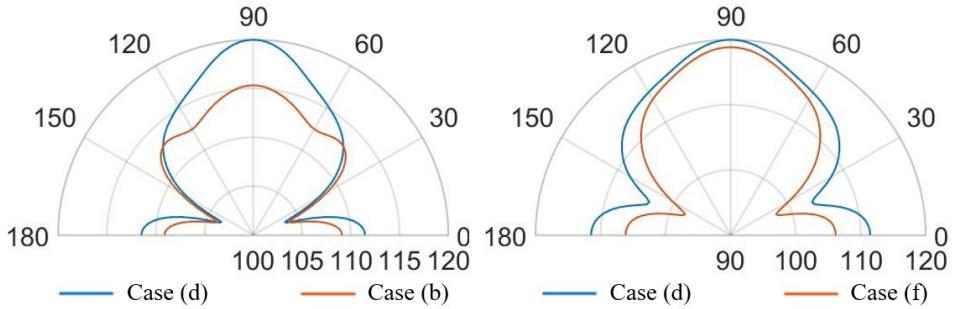

Figure 5.32: *SPL polar plot [dB] at the performing fundamental frequency of 93.0 kHz (3V bias), at 3.5 cm in the y(90 deg)-z(0 deg) plane: (d) vs (b) (left), (d) vs (f) (right).*

Concerning the comparison between the cases (d) and (b) in Fig. 5.31, the configuration (d) leads to greater propagation in the horizontal direction at 0-180 degrees. Hence, with the configuration (d), actuating the system at the fundamental frequency of 85.5 kHz causes the energy excites the eighth eigenmode (see Fig. 5.22), involving the intensively vibration of the package lateral walls as well. Moreover, along the vertical direction the (d) lobe is wider than (b) one with maximum value of 113 dB with respect 112.5 dB and the two symmetrical side lobes are farther from the vertical direction with lower SPL values of about 108.5 dB with respect to 110 dB.

Considering the comparison between the case (d) and (f) with the same holed area, the horizontal propagation is grater in case (d), while along the vertical direction of 90 degrees, case (f) shows a higher SPL value of about 114.5 dB and it tends to the situation of no package without any side lobes (see Fig. 5.15). As it can be noticed in Fig. 31, exciting the diaphragms at 93.0 kHz, the case (d) shows a main vertical lobe which without any side

lobes. The maximum value of SPL is reached at 90 degrees and it is equal to 120 dB, while the horizontal propagation is characterized by the local maximum equal to 112 dB. Concerning the case (b), one can observe that the polar shape is characterized by the main vertical lobe, two side lobes with local maxima at 45-135 degrees and 0-180 degrees. The difference in the beam pattern are related to the different eigenmodes involved during the vibration. Furthermore, considering the same holed area of the circular hole at the actuation frequency of 93.0 kHz, the particular lobe shape of the case (f) tends to that one of case (d).

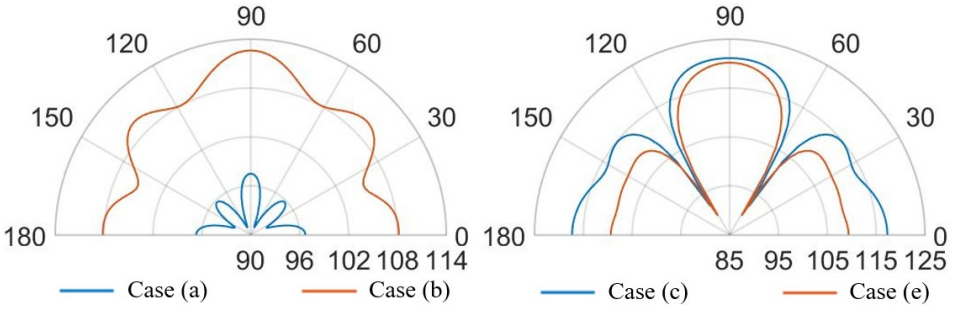

Figure 5.33: *SPL polar plot [dB] at the performing fundamental frequency of 85.5 kHz (10V bias), at 3.5 cm in the y(90 deg)-z(0 deg) plane: (a) vs (b) (left), (c) vs (e) (right).*

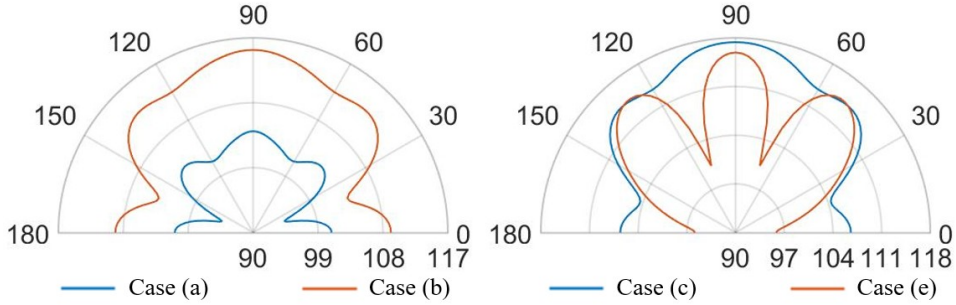

Figure 5.34: *SPL polar plot [dB] at the performing fundamental frequency of 93.0 kHz (3V bias), at 3.5 cm in the y(90 deg)-z(0 deg) plane: (a) vs (b) (left), (c) vs (e) (right).*

Comparing case (a) and case (b), at the two analysis frequencies, in Figs. 5.33-5.34, is worth noting that the lobe shapes between the two cases are the same. For case (a) the protective cap, with a smaller hole radius then that one of case (b), causes high obstructive effect leading to lower SPL values in every direction. In this two situation the SPL propagation polar plot of (b) encompass that one of case (a). The configuration (b) leads to higher SPL values, reduced and a wider lobe of propagation.

Focusing on Fig. 5.33, the comparison between case (c) and case (e), the shape of the vertical lobe is slightly narrower for case (e) and the intensities are almost the same, but the SPL maximum value are respectively 121 dB and 120 dB. This is due to the presence of the random configuration with a greater number of holes with smaller radii, characterizing the protective cap, which produces a greater obstructive effect than the case (c) in which a larger hole is present directly above each transducer. Concerning Fig. 5.34, the case (e) shows a propagation pattern with three well defined lobes at 90, 45-135 degrees with local maxima of 115 dB, while the case (c) shows a wider polar shape.

5.5 Closing remarks on the package effects

The design of PMUTs should be based on a reliable computational model, that includes the complex coupling among different physics and the interaction among different parts of the device. In this chapter, we have considered a 3D multiphysics model that encompasses the mechanical, piezoelectric and acoustic coupling to assess how the package affects the propagation patterns and the acoustic performances of the device considering two the different performing fundamental frequencies of 85.5 kHz (10 V bias) and 93 kHz (3 V bias).

Several simulations have been carried out: i) a geometrically non-linear static analysis to compute the pre-deflected configuration induced by the fabrication residual stresses; ii) a geometrically non-linear static analysis to compute the starting configuration under the bias voltage account taken the initial stress state; iii) an electro-mechanical eigenfrequency analysis, around the previously computed starting deformed configuration, due to the prestresses and the bias voltage, to evaluate the eigenfrequencies of the transducers and the vibration eigenmodes of the whole device; iv) an electro-mechanical-acoustic frequency analysis at 85.5 kHz an 93 kHz, around the starting deflected configuration, under a harmonic voltage perturbation with amplitude of 3 V and a constant bias voltage of 3 V and 10 V.

Several cases have been studied and for both the analysis frequencies of 85.5 kHz and 93.0 kHz, related to respectively 10 V and 3 V bias voltages, to evaluate the different package responses at different performing PMUTs fundamental frequencies.

The comparison between the unpackaged and the packaged systems with no vent shows, in the second case, a considerable reduction of SPL and an acoustic propagation essentially governed by the package vibration.

While, the package free system propagation pattern is characterized by the spherical waves composition coming from all the vibrating PMUTs.

The protective cap solutions show how the acoustic transmission efficiency is strongly influenced by the package presence. This is suggested by the decreasing values of SPL with respect to the unpackaged solution and by the different polar shapes. Nevertheless, the hole presence guarantees higher directivity than the package free case. Therefore, small hole package (a) determines lower SPL values, but induces a narrow lobe in the vertical direction, as it is reported in Fig. 5.25. Considering the cap with a central hole of radius equal to $R_{hole} = 2R_{PMUT}$, the SPL polar shape is wider and higher value of acoustic intensity are reached (see Fig. 5.25).

Solutions (c) and (e), respectively the case of a hole placed above each transducer and the random holed configuration, are strongly influenced by the analysis frequency. Actuating the vibration at 85.5 kHz induces a propagation pattern with the same shape of unpackaged one, but lower SPL value are reached due to the obstructive effect. While, at 93.0 kHz the acoustic transmission is basically related to the package modes of vibration and the two package cases (c) and (e) differ from the unpackaged one. Finally, the configuration (d) with central hole shaped like the SPL, is particularly efficient to guarantee the wave propagation along the vertical direction, with a wide lobe characterize by high vales of SPL from 60 and 120 degrees, at both performing frequencies (see Fig. 5.31-5.32). In this case, the involved vibration of the package walls determines the propagation along the horizontal direction and high SPL values are reached at 0-180 degrees, as well.

Future developments will be oriented to the study of different performing frequencies with the applied bias, to evaluate the influence on the acoustic intensity and directivity with respect to the considered package configuration. Furthermore, several analyses will be carried out, varying the distance of the package from the die, the thickness of the package and the hole configuration, to evaluate the effects on the propagation modes and the performances.

CHAPTER 6

Non-linear vibrations in PMUT devices

This chapter is focused on the non-linear dynamic response of PMUT transducers. When the non-linear oscillations are activated by the involved large displacements, the system shows an initial amplitude modulation with small steady state amplitude increments as the voltage input increases at constant frequency. Two numerical models are developed to simulate the complete performance of the system based on the response of the diaphragm.

In the former, the electro-mechanical-acoustic (EMA) problem for the single PMUT is solved, in the time and frequency domains, exploiting the axial symmetry of the system, with the following features: the presence of the fabrication induced residual stresses; the multiple couplings between different physics, namely piezoelectric coupling in the active layer and acoustic-structural interaction for the waves propagation in the surrounding fluid.

In the latter model, the full set of PMUTs belonging to the silicon die in a 4 x 4 array configuration is considered in which the vibrating plates are modelled as equivalent oscillating rigid plane circular pistons, with reduced imposed acceleration amplitude, on a rigid baffle represented by the remaining part of the surface die.

The results of the numerical simulations are compared with the experimental ones in terms of the initial static predeflection, transmitted pressure at 15 cm and 3 cm from the center of the diaphragm, along its own vertical acoustic axis, and non-linear frequency displacement amplitude response functions of the PMUT center.

6.1 Introduction

Several examples of air-coupled PMUTs are present in the literature, characterized by operating frequency above 200 kHz [25]. The difference in the frequency introduces an extra effort in the modelling, due to the geometric non-linearities activated by the high diameter/thickness aspect ratio of the considered transducers [104, 105] (refer to Fig. 6.1).

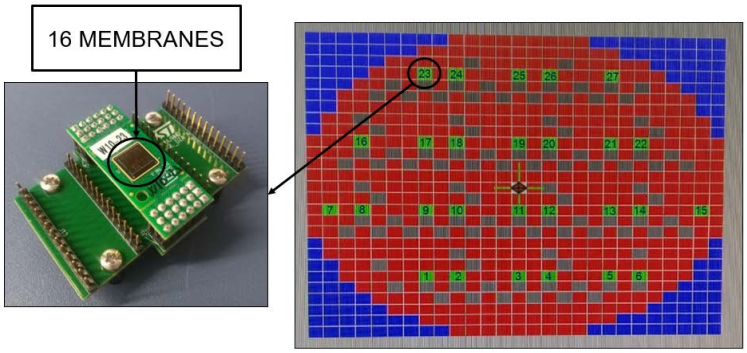

Figure 6.1: *View of the 4x4 array of circular transducers (left); position of the sample on the wafer map (right).*

In the previously chapters 4 and 5 the in frequency domain response has been simulated. The primary aim of the present chapter is to simulate the in-time non-linear dynamic behaviour in the vertical oscillation of the plate [106], generating the pressure waves propagation into the fluid, due to the involved large displacements [107–109], associated with a voltage threshold over which the amplitude increases very slowly with respect to the provided input voltage.

Then, the array response is simulated by a further stage, in which an equivalent rigid piston-like vibration modelling of the transducer is adopted, while the remaining part of the silicon die is assumed to be rigid, allowing one to solve only the acoustic problem in the surrounding fluid. This approach represents a useful tool to study the pressure propagation problem with acceptable computational cost, with respect to the burdensome complete fully coupled electromechanical-acoustic model, used to simulate the single transducer performance.

Furthermore, the influence of the static voltage on the initial deflected configuration and the fundamental frequency is shown, referring to the measured topographies by means of the Polytec MSA-500. Additional considerations are based on the comparison between the measured and simu-

lated hard/soft spring frequency response functions curve of the system. They have been obtained through an up frequency sweep at different constant bias voltage and excitation amplitudes. The displacement at the center of the membrane has been collected at the steady state, for each selected input frequency and bias.

The chapter is organized as follows. In the second section, the EMA numerical modelling of the circular clamped single diaphragm, with its own air-filled closed cavity, is described in the 2D axial-symmetric meridian half plane, together with the 3D acoustic model of the 4x4 array of transducers, in which the layered diaphragms are replaced by equivalent vibrating pistons, to simulate the in parallel TX phase. In section third, first the experimental tests are shown to validate the numerical results for the single transducer, in the mechanical and in the acoustic domains, then the numerical predictions for the array of PMUTs are presented and compared with the single transducer ones. Finally, last section is devoted to some closing remarks.

6.2 Numerical modelling

This section is focused on the two numerical models built in COMSOL Multiphysics 5.4, adopted in the solution strategy to simulate the single transducer and the array of PMUTs.

In the former, the axial-symmetry of the problem is exploited modelling the diaphragm and the cavity in the meridian half space. The transducer has radius of 440 μm and an overall thickness equal to 8 μm, such that the diameter/thickness ratio is 110. The structural layer is made of silicon with thickness equal to 4.25 μm. The PZT layer has thickness of 1.06 μm and is in a circular configuration with radius of 308 μm, coaxial with the diaphragm. The plate is clamped over an air-filled closed cylindrical cavity with height of 400 μm and the same radius of the upper diaphragm.

The model, shown in Fig. 6.2, is described by: elastodynamics in the linear elastic layered system, electrostatics in the piezoelectric layer with the linear stress-charge law and pressure acoustics in the fluid cavity and in a half semi-circular fluid domain with radius equal to 2λ, where $\lambda = c/f_0 = 3434$ μm is the wavelength, $c = 343$ m/s is the speed of sound in the air at the reference state of $T_{ref} = 293.15$ K and $P_{ref} = 1$ atm and $f_0 = 100$ kHz is the performing frequency of the system, while the calculated Rayleigh distance is equal to $D_R = S/\lambda = 177.1$ μm, where S is the PMUT area [40].

The residual stresses are taken into account by an amount of pre-stress

acting in the plane of each layer, so that the cross section is characterized by tensile and compressive initial stresses.

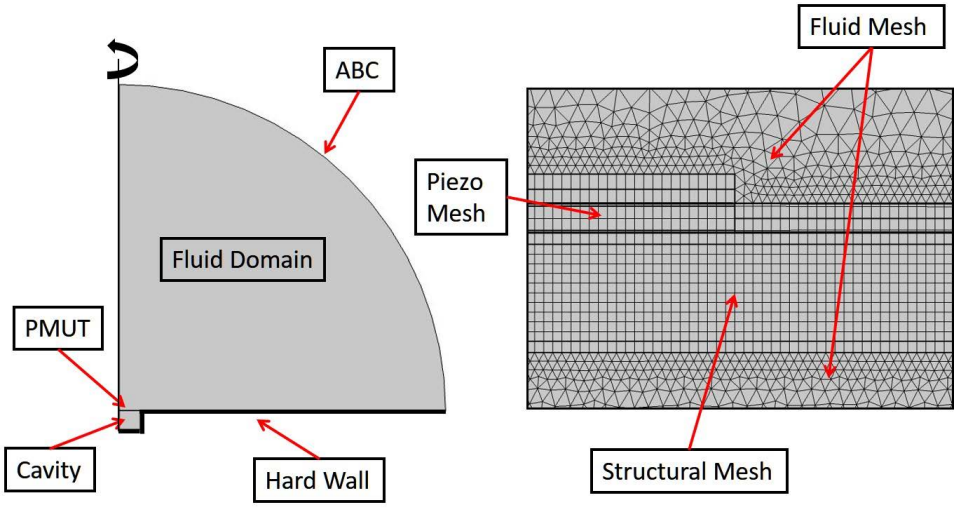

Figure 6.2: *2D axial-symmetric single transducer model (left); PMUT and fluid mesh detail: 3-node triangular fluid elements, 4-node quadrilateral solid elements (right).*

To simulate the several energy losses (thermo-elastic losses, surface and interface dissipation and anchor losses), during the vibration at the fundamental eigenfrequency, a proper damping ratio is taken into account by means of the Rayleigh damping formulation into the elastodynamics equations, while the fluid is considered non-dissipative with no thermo-viscous modelling of the air [73, 74]. The computed Rayleigh parameters [110] refer to $\xi = 1/(2Q_{struct})$ where Q_{struct} is the imposed structural quality factor of the fundamental electro-mechanical eigenmode. Moreover, the radiation is simulated into an infinite medium through the absorption condition at the fluid circular boundary, while on the surface of the cavity and on the remaining acoustic boundary a hard wall condition is imposed.

The electro-mechanical-acoustic response, around the initial deflected configuration of the system, due to the pre-stress state, is obtained under a voltage input sinusoidal excitation at the previously computed linearized fundamental electro-mechanical resonance frequency, including the non-linear effects due to the adopted large displacements formulation [111–116]. The vertical spatial mean acceleration time history can be extracted at the fluid-structure interaction surface.

The latter model, used for the PMUTs array performance simulation, is characterized by two orthogonal symmetry planes passing through the

device where symmetry boundary conditions are enforced (see a detail in Fig. 6.3).

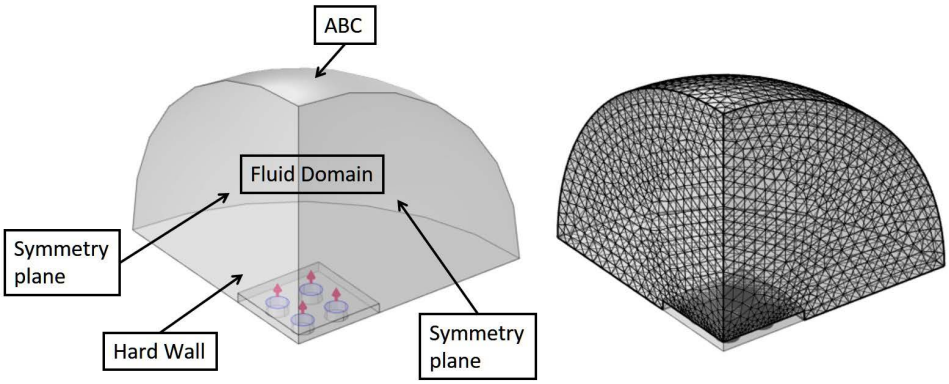

Figure 6.3: *3D Acoustic model, a quarter of a 4x4 array of PMUTs with imposed vertical acceleration on the equivalent pistons (red arrows); fluid mesh detail: 10-node tetrahedral elements (right).*

The acoustic wave problem is therefore solved in a quarter of a hemispherical no dissipative fluid domain [40, 117, 118], with radius equal to 3λ, considering the presence of a quarter of die with full size equal to 7.2x7.2x0.4 mm^3.

Accordingly, a set of 2x2 transducers are modelled as equivalent vibrating baffled rigid pistons, on the die surface, characterized by the same area of the diaphragm and with imposed vertical mean acceleration, previously computed by means of the 2D model for the complete PMUT stack. The absorbing boundary condition is considered, also at this stage, at the fluid spherical boundary to simulate the infinite radiation, together with the symmetry condition on the two vertical planes and the hard wall condition on the remaining surfaces.

The acoustic response is estimated in the fluid domain in terms of pressure map and time history along the vertical acoustic axis passing from the center of the device.

6.3 Results and experimental validation

The single transducer model captures the pre-deflected configuration and the linearized electro-mechanical fundamental eigenfrequency of the transducer. The experimental initial vertical displacement of the center of the plate is equal to 5.2 μm (Fig. 6.4) while its numerical prediction is equal to 4.9 μm; a substantial fundamental mode eigenfrequency shift from 111.5

kHz to 100.0 kHz is associated to the fabrication residual stress state (refer to Fig. 6.11). The mismatch in the pre-deflection can be attributed to the uncertainty in the pre-stresses of the different layers.

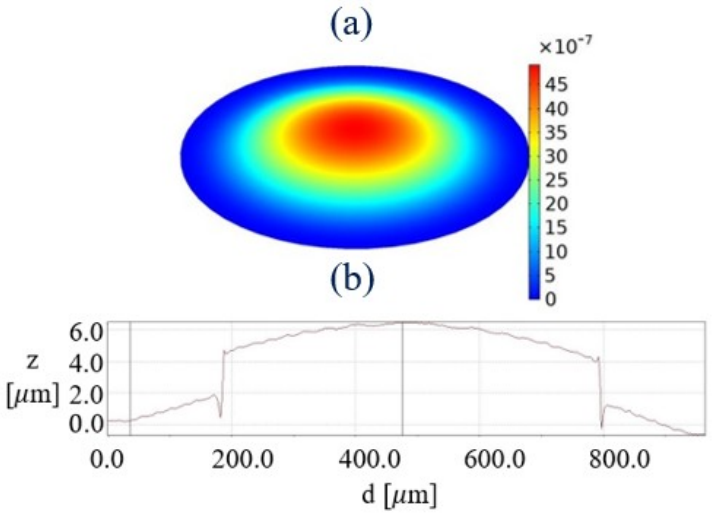

Figure 6.4: *Initial static transversal displacement in μm: numerically computed by means of COMSOL Multiphysics 5.4 (a); experimental profile by means of Polytec MSA-500 (b).*

An experimental campaign, by means of Polytec MSA-500 (Fig. 6.5), has been carried out on 16 PMUTs. The deformed profiles along a diameter, measured by means of the white-light interferometry, are shown in Figs. 6.6 and 6.4 (b) where the PZT hat layer appears about 2 μm thick, instead of 1.06 μm, due to the silicon refractive index compared to the top electrode one. It is worth noting that, because of the noise of the measure, a filter has been applied to the case of $V_{bias} = 0$ V, to get a smoother profile, as a consequence no jump in the PZT thickness appears.

The topography of each membrane and the displacement profile, along the diameter of the transducer, is extracted. The test shows how the application of a constant bias voltage affects the initial static configuration (Fig. 6.6).

The vertical static displacement at the center of the PMUTs is extracted and plotted at different constant bias voltage. Fig. 6.7 (on the left) shows the initial vertical displacement of each transducer, in correspondence of $V_{Bias} = 0$ V, is upward and falls within a range of 3.5 μm to 5.5 μm. The difference in the pre-deflected configuration is related to the difference in the pre-stress state of the layers of the die.

Increasing the value of the constant bias voltage, starting from 0 V to

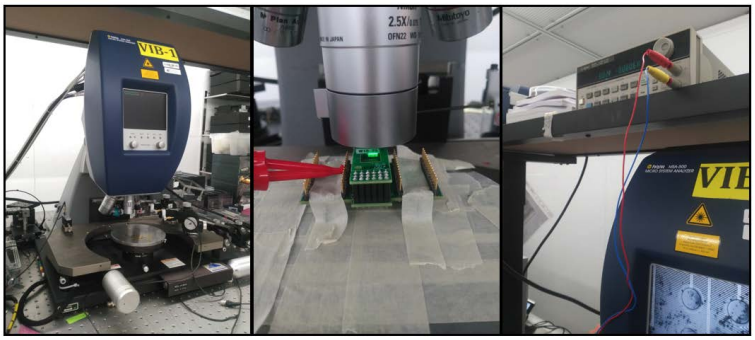

Figure 6.5: *Polytec MSA-500 (left); measurements setup detail (center); external generator for the actuation of the membranes (right).*

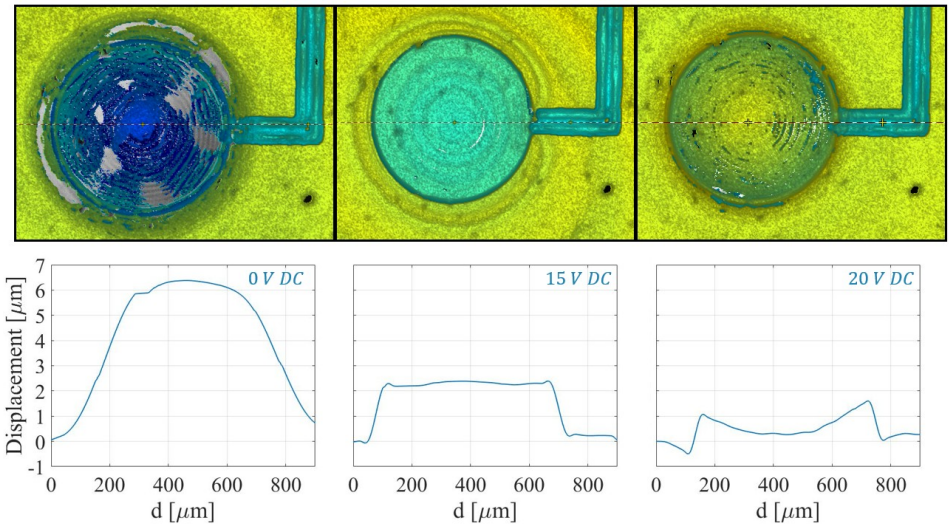

Figure 6.6: *Topography of one membrane of the array for different constant bias voltage: 0 V DC (top left), 15 V DC (top center), 20 V DC (top right); initial static transversal displacement in μm: experimental measurement by means of Polytec MSA-500 for each case (bottom).*

20 V, the value of the vertical displacement at the center of the transducer decreases. The displacement becomes negative and the initial pre-deflected configuration changes concavity (as shown in Fig. 6.6).

Moreover, the resonance frequency of the system has been measured by means of Polytec MSA-500 laser-doppler vibrometer applying a pseudo-random excitation. Fig. 6.7 reports that it decreases reaching the minimum value between 14-16 V. The constant bias voltage allows to compensate the initial stress state inside the diaphragm bringing the system back to the undeformed reference configuration, associated to the case of no pre-stress applied. Through this process, the stiffness of the system decreases until the membrane changes concavity, then the stiffness starts again to increase as well as the resonance frequency of the transducer.

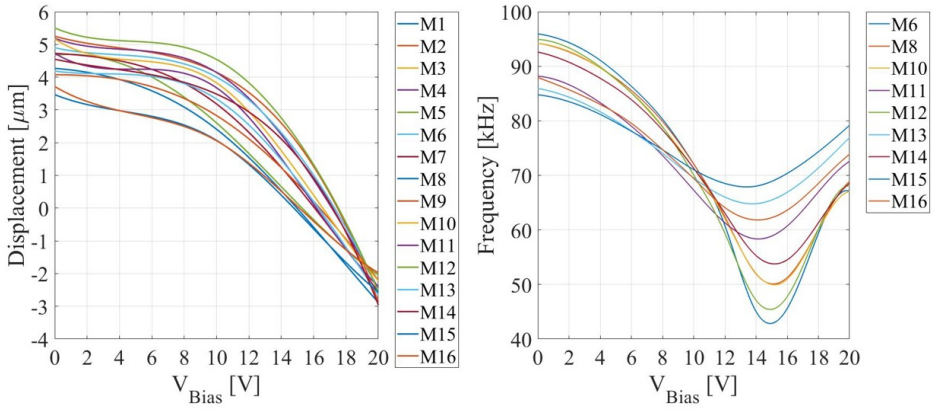

Figure 6.7: *Experimental measurements: constant bias voltage influence on the vertical displacement (left); constant bias voltage influence on the resonance frequency (right).*

Applying a constant voltage difference to the PZT electrodes results in an imposed stress distribution, due to the piezoelectric effect, that determines the deformed configuration. The trend in Fig. 6.7 shows the reverse static configuration of the plate occurs increasing the voltage beyond a specific threshold for each PMUT, in the range of 15 V to 17.5 V. The fundamental resonance frequency of the system is affected by the membrane stresses [112, 113, 119, 120]. The initial stress state, in correspondence of $0V_{Bias}$ at the center of the membrane, is characterized by a compressive membrane stress resultant that becomes larger, increasing the voltage while the system tends to the flat configuration. Hence, the fundamental frequency decreases with the voltage while the center displacement approaches 0 μm. Increasing the voltage beyond the flat threshold, the diaphragm shows the reverse configuration and consequently the

reverse internal stress state. Therefore, the stresses at the center of the membrane are characterized by a tensile membrane resultant and the fundamental frequency increases with the voltage while the magnitude displacement becomes larger and oriented downward. A set of analyses in the time domain are performed with the purpose of investigating the voltage threshold amplitude, over which the oscillating behavior of the transducer shows a non-linear dynamic response [121–126]. The considered excitation is a 100 cycles sinusoidal at the linearized fundamental eigenfrequency $f_0 = 100.0$ kHz. The results are reported in Fig. 6.8 in terms of pressure vs. time histories at 15 cm, on the vertical acoustic axis of the diaphragm for different provided input voltage amplitudes with zero bias voltage. The responses have been obtained assuming a decreasing relation as $1/r$ beyond the computational domain in which the propagation can be considered spherical [40]. The results include the damped free decay oscillating part after the excitation stops.

The numerical results are in good agreement with the recorded experimental pressure histories, obtained by means of a Brüel & Kjær $1/8$" microphone type 4138 with sensitivity at 100 kHz equal to 89.12 mV/Pa, as it is shown in Fig. 6.9, in which the non-linearity threshold voltage amplitude coincides with 400 mV.

The system shows the amplitude modulation as the non-linearity are active due to the fact that the excitation frequency is fixed at the linearized fundamental eigen-frequency while the real resonance frequency, that depends on the oscillation amplitude in the non-linear regime, slightly shifts.

Figure 6.10 shows, numerically and experimentally, the effect of increasing the voltage amplitude up to 800 mV: small increments of pressure amplitude are observed with respect to the values obtained at the estimated linear limit of 400 mV.

The Q-factor of the transducer has been measured by means of a free vibration decay test and corresponds to $Q_{tot} = 74$. It depends on several sources of energy losses: structural losses Q_{struct}, such as thermoelastic, support, surface layer losses, and fluid losses Q_{fluid}, related to the energy radiation into an infinite medium in the air. In the electromechanical-acoustic single transducer model, considering the absorbing condition at the fluid boundary, a numerical $Q_{struct} = 104$ of the fundamental mode has been imposed to obtain the acceptable match between the numerical and the known experimental Q_{tot}. Accordingly, the numerical $Q_{fluid} = 258$ has been computed subtracting the inverse of Q_{struct} to the inverse of the Q_{tot} and extracting the inverse of the result (as common in parallel impedance reduction) [78].

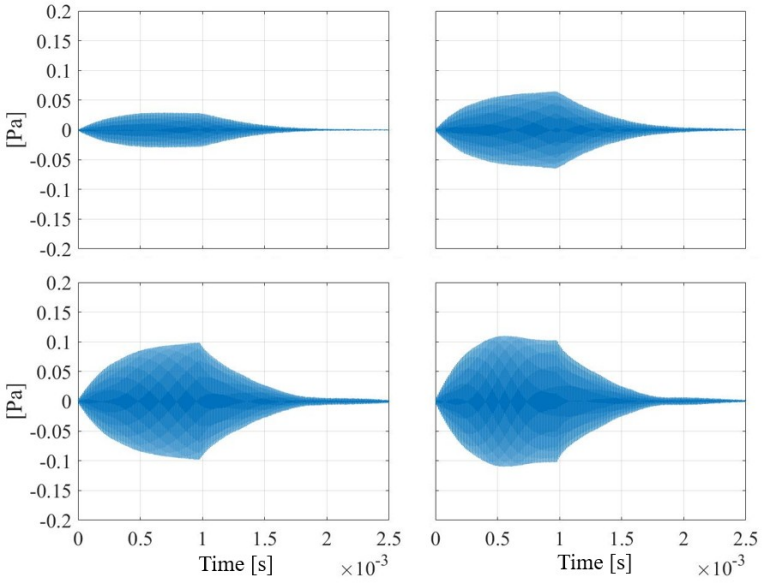

Figure 6.8: *Numerical pressure time histories at* 15 *cm on the vertical acoustic axis of the transducer.* $V_{AC} = 100$ *mV (top left),* 200 *mV (top right),* 300 *mV (bottom left),* 400 *mV (bottom right).*

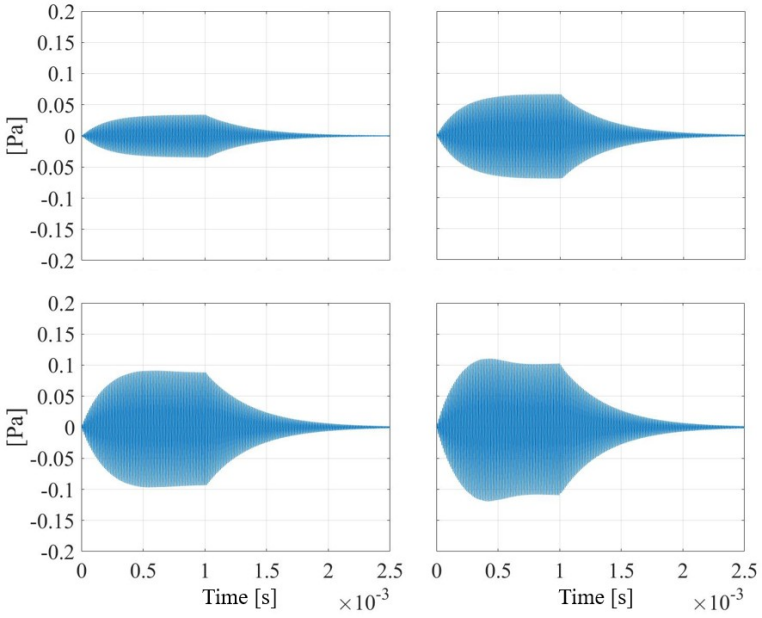

Figure 6.9: *Experimental pressure time histories at* 15 *cm on the vertical acoustic axis of the transducer.* $V_{AC} = 100$ *mV (top left),* 200 *mV (top right),* 300 *mV (bottom left),* 400 *mV (bottom right).*

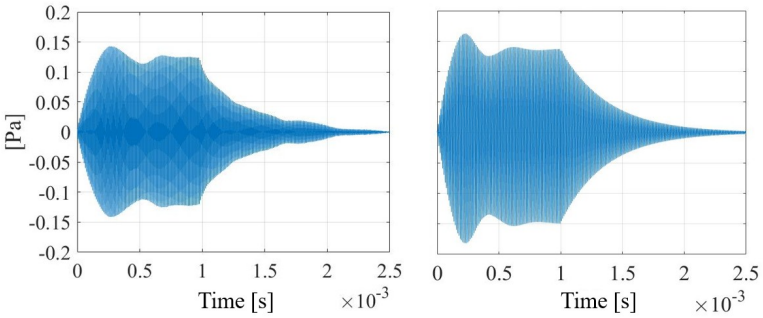

Figure 6.10: *Pressure time histories at* 15 *cm on the vertical acoustic axis of the transducer at* $V_{AC} = 800$ *mV amplitude: experimental (left), numerical (right).*

As reported in Figs. 6.8 and 6.9 for the single transducer TX test, considering a sinusoidal voltage amplitude $V_{AC} = 100$ mV, the experimental steady state pressure amplitude is equal to 0.0328 Pa in very good agreement with the corresponding numerical value of 0.0338 Pa which respectively are 61.30 dB and 61.54 dB.

To investigate the non-linear behaviour a new set of measurements and corresponding analyses in the time domain have been performed, confirming the robustness of the procedure. The applied excitation has been set to 90 sinusoidal cycles at the linearized fundamental eigenfrequency $f_0 = 87.3$ kHz.

The electro-mechanical-acoustic frequency sweep analysis has been performed with a harmonic voltage excitation amplitude of 200 mV and 2 V DC voltage bias, around the fundamental frequency. The result of the study in terms of normalized vertical displacement amplitude spectrum of the center of the PMUT, is reported in Fig. 6.11 together with the experimental one. The measured spectrum, obtained through the Polytec MSA-500 laser-doppler vibrometer, is related to a pseudo-random noise excitation with 1V amplitude and 2 V DC voltage bias, provided to the PZT electrodes, ranging from 10 kHz to 1 MHz.

Furthermore, the numerical pressure histories have been computed. They are in good agreement with the recorded experimental pressure histories, by means of the Brüel & Kjær $1/8$" microphone type 4138, shown in (Fig. 6.12).

Moreover, Figs. 6.13 and 6.14 show the comparison between the experimental and numerical results in term of pressure time histories at 3 cm from the die, along the vertical acoustic axis of the transducer at different provided input voltage amplitudes with 2 V DC constant bias voltage.

The measured sample shows a non-linear dynamic threshold around 300

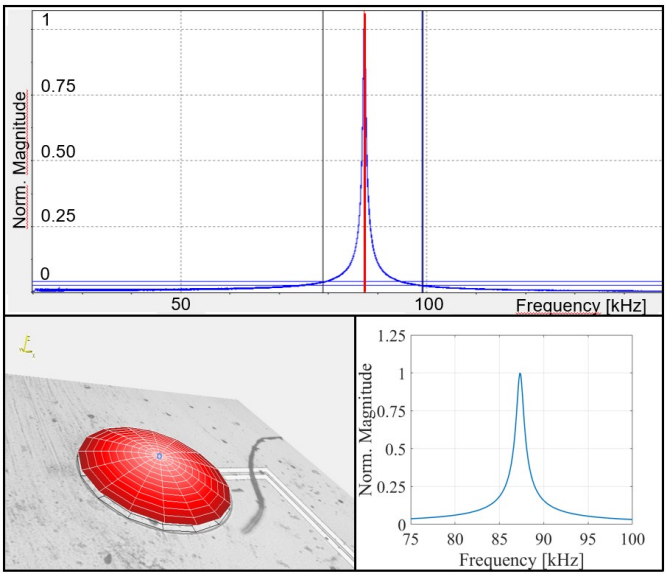

Figure 6.11: *Experimental (top) and numerically (bottom right) computed transversal displacement frequency normalized amplitude spectrum, at the center of the PMUT, by means of COMSOL Multiphysics 5.4; 1^{st} mode shape of the transducers recorded by means of Polytec MSA-500 (bottom left).*

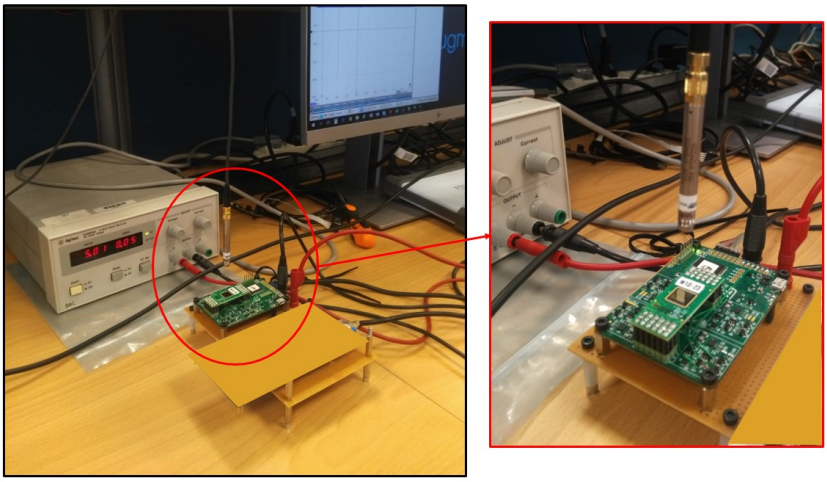

Figure 6.12: *Experimental microphone setup for the acquisition of the PMUTs time histories: overview of the generator, die on board and microphone (left); detail of the microphone at 3 cm from the die (right).*

mV. The non-linear threshold is slightly lower than the first sample one. As a matter of fact, the imposed constant bias voltage reduces the stiffness of the system. As a consequence, the fundamental frequency decreases, the vibration amplitudes, that affect the stiffness, increase at the same voltage levels and the non-linear phenomenon occurs in correspondence of lower VAC.

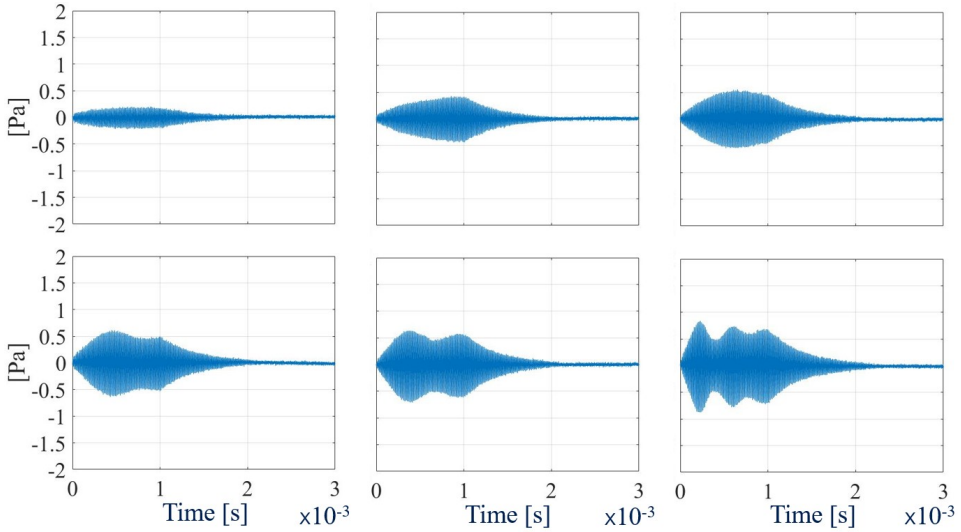

Figure 6.13: *Experimental pressure time histories at 3 cm on the vertical acoustic axis of the transducer.* $V_{AC} = 100$ *mV (top left), 200 mV (top center), 300 mV (top right),* 400 *mV (bottom left), 500 mV (bottom center), 1 V (bottom right).*

The non-linear dynamic behavior of the system has been investigated, evaluating the amplitude frequency response function curves of the transducer at different voltage amplitudes.

The experimental data have been obtained by means of a series of in time domain vibrometer measures through the Polytec MSA-500. The experimental procedure consists in collecting the displacement oscillation amplitude at the steady-state, sweeping up the input frequency of the excitation at different VAC. Hence, a plot of the displacement amplitude vs. input frequency has been reconstructed and reported in Fig. 6.15. The linearized fundamental frequencies has been previously measured by means the pseudo-ramdom vibration testes (see Figs. 6.7 and 6.11).

The corresponding numerical results have been computed considering two different voltage input amplitudes of $V_{AC} = 0.7$ mV and $V_{AC} = 1.4$ mV and two voltage bias of $V_{DC} = 2$ V and $V_{DC} = 12$ mV. Therefore, the related normalized amplitude frequency response functions are shown

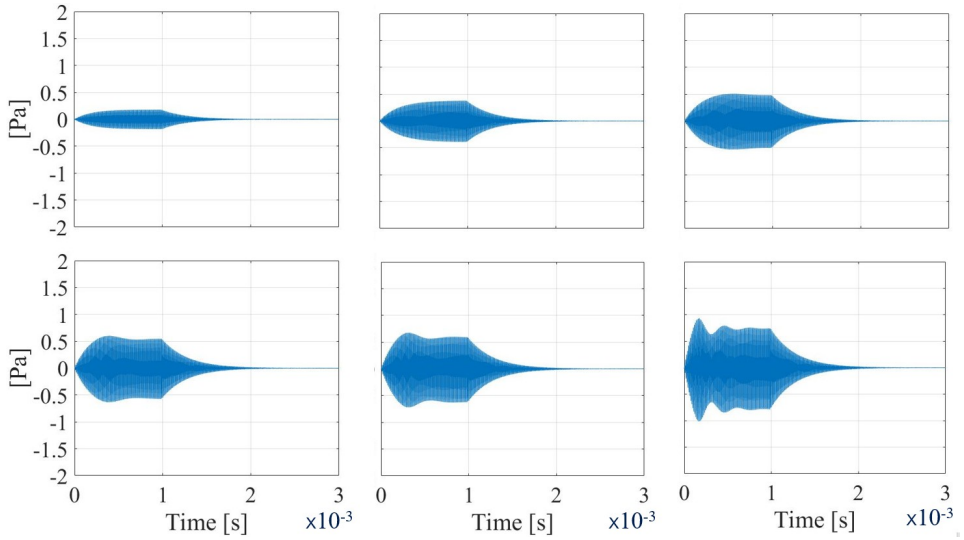

Figure 6.14: *Numerical pressure time histories at 3 cm on the vertical acoustic axis of the transducer. $V_{AC} = 100$ mV (top left), 200 mV (top center), 300 mV (top right), 400 mV (bottom left), 500 mV (bottom center), 1 V (bottom right).*

in Fig. 6.16.

Fig. 6.15 shows the effect of increasing the V_{AC} excitation voltage amplitude at two different constant bias voltages. Focusing the attention on the left graph with $V_{DC} = 2$ V, the system, for low values of V_{AC} shows a linear behavior and the maximum value occurs very close to the linearized meausred resonance frequency. Increasing the excitation amplitude above $V_{AC} = 400$ mV, the non-linear soft spring behavior arises and the amplitude jump appears. While, in the case of $V_{DC} = 12$ V the non-linear hardening behaviour occurs above the voltage threshold of $V_{AC} = 700$ mV.

This behavior is related to the influence of the vertical oscillation, on the stiffness of the prestressed and predeflected system, as happens in the large flexural vibrations of the initially stressed shallow shells and arches. [105, 107, 113, 123, 127–130]. As the vertical oscillation becomes relevant, it affects the stiffness and consequently the fundamental frequency of the system so that the non-linear transient vibrations, observed in the pressure histories in Figs. 6.8-6.10-6.13, occur resulting in a frequency response depending on the displacement amplitude.

Therefore, the non-linear trend is determined by the contribution to the stiffness of the membrane axial force, induced by the combination of the prestress state and the static bias voltage and by the effect on the elastic stiffness due to influence of the initial deformed reference configuration

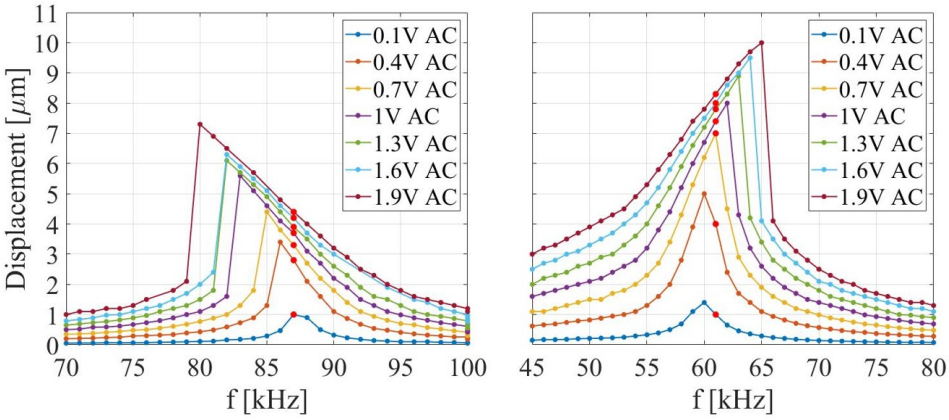

Figure 6.15: *Experimental soft-spring curve: $V_{DC} = 2$ V, V_{AC} sweep. Red dots are associated with the linearized resonance frequency $f_0 = 87.3$ kHz (left); experimental hard-spring curve: $V_{DC} = 12$ V, V_{AC} sweep. Red dots are associated with the resonance frequency $f_0 = 61.3$ kHz (right).*

induced by the combination of the prestress state and the static bias voltage, as well [123, 131–133]. Concerning the case in Fig. 6.15 on the right, applying a constant bias voltage $V_{DC} = 12$ V the predeflected configuration tends to be flat, as it is shown in Fig. 6.7. As a matter of fact, at the center of the PMUT the membrane stress resultant due to the static voltage is compressive while the bending resultant moment has the reverse sign of that one induced by the residual stresses, consequently the reduction in the linearized frequency and the restored flat configuration occur.

Therefore, the system shows higher displacement amplitudes at the same applied V_{AC} than the case with $V_{DC} = 2$ V, and the non-linear hardening trend, typical of the linear elastic flat axial-symmetric plates and rectilinear beams [125, 134, 135]. The numerical results, for the two cases of $V_{AC} = 0.7$ mV and $V_{AC} = 1.4$ mV are reported in Fig. 6.16. As a result of the 2D axial-symmetric single transducer TX simulation, the spatial mean vertical acceleration of the PMUT, over the fluid-structure interaction surface, can be computed providing the input for the next stage with the array model.

In the 3D acoustic array simulation, the previously calculated mean vertical acceleration, has been imposed on the mapped diaphragm areas on the rigid die, reducing the vibrating transducers to an oscillating rigid baffled piston.

Therefore, for the case of $V_{AC} = 100$ mV of the $4x4$ in parallel TX actuation, the following pressure map at the steady state time equal to $t = 1.02$ ms, just before the excitation stops, is shown in Figs. 6.17 and 6.18.

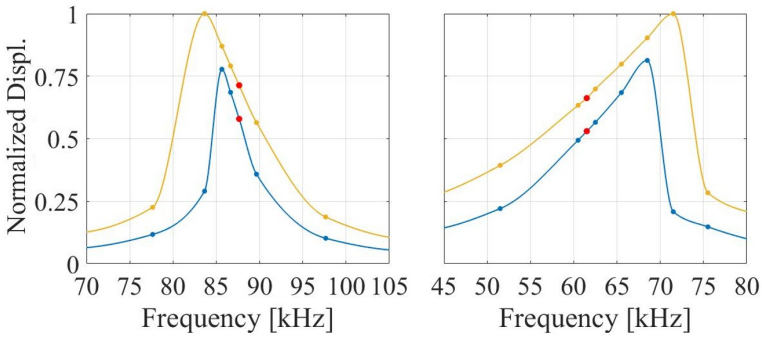

Figure 6.16: *Numerical soft-spring curve: $V_{DC} = 2$ V, $V_{AC} = 700$ mV (blue line), $V_{AC} = 1.4$ V (yellow line). Red dot is associated with the linearized resonance frequency $f_0 = 87.5$ kHz (left); numerical soft-spring curve: $V_{DC} = 12$ V, $V_{AC} = 700$ mV (blue line), $V_{AC} = 1.4$ V (yellow line). Red dot is associated with the resonance frequency $f_0 = 61.5$ kHz (left)*

As it can be notice, the wave front is flat near to the die and become spherical increasing the distance from that.

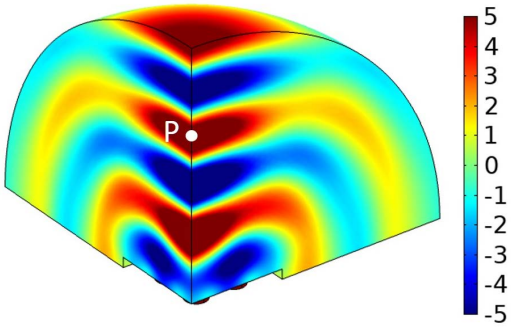

Figure 6.17: *Pressure map [Pa] at $t = 1.02$ ms. Point P at coordinates $(0, 0, 2\lambda)$.*

Figure 6.19 shows the pressure time history evaluated at point P depicted in Fig. 6.17, placed on the vertical acoustic axis which crosses the centre of the die at the distance of 2λ.

To evaluate the performance of the in parallel actuation of the 4x4 array of PMUTs, it is interesting to compare this result with the pressure history generated by the actuation of the single transducer at the same point, obtained by the 2D axial-symmetric model, and shown in Fig. 6.20. (see the depicted point in Fig. 6.21).

In this case, the pressure amplitude is 10 times lower with respect to the case of the 4x4 in parallel actuation, due to the fact that 16 transducers are active and the wave front tends to the spherical configuration at a larger

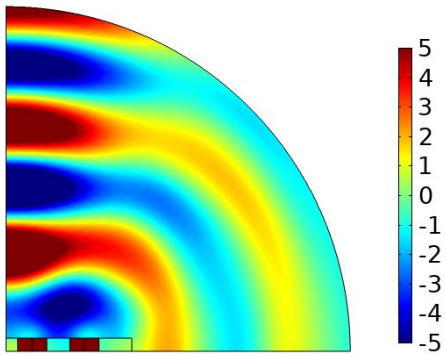

Figure 6.18: *Pressure map [Pa] at $t = 1.02$ ms in the vertical symmetry plane.*

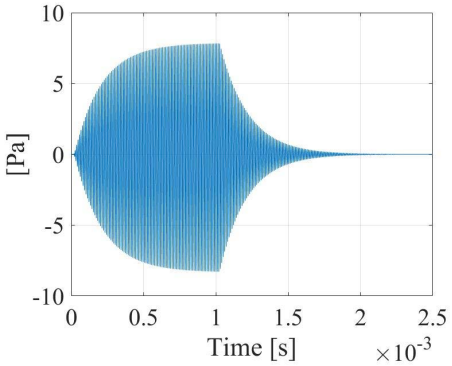

Figure 6.19: *Numerical pressure time history at the point P on the vertical acoustic axis of the array of PMUTs.*

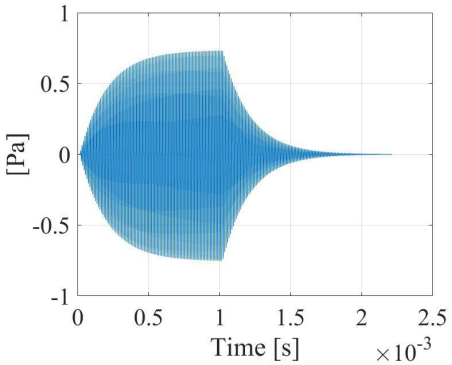

Figure 6.20: *Numerical pressure time history at the point P on the vertical acoustic axis of single transducer.*

distance with respect to the wave front created by the single transducer actuation. This is confirmed by the corresponding pressure map at the time instant $t = 1.02$ ms represented in Fig. 6.21, where the point P, which belongs to the external fluid boundary, is depicted in the 2D electromechanical-acoustic model.

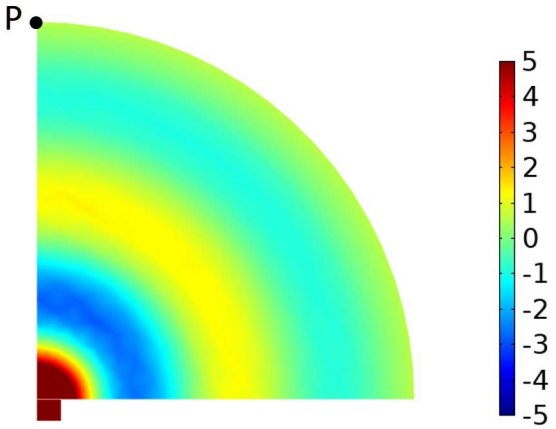

Figure 6.21: *Pressure map [Pa] at* $t = 1.02$ *ms. Point P at coordinates* $(0, 2\lambda)$

Different types of actuation have been simulated to investigate the acoustic performance at $9\ \lambda$, from the center of the die, illustrated in Fig. 6.22.

The actuation type affects the pressure maps in the fluid domain and each case is associated with a proper propagation pattern reported in Fig. 6.23.

The considered acoustic domain has radius equal to $9\ \lambda$, which means that the pressure time history evaluated at point $\mathrm{P}(0, 0, 9\lambda)$ belongs to the fluid boundary. The pressure comparison at point P is reported in Fig. 6.24.

The computed pressure time history at point P are similar. The time delay is clearly visible at the beginning, corresponding to the TOF. The case a) result in a slightly higher steady state pressure than other ones. This is due to the fact that, according the analysed actuation, the acoustic waves mainly propagate along the vertical axis of the device with the presence of side lobes of propagation.

This procedure can be used to preliminary assess the wave propagation coming from an array of transducers.

6.4 Closing remarks on the non-linear vibrations in PMUTs

In this chapter the results obtained with a multi-physics modelling of a single air-coupled PMUT in the time domain are presented, together with

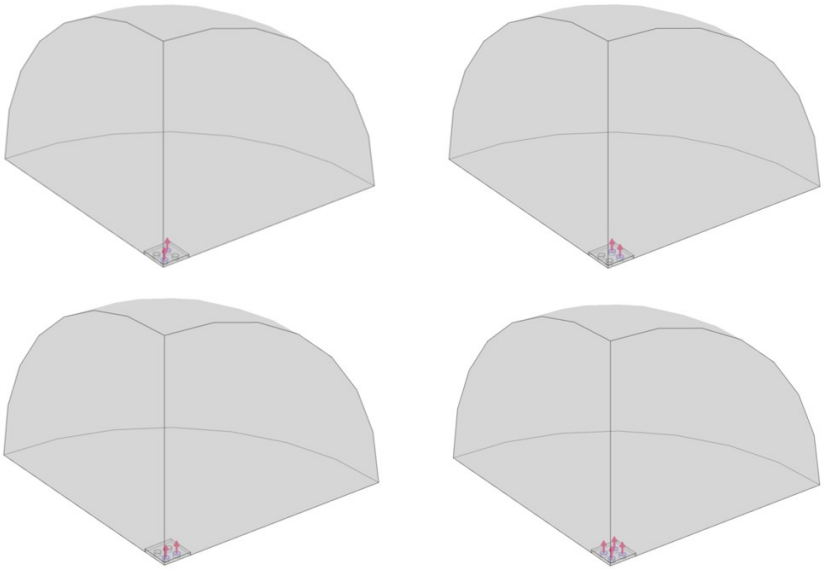

Figure 6.22: *Different cases studies: diagonal actuation (top left), external actuation (top right), internal actuation (bottom left), delayed actuation (bottom right)*

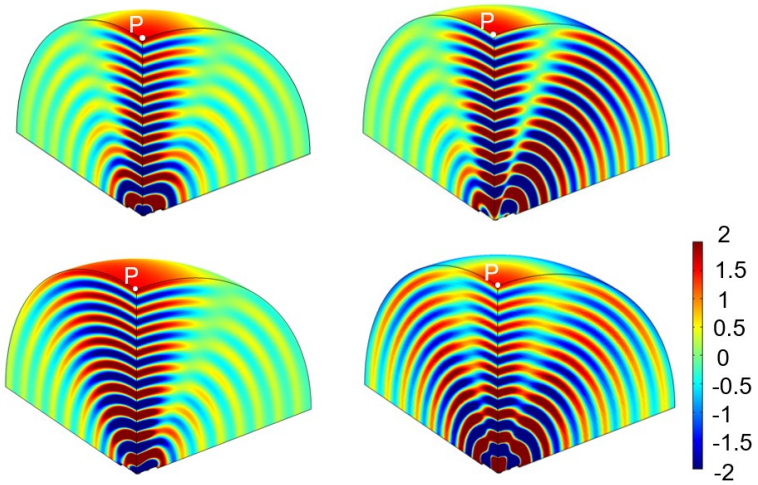

Figure 6.23: *Pressure map for the different cases study: a) diagonal actuation (top left), b) external actuation (top right), c) internal actuation (bottom left), d) delayed actuation (bottom right)*

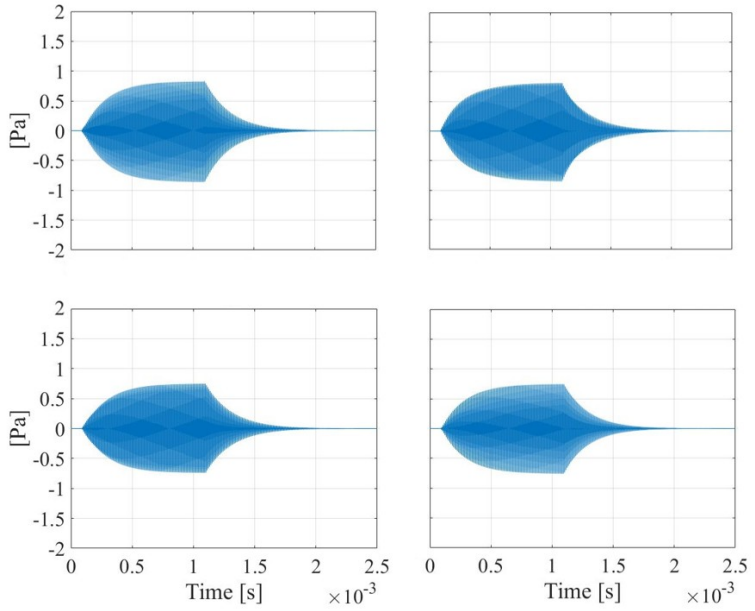

Figure 6.24: *Pressure time history at point $P(0, 0, 9\lambda)$ for the different cases study: diagonal actuation (top left), external actuation (top right), internal actuation (bottom left), delayed actuation (bottom right)*

their experimental validations for the mechanical and acoustic responses.

The influence of non-linearity on the diaphragm vibration has been studied for the fully coupled electromechanical acoustic problem, providing the linearity limit for the transducer performance. Loading the system with an increasing voltage input amplitude at the linearized fundamental electromechanical frequency, the recorded experimental pressure histories suggest a non-linear dynamic behavior of the PMUT.

The proposed single transducer model represents a suitable tool to estimate the non-linear voltage threshold, over which the pressure amplitude slowly increases with the input amplitude and any linear equivalent electrical lumped model of the PMUT fails.

The pressure propagation problem has been studied by means of an acoustic 3D model of the 4x4 array of PMUTs, considering the equivalent piston-like oscillation of the transducers, in the case of parallel actuation.

Work in progress includes numerical simulations of different array actuations and configurations to study the beamforming and the RX problem, including the package influence, together with their experimental validation.

To include the cross-talk among the elements of the array, a reduced or-

der description of the plates is needed, to condensate the dynamic behavior into few dofs and couple all the vibrating systems with the fluid domain.

CHAPTER 7

Model order reduction applied to in-water large arrays of PMUTs

In this chapter a new multiphysics Reduced Order Model (ROM) for the electro-mechanical-acoustic problem is presented. The Model Order Reduction (MOR) solution strategy consists of two main stages. In the former one, the eigenvalue piezoelectric problem is solved for a representative PMUT. Then, acoustic-structure interface of each transducer is mapped onto the fluid domain boundary. In the latter stage, the piezo-acoustic problem is solved by means of a staggered algorithm, considering the PMUTs behavior as a linear combination of few modes. The custom code results, in the case of the stand-alone transducer, have been compared with the commercial software COMSOL multiphysics 5.2 ones, showing a very good agreement. Hence, the model has been applied to the simulation of the pressure wave propagation involving an array of several vibrating PMUTs. Two case studies are reported in which, respectively, the transmission has been focused in a fluid domain neighborhood of the focal point, along the transversal acoustic axis of the device, by means of 11x11 PMUTs array and the RX phase has been simulated for the 7x7 cluster of PMUTs, considering an incoming background pressure field. The numerical model shows very good agreement and faster computational time than the standard coupled piezoelectric-acoustic full-order approaches implemented in several FE commercial codes.

7.1 Introduction

Several applications involve the use of large array of PMUTs to guarantee the proper transmitted acoustic energy, as reported in cap 2; medical acoustic imaging [18,19,48,56,136–143] and hydrophones exploit [144–146] the in-water wave propagation of ultrasonic pulses [11, 13, 14], finger-printing recognition [81,82,147–149] and sonar applications [150–152]. Further applications, in which several transducers, are needed are represented by non-destructive testing [153–159], humidity sensing [160] and velocity sensing (doppler flow meter) [12, 161–166] .

The primary focus of the present chapter is to show the novel reduced order approach for electro-mechanical-acoustic analyses and investigate the corresponding simulation performances. Hence, the attention is paid to the study of beam focusing, wave interference and pressure receiving problems, involving several transducers. The model has been implemented into a Fortran custom code and represents a suitable tool to carry out pressure propagation pattern analyses in which the transducers are driven independently each other. Furthermore, the acoustic interaction among multiple vibrating diaphragms, in the near-field, is taken into account by means of the full order FEM approach for the acoustic problem, in spite of the order reduction of the PMUTs dynamic behaviour. Hence, the interference phenomena during the wave propagation are properly simulated.

The chapter is organized as follows. In the second section, the mathematical formulation for the reduced order transmitting and receiving problems is presented [167–170]. In the third section the involved methodology is described. In the fourth section, results and discussion are reported for the case of a stand-alone transducer compared with the COMSOL Multhiphysics 5.2 ones. Afterward, section 5 and 6 are devoted to the simulations of two different scenarios by means of the custom code, to study the 11x11 PMUTs array transmitting focusing problem and 7x7 cluster of PMUTs in receiving phase. In the end, final remarks are collected in the conclusions section.

7.2 Model order reduction: mathematical formulation

This section is devoted to the Reduced Order Model (ROM) mathematical derivation based on the Model Order Reduction (MOR) technique applied to the piezoelectric problem. After recalling the piezoelectric constitutive law, the weak formulation of the problem and the finite element method approximations are presented together with the current equation. Therefore,

the associated eigenvalue problem is derived with two solution approaches. Consequently, the order reduction technique is enforced to obtain the final equations. In the last part, the coupling with the acoustics is shown with the FEM approximations of the transmitting and the receiving problems.

7.2.1 Piezoelectric constitutive equations

Considering a piezoelectric domain Ω and assuming φ as the electric potential, in standard piezoelectric notation [45] for the stress-charge form [171–173], the piezoelectric constitutive model (3.9) and (3.10), presented in chapter 3, is recalled below

$$\boldsymbol{T} = \mathbf{C} : \boldsymbol{S} - \mathbf{e}^T \cdot \boldsymbol{E} = \mathbf{C} : \boldsymbol{S}[\boldsymbol{u}] + \mathbf{e}^T \cdot \nabla\varphi \tag{7.1}$$

$$\boldsymbol{D} = \mathbf{e} : \boldsymbol{S} + \boldsymbol{\varepsilon} \cdot \boldsymbol{E} = \mathbf{e} : \boldsymbol{S}[\boldsymbol{u}] - \boldsymbol{\varepsilon} \cdot \nabla\varphi \tag{7.2}$$

where $\boldsymbol{S}[\boldsymbol{u}] = \text{sym}(\nabla \boldsymbol{u})$. Furthermore, let $\boldsymbol{g}_j$ be the base vectors of the Cartesian 3D space, if $\mathbf{e} = e_{kij}\boldsymbol{g}_k \otimes \boldsymbol{g}_i \otimes \boldsymbol{g}_j$ then $\mathbf{e}^T$ is defined as the tensor $\mathbf{e}^T = e_{kij}\boldsymbol{g}_j \otimes \boldsymbol{g}_i \otimes \boldsymbol{g}_k$.

7.2.2 Weak formulation of the piezoelectric problem

Under the assumptions of any imposed displacement equal to zero, any imposed potential equal to zero but for on the electrode surface S_E, no body forces and electric charges. Considering the presence of traction forces $\boldsymbol{f}^D$ on the loaded surface S_T.

Therefore, the global weak form of the piezoelectric problem is presented:

$$\int_\Omega \rho\ddot{\boldsymbol{u}} \cdot \tilde{\boldsymbol{u}}\, \mathrm{d}\Omega + \int_\Omega \boldsymbol{T} : \boldsymbol{S}[\tilde{\boldsymbol{u}}]\mathrm{d}\Omega = \int_{\partial\Omega} (\boldsymbol{T} \cdot \boldsymbol{n}_p) \cdot \tilde{\boldsymbol{u}}\, \mathrm{d}S \quad \forall \tilde{\boldsymbol{u}} \in \mathcal{C}_u \tag{7.3}$$

$$\int_\Omega \boldsymbol{D} \cdot \nabla\tilde{\varphi}\, \mathrm{d}\Omega = \int_{\partial\Omega} (\boldsymbol{D} \cdot \boldsymbol{n}_p)\tilde{\varphi}\, \mathrm{d}S \quad \forall \tilde{\varphi} \in \mathcal{C}_\varphi \tag{7.4}$$

Finally, imposing the boundary conditions we get the restricted weak form of the piezoelectric problem:

$$\int_\Omega \rho\ddot{\boldsymbol{u}} \cdot \tilde{\boldsymbol{u}}\, \mathrm{d}\Omega + \int_\Omega \boldsymbol{S}[\tilde{\boldsymbol{u}}] : \left(\mathbf{C} : \boldsymbol{S}[\boldsymbol{u}] + \mathbf{e}^T \cdot \nabla\varphi\right) \mathrm{d}\Omega = \int_{S_T} \boldsymbol{f}^D \cdot \tilde{\boldsymbol{u}}\, \mathrm{d}S$$

$$\forall \tilde{\boldsymbol{u}} \in \mathcal{C}_u(0) \tag{7.5}$$

$$\int_\Omega \nabla\tilde{\varphi} \cdot \left(\mathbf{e} : \boldsymbol{S}[\boldsymbol{u}] - \boldsymbol{\varepsilon} \cdot \nabla\varphi\right) \mathrm{d}\Omega = 0 \quad \forall \tilde{\varphi} \in \mathcal{C}_\varphi(0). \tag{7.6}$$

7.2.3 Finite element modelling of the piezoelectric problem

Hereafter, for sake of brevity, the subscript h to indicate the discrete domain and interpolated unknown fields is neglected. Therefore, assuming a quadratic lagrangian interpolation leads to

$$\boldsymbol{u}(\boldsymbol{x},t) = \sum_{k,j} \mathcal{N}_k(\boldsymbol{x}) \boldsymbol{g}_j u_j^{(k)}(t) \qquad \varphi(\boldsymbol{x},t) = \sum_{k} \mathcal{N}_k(\boldsymbol{x}) \varphi^{(k)}(t) + \varphi_V(\boldsymbol{x}) \Phi(t)$$

where, in the first equation, the sum over k is restricted to nodes where displacements are unknown while in the second one the sum over k is restricted to nodes where potentials are unknown but for the electrode S_{E} nodes where the potential is equal to Φ. The same finite element interpolation is used for the virtual fields $\tilde{\boldsymbol{u}}$ and $\tilde{\varphi}$. Moreover the function φ_V is defined in the FEM sense as:

$$\varphi_V(\boldsymbol{x}) = \sum_{m} \mathcal{N}_m(\boldsymbol{x})$$

where the sum over m is restricted to nodes of the electrode S_{E} where $\varphi_V(\boldsymbol{x}^{(m)}) = 1$ and the . The discrete form of the piezoelectric weak problem is presented below.

$$\begin{bmatrix} \mathbb{M} & 0 \\ 0 & 0 \end{bmatrix} \begin{Bmatrix} \ddot{\mathbb{U}} \\ \ddot{\mathbb{V}} \end{Bmatrix} + \begin{bmatrix} \mathbb{K}^{uu} & \mathbb{K}^{uv} \\ -\mathbb{K}^{vu} & -\mathbb{K}^{vv} \end{bmatrix} \begin{Bmatrix} \mathbb{U} \\ \mathbb{V} \end{Bmatrix} = \begin{Bmatrix} \mathbb{F}^{ut} \\ 0 \end{Bmatrix} + \begin{Bmatrix} \mathbb{F}^{u\phi} \\ \mathbb{F}^{v\phi} \end{Bmatrix} \Phi \tag{7.7}$$

With $[\mathbb{K}^{vu}] = [\mathbb{K}^{uv}]^T$. In the piezoelectric code $\mathbb{U}_I = u_j^{(k)}$ if I corresponds to the dof associated with the node k in direction j and $\mathbb{V}_J = \varphi(k)$ if J corresponds to the potential dof associated with the node k. Array $\mathbb{V}$ contains values of the potential on all the nodes but for the electrode where it is equal to Φ. Finally, the involved matrices are computed as follows.

$$\mathbb{M}_{IJ} = \int_\Omega \rho \mathcal{N}_k \boldsymbol{g}_j \cdot \mathcal{N}_n \boldsymbol{g}_m \,\mathrm{d}\Omega \tag{7.8}$$

$$\mathbb{K}^{uu}_{IJ} = \int_\Omega \boldsymbol{S}[\mathcal{N}_k \boldsymbol{g}_j] : \mathbf{C} : \boldsymbol{S}[\mathcal{N}_n \boldsymbol{g}_m] \,\mathrm{d}\Omega \tag{7.9}$$

$$\mathbb{K}^{uv}_{IJ} = \int_\Omega \boldsymbol{S}[\mathcal{N}_k \boldsymbol{g}_j] : \mathbf{e}^T \cdot \nabla[\mathcal{N}_n] \,\mathrm{d}\Omega \tag{7.10}$$

$$\mathbb{K}^{vv}_{IJ} = \int_\Omega \nabla[\mathcal{N}_k] \cdot \boldsymbol{\varepsilon} \cdot \nabla[\mathcal{N}_n] \,\mathrm{d}\Omega \tag{7.11}$$

$$\mathbb{F}^{ut}_{I} = \int_{S_T} (\mathcal{N}_k \boldsymbol{g}_j) \cdot \boldsymbol{f}^D \,\mathrm{d}S \tag{7.12}$$

$$\mathbb{F}^{u\phi}_{I} = -\int_\Omega \boldsymbol{S}[\mathcal{N}_k \boldsymbol{g}_j] : \mathbf{e}^T \cdot \nabla \varphi_V \,\mathrm{d}\Omega \tag{7.13}$$

$$\mathbb{F}^{v\phi}_{I} = -\int_\Omega \nabla[\mathcal{N}_k] \cdot \boldsymbol{\varepsilon} \cdot \nabla \varphi_V \,\mathrm{d}\Omega \tag{7.14}$$

7.2.4 Current equation

Let $\boldsymbol{n}_p$ denote the outward normal on the electrode surface S_E of the piezoelectric domain Ω then the current is

$$I = -\int_{S_\mathrm{E}} \dot{\boldsymbol{D}} \cdot \boldsymbol{n}_p \,\mathrm{d}S$$

with

$$\dot{\boldsymbol{D}} = \mathbf{e} : \boldsymbol{S}[\dot{\boldsymbol{u}}] - \boldsymbol{\varepsilon} \cdot \nabla \dot{\varphi}$$

Now, taking the global weak form for the electrical equation (7.4) and choosing $\tilde{\varphi} = \varphi_V$ implies

$$\begin{aligned} I = -\int_{S_\mathrm{E}} \dot{\boldsymbol{D}} \cdot \boldsymbol{n}_p \,\mathrm{d}S = -\int_\Omega \dot{\boldsymbol{D}} \cdot \nabla \varphi_V \,\mathrm{d}\Omega = \\ = -\int_\Omega (\mathbf{e} : \boldsymbol{S}[\dot{\boldsymbol{u}}] - \boldsymbol{\varepsilon} \cdot \nabla \dot{\varphi}) \cdot \nabla \varphi_V \,\mathrm{d}\Omega \end{aligned} \tag{7.15}$$

$$I = \{\mathbb{F}^{uv}\}^T \{\dot{\mathbb{U}}\} - \{\mathbb{F}^{v\phi}\}^T \{\dot{\mathbb{V}}\} + C_{vv} \dot{\Phi} \tag{7.16}$$

which is the current equation of the problem, with the electric capacitance.

$$C_{vv} = \int_\Omega \nabla \varphi_V \cdot \boldsymbol{\varepsilon} \cdot \nabla \varphi_V \,\mathrm{d}\Omega.$$

7.2.5 Model order reduction for the piezoelectric problem: approach 1

To generate the ROM, the eigenvalue piezoelectric problem is solved [174, 175]. Hereinafter, the decoupled approach is described starting from the elastodynamics.

Eigenvalue problem

Solving the elastodynamics problem with no forcing term (free vibrations problem) implies

$$-\omega^2[\mathbb{M}]\{\mathbb{U}\} + [\mathbb{K}^{uu}]\{\mathbb{U}\} = \{0\} \tag{7.17}$$

leads to the corresponding mechanical eigenvalues and eigenvectors.

Let $\{\mathbb{U}\}^m$ be the array of nodal values of the mechanical modes and $\boldsymbol{U}^m(\boldsymbol{x})$ the corresponding interpolated fields. The displacement field is obtained as

$$\boldsymbol{u}(\boldsymbol{x}, t) = \sum_m q_m(t)\boldsymbol{U}^m(\boldsymbol{x}).$$

Reduced order model generation

Setting

$$\{\mathbb{U}(t)\} = \sum_m q_m(t)\{\mathbb{U}^m\}$$

the second equation of (7.7) becomes

$$[\mathbb{K}^{vv}]\{\mathbb{V}\} = [\mathbb{K}^{vu}]\sum_m q_m\{\mathbb{U}^m\} + \{\mathbb{F}^{v\phi}\}\Phi = \sum_m q_m\{\mathbb{F}^{vq_m}\} + \{\mathbb{F}^{v\phi}\}\Phi \tag{7.18}$$

where

$$\{\mathbb{F}^{vq_m}\} = [\mathbb{K}^{vu}]\{\mathbb{U}^m\}$$

that implies

$$\{\mathbb{V}\} = \sum_m q_m\{\mathbb{V}^{q_m}\} + \{\mathbb{V}^{\phi}\}\Phi \tag{7.19}$$

with the following equalities

$$\{\mathbb{V}^{q_m}\} = [\mathbb{K}^{vv}]^{-1}\{\mathbb{F}^{vq_m}\} \qquad \{\mathbb{V}^{\phi}\} = [\mathbb{K}^{vv}]^{-1}\{\mathbb{F}^{v\phi}\}.$$

in which $\{\mathbb{V}^{\phi}\}$ is the static solution of the electric problem assuming a unit potential Φ.

Therefore, plugging the results in the first equation of (7.7) projected on $\{\mathbb{U}^m\}$, gives one the following dynamic equations of motion in the unknown modal parameter q_m

$$\ddot{q_m} + (\omega_m^2 + \{\mathbb{F}^{vq_m}\}^T\{\mathbb{V}^{q_m}\})q_m = \{\mathbb{U}^m\}^T\{\mathbb{F}^{ut}\} + (\{\mathbb{U}^m\}^T\{\mathbb{F}^{u\phi}\} - \{\mathbb{F}^{vq_m}\}^T\{\mathbb{V}^{\phi}\})\Phi$$

or

$$\ddot{q_m} + \bar{\omega}_m^2 q_m = f_m + \eta_m \Phi \tag{7.20}$$

where we have set

$$\bar{\omega}_m = \omega_m^2 + \{\mathbb{F}^{vq_m}\}^T\{\mathbb{V}^{q_m}\} \quad f_m = \{\mathbb{U}^m\}^T\{\mathbb{F}^{ut}\}$$
$$\eta_m = \{\mathbb{U}^m\}^T\{\mathbb{F}^{u\phi}\} - \{\mathbb{F}^{vq_m}\}^T\{\mathbb{V}^{\phi}\}. \tag{7.21}$$

in which $\bar{\omega}_m$ is the estimated electro-mechanical circular eigenfrequecy of the m-th mode, f_m is the mechanical r.h.s. projection on mode $\{\mathbb{U}^m\}$ and η_m the electro-mechanical influence coefficient of mode m.

Moreover, considering the following equalities

$$\{\dot{\mathbb{U}}\} = \sum_m \dot{q}_m\{\mathbb{U}^{q_m}\} \qquad \{\dot{\mathbb{V}}\} = \sum_m \dot{q}_m\{\mathbb{V}^{q_m}\} + \{\mathbb{V}^{\phi}\}\dot{\Phi} \tag{7.22}$$

from (7.16) we get the ROM for the current

$$I = \sum_m (\{\mathbb{F}^{u\phi}\}^T\{\mathbb{U}^m\} - \{\mathbb{F}^{v\phi}\}^T\{\mathbb{V}^{q_m}\})\dot{q}_m + (C_{vv} - \{\mathbb{F}^{v\phi}\}^T\{\mathbb{V}^{\phi}\})\dot{\Phi}$$

or

$$I = \sum_m \dot{q}_m\eta_m + C_0\dot{\Phi} \tag{7.23}$$

where we have set the piezoelectric capacitance equal to

$$C_0 = C_{vv} - \{\mathbb{F}^{v\phi}\}^T\{\mathbb{V}^{\phi}\}.$$

7.2.6 Model order reduction for the piezoelectric problem: approach 2

After the decoupled approach, the fully coupled approach is described [176]. It depends on the availability of a suitable eigenvalue solver. By static condensation of $\{\mathbb{V}\}$, the system (7.7) becomes

$$[\mathbb{M}]\{\ddot{\mathbb{U}}\} + [\mathbb{K}]\{\mathbb{U}\} = \{\mathbb{F}^{ut}\} + (\{\mathbb{F}^{u\phi}\} - [\mathbb{K}^{uv}]\{\mathbb{V}^{\phi}\})\Phi \tag{7.24}$$
$$\{\mathbb{V}\} = [\mathbb{K}^{vv}]^{-1}[\mathbb{K}^{vu}]\{\mathbb{U}\} + \{\mathbb{V}^{\phi}\}\Phi \tag{7.25}$$

where

$$[\mathbb{K}] = [\mathbb{K}^{uu}] + [\mathbb{K}^{uv}][\mathbb{K}^{vv}]^{-1}[\mathbb{K}^{vu}] \qquad \{\mathbb{V}^{\phi}\} = [\mathbb{K}^{vv}]^{-1}(\{\mathbb{F}^{v\phi}\}$$

Eigenvalue problem

Solving (7.24), (7.25) with no forcing term (piezoelectric free vibrations problem) implies

$$[\mathbb{M}]\{\ddot{\mathbb{U}}\} + [\mathbb{K}]\{\mathbb{U}\} = \{0\} \tag{7.26}$$

$$\{\mathbb{V}\} = [\mathbb{K}^{vv}]^{-1}[\mathbb{K}^{vu}]\{\mathbb{U}\} \tag{7.27}$$

Let $\{\mathbb{U}^m\}$ be the array of nodal values of the piezoelectric displacement modes, $\{\mathbb{V}^m\}$ the associated array of nodal values through (7.27), $\boldsymbol{U}^m(\boldsymbol{x})$ and $V^m(\boldsymbol{x})$ the corresponding interpolated fields.

$[\mathbb{K}^{uu}]$ and $[\mathbb{K}^{vv}]$ are positive definite ($[\mathbb{K}]$ positive definite) because of the provided displacement and electric potential constraints .

The mass matrix $[\mathbb{M}]$ being symmetric positive definite, the eigenvalue problem is well posed and yields a simultaneous diagonalization of the matrices $[\mathbb{M}]$ and $[\mathbb{K}]$, with $\omega_m^2 > 0 \quad \forall m$.

$\{\mathbb{U}^m\}$ are chosen to fulfill the conditions:

$$\{\mathbb{U}^m\}^T[\mathbb{M}]\{\mathbb{U}^m\} = 1 \quad \Rightarrow \quad \{\mathbb{U}^m\}^T[\mathbb{K}]\{\mathbb{U}^m\} = \omega_m^2 \quad \forall m$$

$$\{\mathbb{U}^n\}^T[\mathbb{M}]\{\mathbb{U}^m\} = 0, \qquad \{\mathbb{U}^n\}^T[\mathbb{K}]\{\mathbb{U}^m\} = 0 \qquad (\forall n \neq m)$$

Reduced order model generation

Selecting a limited number m of modes (possibly one) the displacement field is obtained as the combination of the piezoelectric modes

$$\boldsymbol{u}(\boldsymbol{x}, t) = \sum_m q_m(t)\boldsymbol{U}^m(\boldsymbol{x})$$

and the corresponding array of unknown nodal values:

$$\{\mathbb{U}(t)\} = \sum_m q_m(t)\{\mathbb{U}^m\}$$

which also gives one the expression of nodal potentials through (7.25)

$$\{\mathbb{V}(t)\} = \sum_m q_m(t)\{\mathbb{V}^m\} + \{\mathbb{V}^{\phi}\}\Phi$$

Hence, projecting (7.24) on $\{\mathbb{U}^m\}$ implies

$$\begin{aligned} \ddot{q_m} + \omega_m^2 q_m &= \{\mathbb{U}^m\}^T\{\mathbb{F}^{ut}\} + \{\mathbb{U}^m\}^T(\{\mathbb{F}^{u\phi}\} - \{\mathbb{K}^{uv}\}^T\{\mathbb{V}^{\phi}\})\Phi \\ &= \{\mathbb{U}^m\}^T\{\mathbb{F}^{ut}\} + (\{\mathbb{U}^m\}^T\{\mathbb{F}^{u\phi}\} - \{\mathbb{V}^m\}^T\{\mathbb{F}^{v\phi}\})\Phi \\ &= f_m + \eta_m\Phi \end{aligned} \tag{7.28}$$

where we have set

$$f_m = \{\mathbb{U}^m\}^T\{\mathbb{F}^{ut}\} \qquad \eta_m = \{\mathbb{U}^m\}^T\{\mathbb{F}^{u\phi}\} - \{\mathbb{V}^m\}^T\{\mathbb{F}^{v\phi}\} \tag{7.29}$$

which have the same meaning of the equivalent quantities in the approach 1 (7.21).

Moreover, the following equalities hold

$$\{\dot{\mathbb{U}}\} = \sum_m \dot{q}_m\{\mathbb{U}^m\} \qquad \{\dot{\mathbb{V}}\} = \sum_m \dot{q}_m\{\mathbb{V}^m\} + \{\mathbb{V}^{\phi}\}\dot{\Phi}$$

Therefore, plugging them into (7.16), the ROM for the current is obtained

$$I = \sum_m (\{\mathbb{F}^{u\phi}\}^T\{\mathbb{U}^m\} - \{\mathbb{F}^{v\phi}\}^T\{\mathbb{V}^m\})\dot{q}_m + (C_{vv} - \{\mathbb{F}^{v\phi}\}^T\{\mathbb{V}^{\phi}\})\dot{\Phi}$$

or

$$I = \sum_m \dot{q}_m\eta_m + C_0\dot{\Phi} \tag{7.30}$$

where we have defined the piezoelectric capacitance

$$C_0 = C_{vv} - \{\mathbb{F}^{v\phi}\}^T\{\mathbb{V}^{\phi}\}.$$

7.2.7 Equivalent electric circuit with one mode

Considering a piezoelectric structure vibrating under the voltage excitation, no mechanical loading and only one mode selected, with eigenfreq ω (7.28) becomes (referring to (7.20), $\omega \leftarrow \bar{\omega}$)

$$\ddot{q} + \frac{\omega}{Q}\dot{q} + \omega^2 q = \eta\Phi \tag{7.31}$$

where a dissipation linear term has been added, with damping ratio $1/2Q$ where Q is the enforced quality factor, while the current equation becomes

$$I = I_{mech} + I_C = \eta\dot{q} + C_0\dot{\Phi} \tag{7.32}$$

Thus, it can be represented as an electrical circuit given by the parallel of a capacitor C_0, associated with the piezoelectric material at the rest configuration subjected to a voltage difference Φ, in which the current $I_C = C_0\dot{\Phi}$

flows and the series of a mechanical resistance, capacitor and inductor defined as follows,

$$L_{mech} = \frac{1}{\eta^2} \qquad R_{mech} = \frac{\omega}{Q\eta^2} \qquad C_{mech} = \frac{\eta^2}{\omega^2} \tag{7.33}$$

where the current $I_{mech} = \eta\dot{q}$ flows.

Hence, two cases are possible: open circuit in which the total current $I = I_{mech} + I_C = 0$ and closed circuit where the current I is feeding an electrical load R and the equality $I = \Phi/R$ holds.

7.2.8 Coupling with acoustics

In this section, the coupling with the acoustics and the transmitting (TX) and receiving (RX) problems are described. Considering a lossless fluid domain Ω [29, 31, 32, 170, 177], PMUTs are placed on a flat boundary in a baffled configuration, which imply a hard wall condition (3.25) is enforced on the remaining part of the boundary encompassing the transducers [29]. Furthermore, assuming the normal $\boldsymbol{n}$ going outward and always referred to the fluid domain, in order to simulate the infinite radiation, a first order absorbing boundary condition (ABC) is imposed on the remaining acoustic boundary (3.26) (see a detailed picture in Fig. 7.3).

Transmitting problem

Setting $\boldsymbol{u} = \sum_m q_m \boldsymbol{U}^m$ and $\tilde{\boldsymbol{u}} = \boldsymbol{U}^m$ in (7.5) or equivalently recalling (7.28) and the acoustic-structure interaction (ASI) condition (3.24), we get the modal projection for the i-th PMUT with interaction surface $S_{\mathrm{P_i}}$ where the pressure is applied (referring to approach 1, $\omega \leftarrow \bar{\omega}$)

$$\ddot{q}_m^{(i)} + {\omega_m^{(i)}}^2 q_m^{(i)} = \int_{S_{\mathrm{P_i}}} p\boldsymbol{n} \cdot \boldsymbol{U}^{(i),m} \,\mathrm{d}S + \eta_m^{(i)} \Phi^{(i)} \tag{7.34}$$

where p represents the unknown acoustic pressure and the $\omega_m^{(i)}$ is the m-th circular eigenfrequency of the i-th PMUT.

Weak form of the transmitting reduced coupled problem

Hereinafter, the weak form of the TX reduced coupled problem is presented, where, $c = \sqrt{\kappa/\rho}$ is the speed of sound, κ the isentropic bulk modulus of the fluid and ρ the density of the fluid, computed at the reference state (3.2.1), presented in 3.

Therefore, considering the i-th PMUT with interaction surface $S_{\mathrm{P_i}}$, the m-th eigenmode and the ASI condition (3.23), the weak form of the acoustics TX problem is obtained as follows

$$\int_\Omega (\rho\ddot{p}\,\tilde{p} + \kappa\nabla p\cdot\nabla\tilde{p})\,\mathrm{d}\Omega = \int_{\partial\Omega}\kappa(\nabla p\cdot\boldsymbol{n})\tilde{p}\,\mathrm{d}S = \tag{7.35}$$

$$= -\int_{S_{\mathrm{ABC}}}\frac{\kappa}{c}\dot{p}\tilde{p}\,\mathrm{d}S - \sum_i\int_{S_{\mathrm{P_i}}}\rho\kappa(\ddot{\boldsymbol{u}}\cdot\boldsymbol{n})\tilde{p}\,\mathrm{d}S$$

$$= -\int_{S_{\mathrm{ABC}}}\frac{\kappa}{c}\dot{p}\tilde{p}\,\mathrm{d}S - \sum_i\sum_m\ddot{q}_m^{(i)}\int_{S_{\mathrm{P_i}}}\rho\kappa(\boldsymbol{U}^{(i),m}\cdot\boldsymbol{n})\tilde{p}\,\mathrm{d}S \quad \forall\tilde{p}\in\mathcal{C}_p.$$

FE modelling of the transmitting problem

Assuming a quadratic lagrangian interpolation of the unknown pressure field

$$p(\boldsymbol{x},t) = \sum_r \mathcal{N}_k(\boldsymbol{x})p^{(r)}(t) \tag{7.36}$$

where the sum over r is restricted to nodes where the pressure is unknown, lead to the discretized acoustic RO coupled system. Therefore, considering the i-th PMUT with interaction surface $S_{\mathrm{P_i}}$ and the m-th eigenmode the TX problem is obtained as follows

$$\left[\mathbb{M}\right]\left\{\ddot{\mathbb{P}}\right\} + \left[\mathbb{C}\right]\left\{\dot{\mathbb{P}}\right\} + \left[\mathbb{K}\right]\left\{\mathbb{P}\right\} = -\left\{\mathbb{F}^{p\ddot{q}}\right\} \tag{7.37}$$

$$\ddot{q}_m^{(i)} + {\omega_m^{(i)}}^2 q_m^{(i)} = f_m^{(i),qp} + \eta_m^{(i)}\Phi^{(i)}. \tag{7.38}$$

In the acoustics code $\mathbb{P}_I = p^{(r)}$ if I corresponds to the dof associated with the node r and $\mathbb{U}_J^{(i),m} = u_3^{(s)(i),m}$ if J corresponds to the dof associated with the node s.

$$\mathbb{M}_{IJ} = \int_\Omega \rho\mathcal{N}_r\mathcal{N}_n\,\mathrm{d}\Omega \tag{7.39}$$

$$\mathbb{C}_{IJ} = \int_\Omega \frac{\kappa}{c}\mathcal{N}_r\mathcal{N}_n\,\mathrm{d}\Omega \tag{7.40}$$

$$\mathbb{K}_{IJ} = \int_\Omega \kappa\nabla[\mathcal{N}_r]\cdot\nabla[\mathcal{N}_n]\,\mathrm{d}\Omega \tag{7.41}$$

$$\mathbb{F}_I^{p\ddot{q}} = \sum_i\sum_m\sum_s \ddot{q}_m^{(i)}u_3^{(s)(i),m}\int_{S_{\mathrm{P_i}}}\rho\kappa\mathcal{N}_r\mathcal{N}_s\boldsymbol{g}_3\cdot\boldsymbol{n}\,\mathrm{d}S \tag{7.42}$$

$$f_m^{(i),qp} = \sum_r\sum_s p^{(r)}u_3^{(s)(i),m}\int_{S_{\mathrm{P_i}}}\mathcal{N}_r\mathcal{N}_s\boldsymbol{g}_3\cdot\boldsymbol{n}\,\mathrm{d}S \tag{7.43}$$

Receiving problem

Setting $\boldsymbol{u} = \sum_m q_m \boldsymbol{U}^m$ and considering an imposed incident background pressure field p_{in} in Ω, implies a total pressure field equal to

$$p_{tot} = p_{in} + p$$

where p represents the unknown scattered pressure.

Therefore, the modal projection (7.28) for the i-th PMUT with interaction surface $S_{\mathrm{P_i}}$ leads to (referring to approach 1, $\omega \leftarrow \bar{\omega}$)

$$\begin{aligned} \ddot{q}_m^{(i)} + {\omega_m^{(i)}}^2 q_m^{(i)} &= \int_{S_{\mathrm{P_i}}} p_{tot} \boldsymbol{n} \cdot \boldsymbol{U}^{(i),m} \,\mathrm{d}S + \eta_m^{(i)} \Phi^{(i)} \\ &= \int_{S_{\mathrm{P_i}}} p \boldsymbol{n} \cdot \boldsymbol{U}^{(i),m} \,\mathrm{d}S + \int_{S_{\mathrm{P_i}}} p_{in} \boldsymbol{n} \cdot \boldsymbol{U}^{(i),m} \,\mathrm{d}S + \eta_m^{(i)} \Phi^{(i)} \end{aligned} \tag{7.44}$$

While the in the current equation, considering the open circuit configuration, we have

$$C_0^{(i)} \dot{\Phi}^{(i)} + \sum_m \dot{q}_m^{(i)} \eta_m^{(i)} = 0 \tag{7.45}$$

Weak form of the receiving reduced coupled problem

Hereinafter, considering the i-th PMUT with interaction surface $S_{\mathrm{P_i}}$ and the m-th eigenmode and the weak form of the RX reduced coupled problem is derived as follows

$$\begin{aligned} &\int_\Omega (\rho \ddot{p}\, \tilde{p} + \kappa \nabla p \cdot \nabla \tilde{p}) \,\mathrm{d}\Omega = \int_{\partial\Omega} \kappa (\nabla p \cdot \boldsymbol{n}) \tilde{p} \,\mathrm{d}S = \\ &= -\int_{S_{\mathrm{ABC}}} \frac{\kappa}{c} \dot{p} \tilde{p} \,\mathrm{d}S - \sum_i \int_{S_{\mathrm{P_i}}} \rho\kappa (\ddot{\boldsymbol{u}} \cdot \boldsymbol{n}) \tilde{p} \,\mathrm{d}S \\ &\quad - \sum_i \int_{S_{\mathrm{P_i}}} \kappa (\nabla p_{in} \cdot \boldsymbol{n}) \tilde{p} \,\mathrm{d}S - \int_{S_{\mathrm{HW}}} \kappa (\nabla p_{in} \cdot \boldsymbol{n}) \tilde{p} \,\mathrm{d}S \\ &= -\int_{S_{\mathrm{ABC}}} \frac{\kappa}{c} \dot{p} \tilde{p} \,\mathrm{d}S - \sum_i \sum_m \ddot{q}_m^{(i)} \int_{S_{\mathrm{P_i}}} \rho\kappa (\boldsymbol{U}^{(i),m} \cdot \boldsymbol{n}) \tilde{p} \,\mathrm{d}S \\ &\quad - \sum_i \int_{S_{\mathrm{P_i}}} \kappa (\nabla p_{in} \cdot \boldsymbol{n}) \tilde{p} \,\mathrm{d}S - \int_{S_{\mathrm{HW}}} \kappa (\nabla p_{in} \cdot \boldsymbol{n}) \tilde{p} \,\mathrm{d}S \qquad \forall \tilde{p} \in \mathcal{C}_p. \end{aligned} \tag{7.46}$$

FE modelling of the receiving problem

We recall the FE interpolation of the unknown acoustic pressure p used for the TX problem 7.36.

Hence, the discretized acoustic system, the ROM for the i-th PMUT, m-th eigenmode and the current equation are obtained as follows

$$\left[\mathbb{M}\right]\left\{\ddot{\mathbb{P}}\right\}+\left[\mathbb{C}\right]\left\{\dot{\mathbb{P}}\right\}+\left[\mathbb{K}\right]\left\{\mathbb{P}\right\}=-\left\{\mathbb{F}^{p\ddot{q}}\right\}-\left\{\mathbb{F}^{pp_{in}^{SP}}\right\}-\left\{\mathbb{F}^{pp_{in}^{HW}}\right\} \quad (7.47)$$

$$\ddot{q}_m^{(i)}+{\omega_m^{(i)}}^2 q_m^{(i)}=f_m^{(i),qp}+f_m^{(i),qp_{in}}+\eta_m^{(i)}\Phi^{(i)} \quad (7.48)$$

$$C_0^{(i)}\dot{\Phi}^{(i)}+\sum_m \dot{q}_m^{(i)}\eta_m^{(i)}=0 \quad (7.49)$$

where we have set the r.h.s terms equal to

$$\mathbb{F}_I^{pp_{in}^{SP}}=\sum_i \int_{S_{\mathrm{P_i}}} \kappa(\nabla p_{in}\cdot\boldsymbol{n})\mathcal{N}_r \,\mathrm{d}S \quad (7.50)$$

$$\mathbb{F}_I^{pp_{in}^{HW}}=\int_{S_{\mathrm{HW}}} \kappa(\nabla p_{in}\cdot\boldsymbol{n})\mathcal{N}_r \,\mathrm{d}S \quad (7.51)$$

$$f_m^{(i),qp_{in}}=\sum_s u_3^{(s)(i),m}\int_{S_{\mathrm{P_i}}} p_{in}\mathcal{N}_s\boldsymbol{g}_3\cdot\boldsymbol{n}\,\mathrm{d}S. \quad (7.52)$$

7.3 Methodology

In this section the methodology adopted in the previous described multiphysics ROM of the electro-mechanical-acoustic problem [178–181] is presented.

The generic piezoelectric transducer consists of a circular clamped plate with a radius of 115 μm and an overall thickness of 19.4 μm, so that the diameter over thickness aspect ratio is 28.75. It consists of several layers with different elastic properties and thicknesses. The structural layer is made of silicon, while the considered piezoelectric layer is made of PZT. It has thickness equal to 2 μm and is in a circular hat configuration with radius of 80.5 μm, coaxial with the plate (see a detail of the layered cross section in Figs. 7.1 and 7.2).

As already described, the problem involves three physics and their mutual interactions that characterize the following COMSOL comparison models: elastodynamics, electrostatics and pressure acoustics. Furthermore, each transducer layer is considered as a linear elastic solid material, while

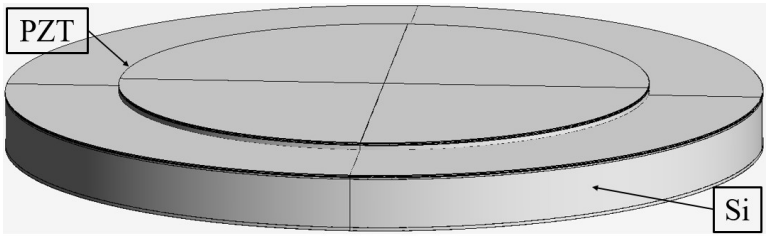

Figure 7.1: *PMUT layered configuration*

for the PZT a linear piezoelectric stress-charge constitutive model is adopted. Hence, a lossless fluid model is enforced in the acoustic domain, to simulate the in-water pressure propagation. The mesh of the acoustic and piezoelectric problem are kept independent. Therefore, the presented PMUT is discretized with quadratic serendipity wedge elements (see a detail in Fig. 7.3) while quadratic tetrahedral elements are used in the fluid domain.

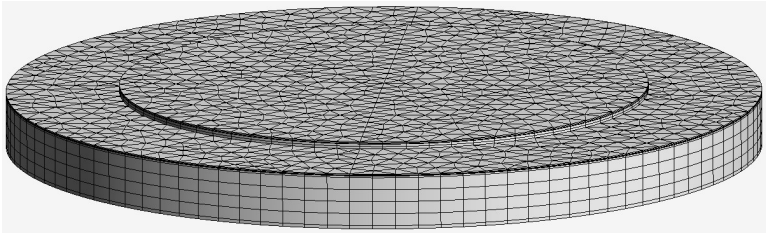

Figure 7.2: *PMUT discretization*

The the waves infinite radiation is guaranteed by the ABC at the acoustic boundaries. Additionally, the array of transducers belongs to a perfectly rigid flat surface. In Fig. 7.3, an example of discretized system, for the TX problem, is presented.

The solution strategy based on the mathematical formulation, described in the previous section, consists of two stages. In the former one, the eigenvalue piezoelectric problem is solved once for all, considering the complete stack of a representative PMUT, by means of the Arnoldi method and few selected modes are extracted. Then, the acoustic-structure interaction surface of each transducer is mapped onto the fluid boundary PMUTs sites by means of a quadratic map, keeping the two meshes independent. Conversely, on the remaining part of the flat boundary an hard wall condition is enforced. In the latter stage, the in-time domain reduced order FE piezoacoustic problem is solved through a staggered implicit procedure based on the Newmark's integration scheme. Therefore, the electro-mechanical

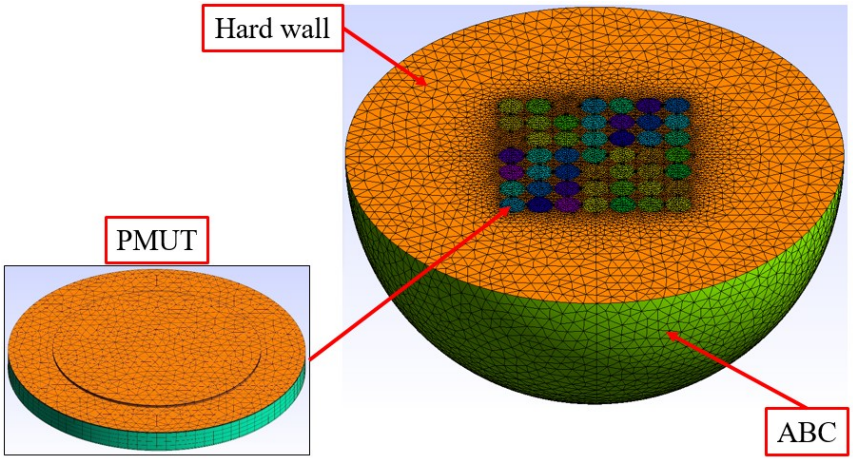

Figure 7.3: *Finite element model in TX phase: PMUT mesh detail (left), fluid domain mesh detail with 7x7 mapped PMUT interaction surfaces in different colors (right).*

dynamic behaviour is represented as a combination of the selected modes, reducing each transducer to few DOFs, while for the full order acoustic problem the solution is computed by means of the finite element method. The described technique allows one to simulate in an exact manner the acoustic-structure interaction as the transducers are vibrating according to the considered modes. The involved computational burden is basically only related to the pressure DOFs and depends on the size of the fluid domain in which the the propagation wave pattern is simulated without any order reduction [182–184] in contrast with the classical vibroacoustics FE-ROMs [185–187] and the commonly used BEM approaches. [188–192].

7.4 Reduced order model custom code vs full order COMSOL 5.2 model

In this section the comparison case studies, for the TX and RX problems, with the standard full order approach implemented in the commercial software COMSOL Multiphysics 5.2, are reported to validate the ROM custom code and investigate the model order reduction performances.

7.4.1 Piezoelectric eigenmodes

In the former stage the piezoelectric eigenproblem is solved to carry out the selected modes involved in the MOR technique. The numerical comparison between the commercial software and the custom piezoelectric code results,

obtained by means of the fully coupled approach 7.27, are presented.

The adopted common FE discretization is characterized by the 15 elements in the PMUT radius, 4 elements through the thickness for the PZT and the silicon layers (refer to Fig. 7.2), while the other layers are discretized with an element through the thickness.

Hence, the first threee axysymmetric modes, adopted in the MOR technique for the TX and RX problems described in the next sections are considered in Fig. 7.4.

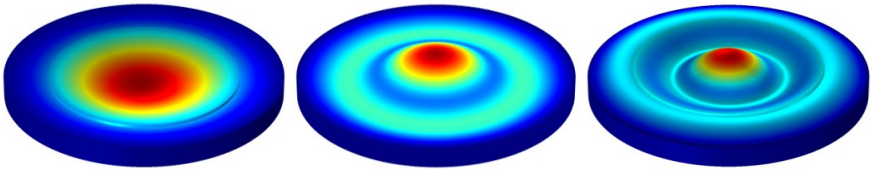

Figure 7.4: *Piezoelectric eigenmodes: (a) fundamental mode; (b) 2nd axysymmetric mode, (c) 3rd axysymmetric mode*

The numerical fundamental electro-mechanical eigenfrequency computed through the custom code is $f_0 = 4.0680$ MHz perfectly matched by the COMSOL direct eigenvalue solver that reports the same value. Conversely, the 2ns axysymmetric eigenfrequency is equal to 15.020 MHz for the custom code and 15.022 MHz for the commercial software. Finally, the 3rd piezoelectric eigenfrequency predicted by the custom code is 30.173 MHz and the COMSOL one is 30.176 MHz. Hence the numerical custom code results show a satisfactory agreement with the commercial software ones and the slight mismatch in the higher modes can be attributed to the small differences in the discretizations and the adopted different numerical procedures.

7.4.2 Stand-alone transducer: transmitting problem

Herinafter, the numerical comparison between the ROM custom code and the COMSOL 5.2 full order model in the transmitting phase, is presented.

The analyzed system consists of a single central vibrating transducer interacting with a hemispherical water domain with radius equal to $3\lambda = 1092.2$ μm where $\lambda = \nu_s/f_0 = 364.06$ μm is the wavelength, $\nu_s = 1481$ μm/μs is the speed of sound in water and $f_0 = 4.068$ MHz is the fundamental electro-mechanical frequency of the PMUT.

The adopted common FE discretization, already sketched in Fig. 7.3, of the fluid acoustic domain, is shown in Fig. 7.5 and it is characterized by

a maximum element size of $\lambda/10 = 36.406$ μm [193–195]. Moreover, a local refinement at the PMUT site has been enforced, to mesh the circular acoustic-structure interface with an element size of $R_{PMUT}/15 = 7.67$ μm where $R_PMUT = 115$ μm is the PMUT radius.

The adopted imposed excitation voltage, at the piezoelectric electrode, is equal to 15 sinusoidal cycles at f_0 with 1 V amplitude.

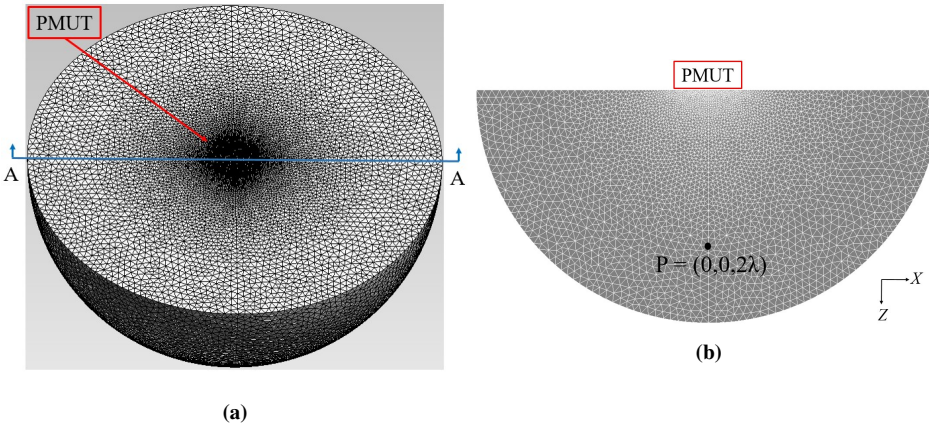

Figure 7.5: *FE fluid domain: (a) 3D view; (b) mesh detail on the cross-section A-A.*

The numerical comparison, considering a ROM generated by the first 3 selected axisymmetric modes (refer to Fig. 7.4), in terms of pressure maps, at three different computation time instants $t = 1.69$, $t = 1.93$ μs and μs $t = 3.69$ μs, on a (O,X,Z) cross-section cut plane A-A (refer to Fig. 7.5) passing through the transducer diameter is presented in Fig. 7.6.

The comparison maps show a very good agreement between the two different solutions approaches. They are both characterized by a spherical propagation starting from the PMUT center, in accordance with the dome-shaped diaphragm vibration. Additionally, the propagation wavelength, shown in the pressure maps, is equal to 364.06 μm that perfectly corresponds to the considered and previously mentioned $\lambda = \nu_s/f_0$.

Furthermore, the corresponding pressure time histories, at the PMUT center and at point P, depicted in Fig. 7.5, placed at $2\lambda = 728.12$ μm on the vertical acoustic axis of the transducer passing through the center of the system are reported in Fig. 7.7.

The FE-ROM predicts the same pressure histories of the COMSOL 5.2 full order model. The PMUT center pressure histories are both characterized by a steady state amplitude of 0.073 MPa after an initial transient regime. The pressure histories at point P=(0,0,2λ) are characterized by

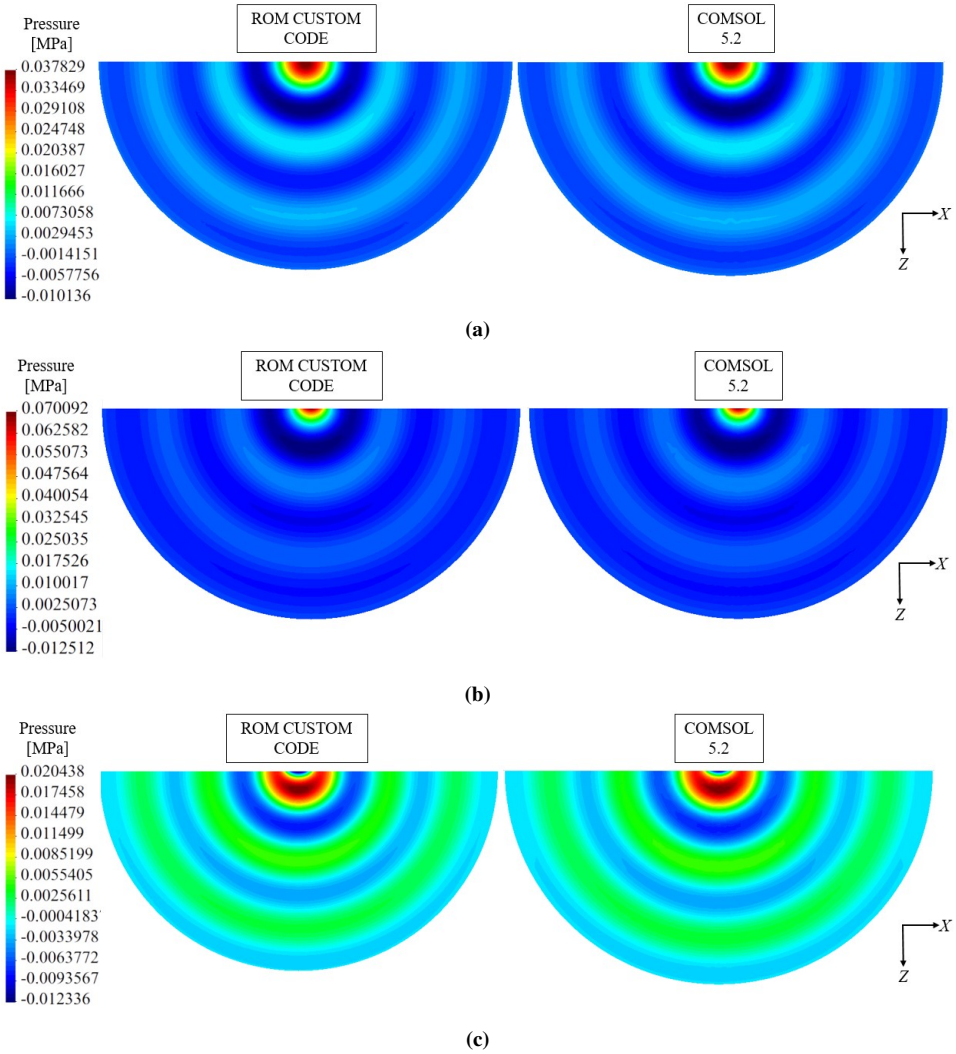

Figure 7.6: *Pressure map comparisons at different time instants: (a) $t = 1.69$ μs; (b) $t = 1.93$ μs; (c) $t = 3.69$ μs.*

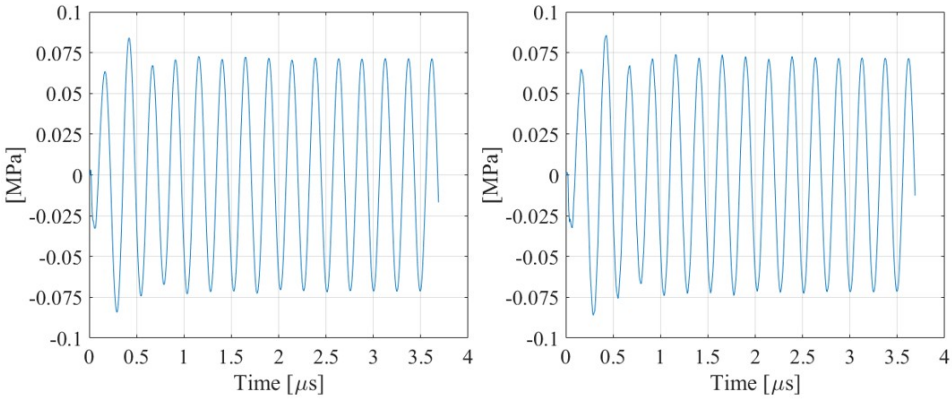

(a) *ROM custom code (left), COMSOL 5.2 (right).*

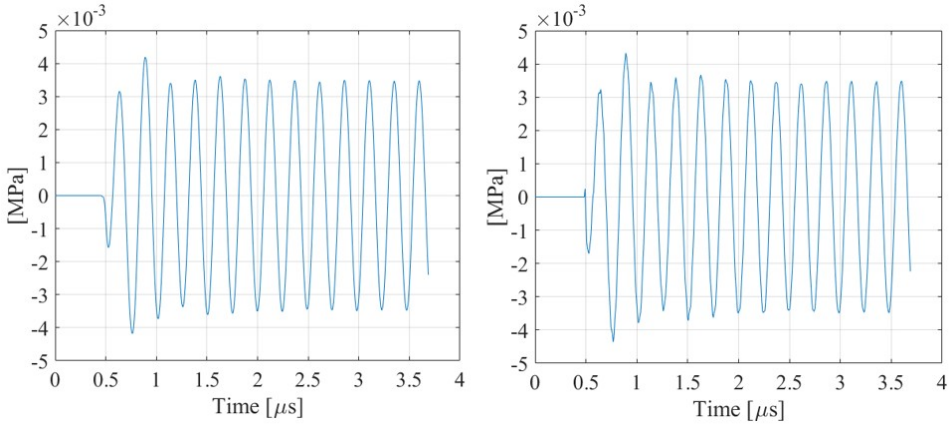

(b) *ROM custom code (left), COMSOL 5.2 (right).*

Figure 7.7: *Pressure time histories at the PMUT center: (a) at PMUT center, (b) at point P=(0,0,2λ).*

0.0035 MPa amplitude, an initial resting time of 0.49 μs corresponding to the time of flight (TOF) of the pressure propagation, travelling for 2λ in a time interval of 2 cycles at the considered f_0. Fig. 7.7 (b) reports a smoother starting oscillation for the custom code case while the standard software is noisier and a first local spike appears.

It is worth noting that, the FE-ROM predicts the same pressure histories and propagation maps of the COMSOL 5.2 full order model. Additionally, the ROM custom code computational time is about 8 mins, conversely, the corresponding involved one in the full-order FEM, is about 1 h 20 mins. To carry out the presented comparison results, the adopted COMSOL 5.2 time integration scheme has been the generalized alpha method with the same time step equal to $\Delta t = 1/(128 f_0)$ of the corresponding Newmark's staggered procedure implemented into the custom code, running on the same machine with 6 Xeon CPU cores @3.6 GHz and 64 GB RAM.

7.4.3 Stand-alone transducer: receiving problem

The numerical comparison between the ROM custom code and the COMSOL 5.2 full order model in the receiving phase, is presented below. The FEM domain is characterized by the same element sizes of the previous TX problem but the transducer is here interacting with a cylindrical acoustic fluid domain with radius and height equal to $3\lambda = 1092.2$ μm (see Fig. 7.8).

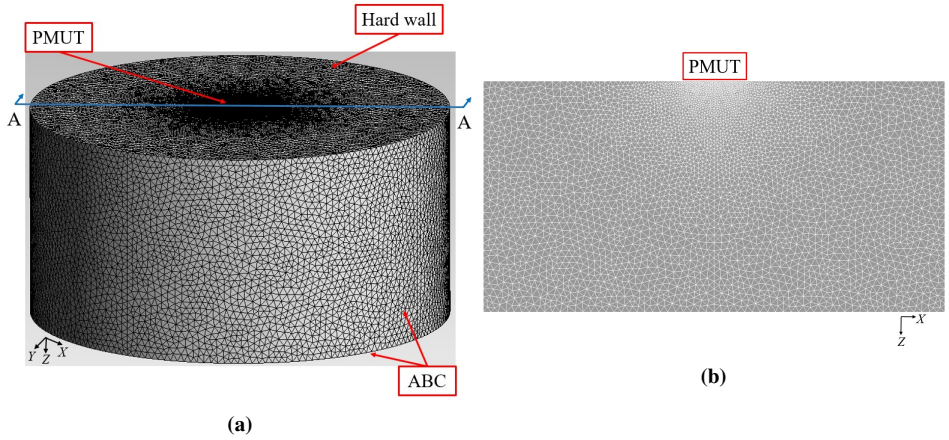

Figure 7.8: *FE fluid domain: (a) 3D view; (b) mesh detail on the cross-section A-A.*

The adopted FEM domain configuration is justified by the reflected pressure propagation pattern generated by the hard wall conditions on the flat

surface and the PMUT vibration. As a matter of fact, the resulting propagation is mainly orthogonal to the the hard wall (O,X,Y) plane, along the vertical direction $\boldsymbol{e}_3$, to be absorbed by the ABC on the opposite boundary. The considered background incoming pressure field is equal to a sinusoidal pressure wave with $P_{in} = 1$ MPa amplitude for 15 cycles at f_0, travelling in direction $-\boldsymbol{e}_3$ in the acoustic domain and it is reported below

$$p_{in}(\boldsymbol{x}, t) = P_{in} \sin(t + \frac{\boldsymbol{x} \cdot \boldsymbol{e}_3}{c}) \qquad t \in [0, 15/f_0] \tag{7.53}$$

In the receiving phase, the attention is focused on the scattered pressure p at the PMUT center and the voltage Φ, on the electrode surface of the piezoelectric layer, generated by the transducer oscillation. Hence, the numerical comparison between the ROM custom code and the COMSOL 5.2 full order model, considering a ROM generated by the first 3 selected axisymmetric modes (refer to Fig. 7.4), in terms of pressure time histories, are reported in Fig. 7.9.

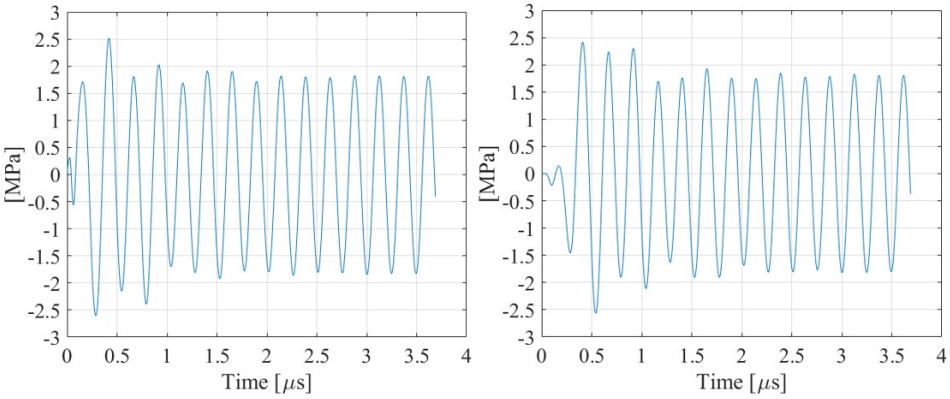

Figure 7.9: *Scattered pressure time histories at the PMUT center: ROM custom code (left), COMSOL 5.2 (right).*

The numerical comparison show a very good agreement between the ROM custom code results and the full order approach implement in COMSOL 5.2. The initial transient behaviour is slightly different in the two cases because of the different adopted integration techniques. In fact in the RX problem, the commercial code applies a unit ramp function to the imposed input pressure in the first time period, to get a smother starting response. Consequently, a smother starting oscillating solution appears in the COMSOL result while the steady state response perfectly matches the custom code one. In fact, the pressure steady state amplitudes are both equal to

1.83 Mpa. Going further, the voltage time history comparison is presented in Fig. 7.10.

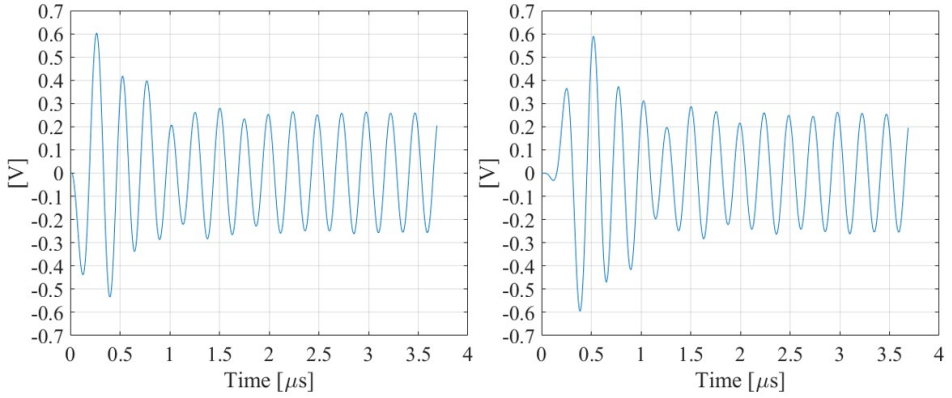

Figure 7.10: *Voltage time histories at the PMUT electrode: ROM custom code (left), COMSOL 5.2 (right).*

The ROM custom code voltage prediction show a satisfactory agreement with the COMSOL one. The previous mentioned COMSOL smoother initial transient behaviour is present in those data, as well. Hence, the steady state response are both characterized by a voltage amplitude equal to 0.27 V.

Finally, the ROM custom predicts the same scattered pressure and voltage histories of the COMSOL 5.2 full order model, in the TX and RX cases. In the presented RX case study the ROM computational time is about 20 mins, with the first 3 axisymmetric modes selected. Conversely, the full-order FEM one, is about 3 h 15 mins, adopting the generalized alpha integration scheme with the same time step equal to $\Delta t = 1/(128 f_0)$ and running on the same machine, as fully described in the previous TX comparison.

7.5 11x11 PMUTs array: transmitting problem

To show the performances of the proposed ROM code, the TX problem is solved focusing the transmission on a point in the acoustic fluid domain by means of a 11x11 array of PMUTs.

The adopted ROM has been generated by the three axysymmetric modes reported in Fig. 7.4. Therefore, the analyzed system consists 121 transducers arranged in a square array with pitch of $2\lambda/3 = 242.69$ μm and interacting with a $6\lambda = 2.184$ mm hemispherical acoustic domain . The FEM domain, already presented in Fig. 7.3, is characterized by an adopted

maximum element size of $\lambda/10$ where λ is the corresponding wavelength at the fundamental electro-mechanical frequency of the PMUT $f_0 = 4.068$ MHz (see a detailed picture in Fig. 7.11). Moreover, a local refinement at the PMUTs sites has been enforced, to mesh the circular acoustic-structure interfaces with an element size of $R_{PMUT}/6 = 19.167$ μm. Hence, a beam

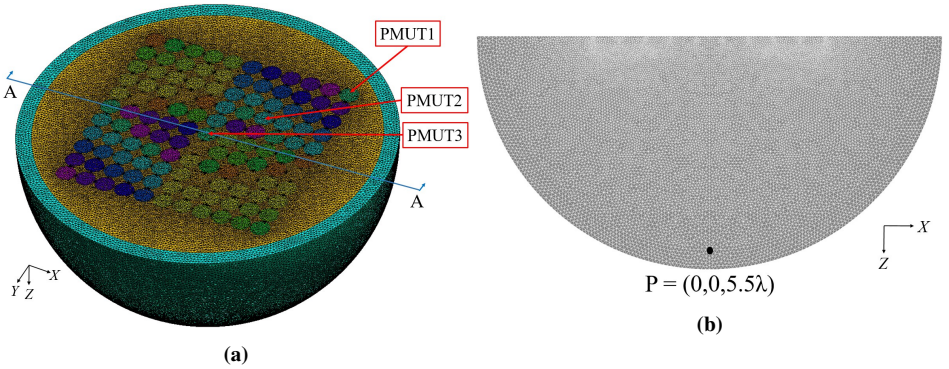

Figure 7.11: *FE fluid domain: (a) 3D view, 11x11 array of circular transducers with different colors; (b) mesh detail on the cross-section A-A, focal point P.*

focusing actuation technique has been implemented. The provided input voltage signal to the piezoelectric layers of the transducers, consists of a sinusoidal function at f_0 with 1 V amplitude, starting after a resting time t_0 in which no actuation is provided. Considering a spherical wavefront propagation generated by the oscillation of each transducers, the computation of the resting time t_0 of each PMUTs is based on the distance between the considered diaphragm center and the focal point, to achieve the situation in which every wavefronts simultaneously reach the focal point [11, 13, 14]. Indeed, the beam is focused on a neighborhood of point P depited in Fig. 7.11, at $5.5\lambda = 2.002$ mm along the vertical direction of the system passing through the center of the array.

Hereinafter, the pressure maps time sequence on the cross-section A-A cut plane passing through the center of the array presented in Fig. 7.11 are reported in Fig. 7.12.

The proposed pressure maps show a focused region around the focal point P=(0,0,5.5λ) with high concentration of pressure amplitudes. The beam pattern clearly points to the focus P. with a pressure wavefront determined by the envelop of all the wavefronts starting from each oscillating transducer. Hence the resulting bottleneck shaped pressure propagation occurs, with the tip in point P.

Furthermore, the pressure time histories at the center of PMUTs 1,2 and

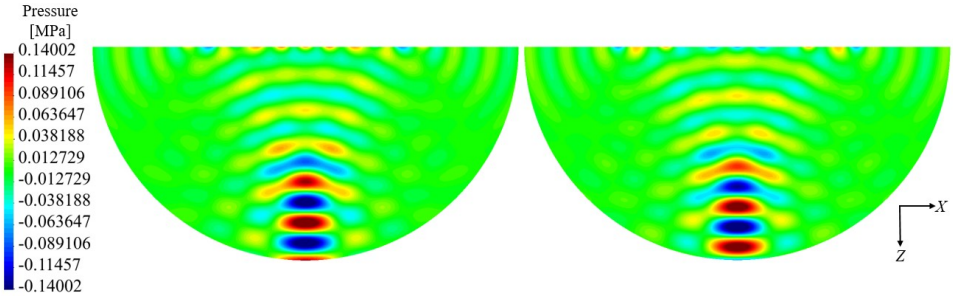

(a) $t = 2.34$ μs *(left),* $t = 2.49$ μs *(right).*

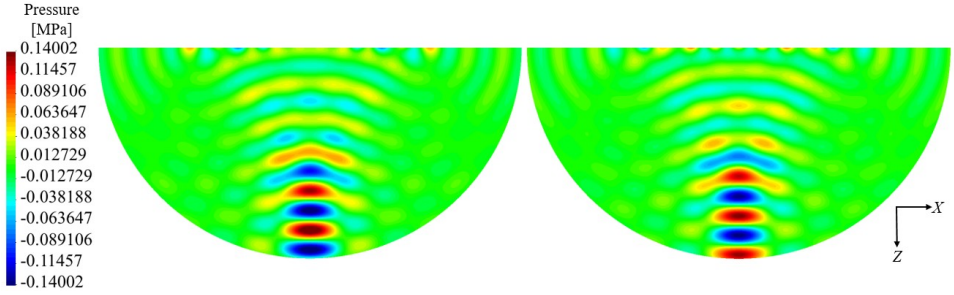

(b) $t = 2.64$ μs *(left);* $t = 2.80$ μs *(right).*

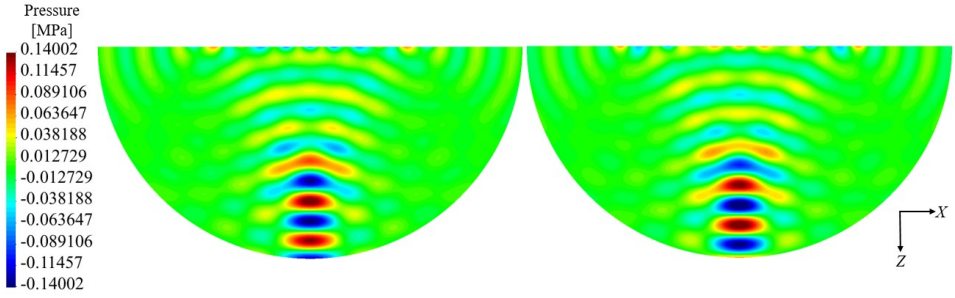

(c) $t = 2.95$ μs *(left);* $t = 3.10$ μs *(right).*

Figure 7.12: *Focused pressure beam maps at different time instants.*

3, highlighted in Fig. 7.11 are shown together with the pressure history at the focal point P (see Fig. 7.13).

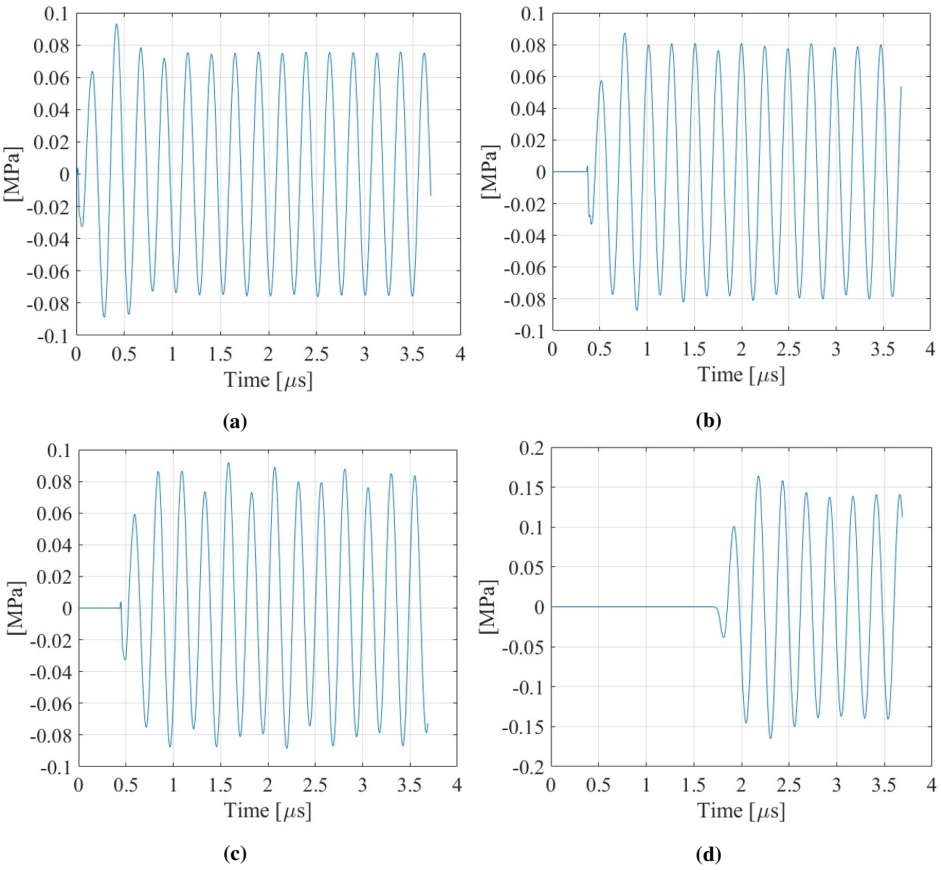

Figure 7.13: *Pressure time histories at different time points: (a) PMUT1 center, (b) PMUT2 center, (c) PMUT3 center, (d) focal point P=(0,0,5.5λ).*

The PMUTs pressure time histories are characterized by a proper resting time t_0 according to the adopted focusing technique. Indeed, PMUT1 placed at the highest distance from the focal point starts to oscillate prior to the other transducers so that no resting time is present in Fig. 7.13 (a). Furthermore, after 0.36 μs the PMUT2 vibrates, while the closest to the focus central PMUT1 oscillates with 0.44 μs later, as Fig. 7.13 (b) and (c) correctly report. Moreover, approaching the center of the array, the pressure interaction among the transducers increases. Hence, the pressure at boundary array PMUT1 tents to the stand-alone case, described in Fig. 7.7 (a) on the left, with 0.75 MPa amplitude. On the contrary, the pressure time history at PMUT3 (refer to Fig. 7.13 (c)) is strongly affected by the

pressure waves coming from the neighboring diaphragms vibration, resulting in a variational amplitude. The interaction effect is slightly present in the PMUT2 pressure history, in Fig. 7.13 (b), as well. Further, the focused pressure time history at point P, in Fig. 7.13 (d), reports a 0.14 MPa amplitude and a proper TOF of 1.79 μs corresponding to covered distance between the focus P and first oscillating diaphragm PMUT1.

The considered case study is characterized by a total number of DOFs equal to 3445745 and a computational time of about 6 hours for a time domain simulation of 3.69 μs corresponding to 15 cycles at f_0 with an integration time step of $\Delta t = 1/(128 f_0)$.

Finally, the proposed ROM can be successfully adopted to simulate the pressure radiation without any arrangement limitations for the array of transducers, considering an independent voltage input excitation for each PMUT.

7.6 7x7 PMUTs array: receiving problem

In this section, the proposed ROM code is applied to study the RX problem involving a 7x7 array of PMUTs. The proposed arrangement of diaphragms simulate the behaviour of a cluster of transducers in receiving phase, in which the scattered pressure at the PMUTs and the generated voltage at the piezoelectric electrodes, due to an incoming background pressure field, are computed.

The adopted ROM has been generated by the three axysymmetric modes reported in Fig. 7.4. Hence, the presented system consists 49 PMUTs arranged in a square array characterized by a pitch of $2\lambda/3 = 242.69$ μm and interacting with a prismatic acoustic domain with dimensions 11λx11λx5.5λ = 4.004x4.004x2.002 mm^3. In the FEM acoustic domain, a maximum element size of $\lambda/10$ has been adopted, where λ is the corresponding wavelength at the fundamental electro-mechanical frequency of the PMUT $f_0 = 4.068$ MHz (see a detailed picture in Fig. 7.14). Furthermore, as the previous 11x11 TX case, a local refinement at the PMUTs sites has been enforced, to mesh the circular acoustic-structure interfaces with an element size of $R_{PMUT}/6$.

As already mentioned in the stand-alone transducer RX problem, the adopted FEM domain configuration is justified by the reflected pressure propagation pattern generated by the hard wall conditions, on the flat surface, and the PMUTs vibration. In fact, it mainly propagates along the vertical direction $\boldsymbol{e}_3$, orthogonal to the the hard wall (O,X,Y) plane, to be absorbed by the ABC on the opposite boundary.

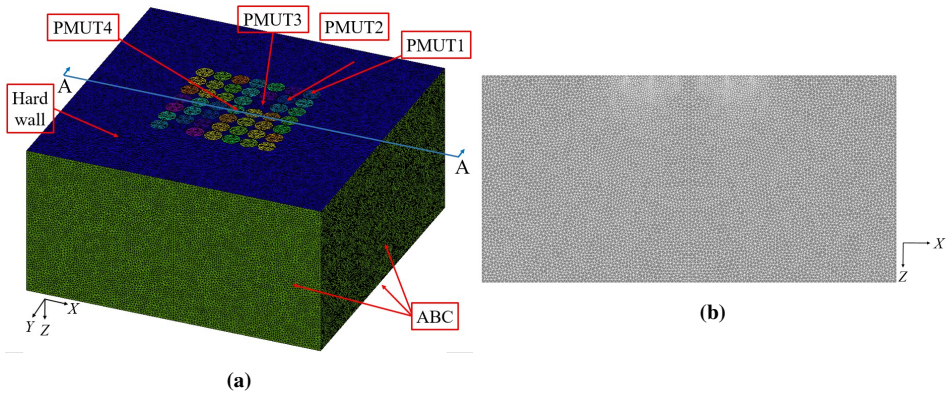

Figure 7.14: *FE fluid domain: (a) 3D view, 7x7 array of circular transducers with different colors; (b) mesh detail on the cross-section A-A.*

Considering a background incoming pressure field 7.53 with amplitude $P_{in} = 1$ MPa, travelling in direction $-\boldsymbol{e}_3$ in the acoustic domain, the scattered pressure time histories at the centers of PMUTs 1,2,3 and 4, highlighted in Fig. 7.14 are reported in Fig. 7.15 on a half diagonal.

Fig. 7.15 reports the effect of the pressure interaction in the near-field among different vibrating diaphragms. In fact, the pressure time histories show different amplitudes, depending on the position in the array. Hence, it results in the pressure amplitude of 2.50 MPa for the central PMUT4. While, the central diagonal PMUT3 and PMUT2 are respectively characterized by the pressure amplitudes of 2.72 MPa and 2.72 MPa. Approaching the array boundary, the pressure decreases and the amplitude of 2.32 MPa is predicted for the PMUT1.

Additionally, the voltage time histories on the corresponding piezoelectric electrodes are presented in Fig. 7.16.

The voltage histories show the same trend of the corresponding pressure histories. They are characterized by the in-time evolution with different amplitudes, due to the waves interaction in the near-field. Indeed, the voltage amplitude follow the same spatial dependency with respect to the transducer position on the array. Hence, the greatest voltage amplitude of 0.93 V is reported for the two central diagonal PMUT2 and PMUT3, in correspondence of the greatest pressure amplitudes. While, the values of 0.81 V is predicted for the central PMUT4 and 0.71 V for the boundary array PMUT1, according to presented the pressure values.

The described RX case study is characterized by a total number of DOFs equal to 3437515 and a computational time of about 6 hours for a time domain simulation of 3.69 μs corresponding to 15 cycles at f_0 with an

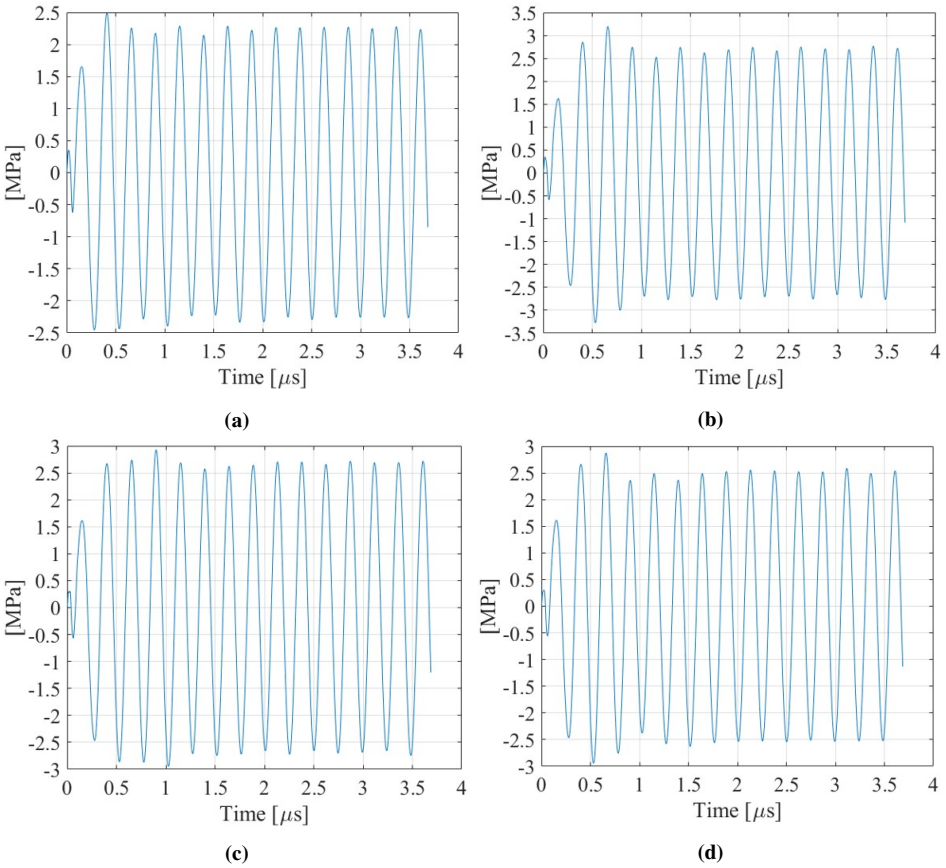

Figure 7.15: *Pressure time histories at different time points: (a) PMUT1 center, (b) PMUT2 center, (c) PMUT3 center, (d) PMUT4 center.*

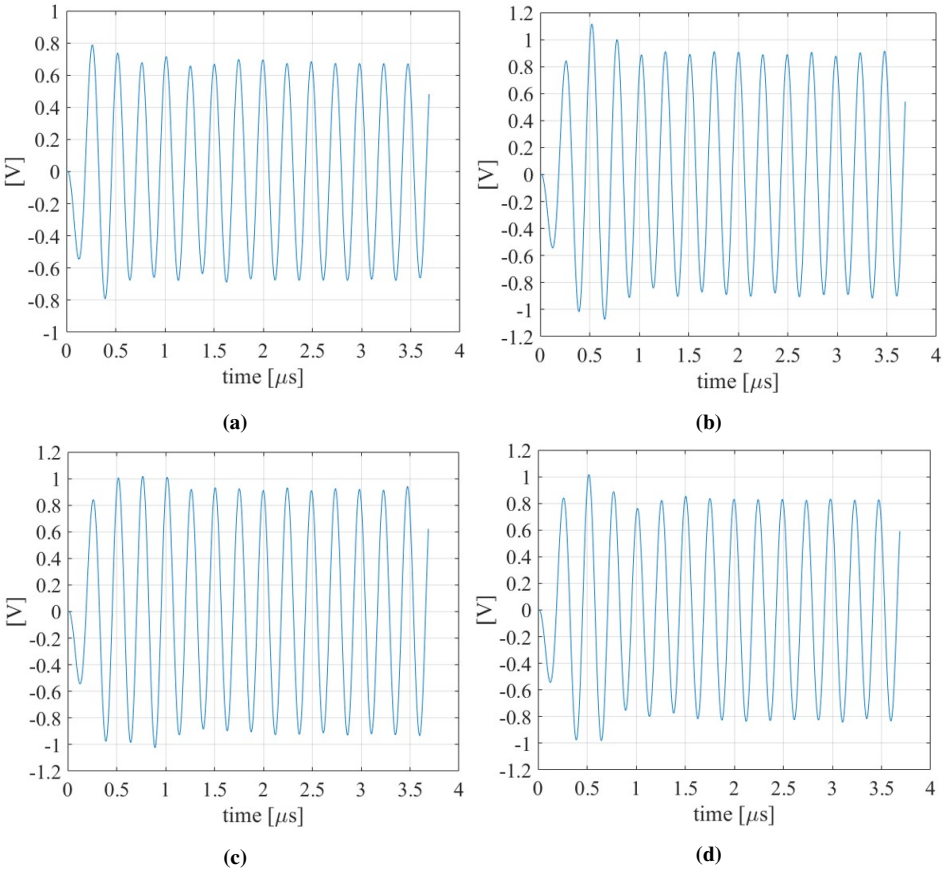

Figure 7.16: *Voltage time histories at electrodes: (a) PMUT1, (b) PMUT2, (c) PMUT3, (d) PMUT4.*

integration time step of $\Delta t = 1/(128 f_0)$.

In the end, the proposed MOR has been successfully adopted to simulate the receiving phase of a cluster of PMUTs, considering an incoming pressure plane wave propagating along the orthogonal direction of the array of transducers.

7.7 Closing remarks on the model order reduction for large array

In this chapter a novel multiphysics FE-ROM for the electro-mechanical-acoustic problem has been presented.

The solution strategy has been presented from a mathematical point of view and the involved methodology has been described. Hence, the custom code has been validated, considering the simple case of a stand-alone PMUT interacting with a water domain, in the TX and RX phases, comparing the solutions with the standard full order commercial software COMSOL Multiphysics 5.2 ones.

Moreover, the performances about the computational time have been highlighted with respect to the full order FEM approach. Hence, the proposed FE-ROM results are in very good agreement with the COMSOL ones and a faster computational time is observed.

Going further, the TX problem involving a 11x11 PMUTs arrangement has been successfully studied, applying a proper focusing actuation technique. Indeed, the pressure propagation has been focused in a neighborhood of the focal point P at 5.5λ, along the transversal vertical acoustic axis of the system, passing through the center of the array. Indeed, the pressure interaction among different transducers in the near-field has been described and the pressure history at the focus P has been predicted.

Moreover, The RX phase of a PMUTs cluster has been successfully simulated, as well. In this case a orthogonal sinusoidal incoming plane wave has been adopted as background pressure field. The voltage outputs on the piezoelectric electrodes have been computed together with the scattered pressure at the corresponding PMUTs centers, showing the near-field interaction effects.

Furthermore, the novel approach represents a suitable tool to study beamforming, focusing problems and correctly simulate the RX phase involving several PMUTs.

Additionally, the MOR technique implies a dof per selected PMUT mode, consequently the total number of dofs are basically related to the size of the FE acoustic domain and no limits in the number of transducers

occur. Moreover, the piezoelectric eigenvalue problem is solved once for all and the acoustic and piezoelectric meshes are kept independent so that the considered modes are simply mapped at the PMUTs sites, therefore the solution time hugely speeds up.

Future developments are oriented to study the acoustic cross-talk problem in the pulse-echo scenario, in which a set of transducers are driven to transmit the pressure propagation while the remaining ones are receiving the reflected pressure waves and to compute the far-field pressure response, out of the FE domain, by means of proper integral techniques.

CHAPTER 8

Conclusions and Future Work

The goal of the present work was the modelling and simulation of the PMUT devices. To this purpose the physical working principles and the state of art of this technology were initially studied and presented. Furthermore, the mathematical formulation of the coupled piezolectric-acoustic problem was derived and applied to describe the dynamical behaviour of the system in the transmitting and receiving phase. Several numerical models were proposed and built to properly study the different involved problems in the working of this innovative transducers. In Chapters 4-5-6-7 a different PMUT problem was described and solved by means of appropriate numerical techniques and models.

The response of the in-air coupled array of PMUTs was successfully analysed and compared to the stand-alone one. The presence of fabrication induced residual stresses, which determine a non-linear initial deformed configuration of the diaphragms and the a substantial fundamental mode frequency shift, was taken into account. The quality factor of the vibrating diaphragm was obtained by means of the coupled thermoacoustics-lossy pressure model, in which the dissipative fluid thermal and viscous properties were considered. The numerical results show a satisfactory agreement with the experimental data. Moreover, the 3D 4x4 numerical model

was used to carry out the acoustic analysis compared with the stand-alone transducer performance.

Several applications of this technology require the presence of a protecting structure against the external agents. To study the effects of the package on the transmitted pressure propagation, a 3D FEM model was adopted in which a linear elastic brass package was considered. Hence, the acoustic-structure interaction does not only involve the transducers but the protecting structure, as well. Hence, different holed configuration results in different pressure lobes, related to the activated package vibration modes. Therefore, the complete design of the transducer must take into account the elastic properties of the protecting structure, in accordance to the required radiation pattern and application.

The carried out experimental campaign, on the in-air PMUTs, showed the non-linear dynamic behaviour over a certain actuation voltage threshold and the influence of the DC bias voltage on the fundamental frequency and the starting performing deformed configuration. Indeed, the system vibrates in a amplitude modulation regime, in which the stiffness varies with the displacement amplitude. Two numerical models were presented to successfully solve the TX problem at two scales. The former correctly simulates the non-linear hard-spring/soft-spring behaviour of the single fluid-coupled transducer, under the effects of the residual stresses and the imposed DC bias voltage. The latter represents a good tool to simulate the array acoustic response, avoiding the long and computationally expensive non-linear transient numerical analyses. In fact, a simplified acoustic 3D model with piston-like vibrating transducers was adopted, in which the enforced input velocities time histories were extracted from the previous large displacement electro-mechanical-acoustic coupled analyses.

Ultrasound medical applications deal with large array of transducers. To properly model and simulate the in-water performance of the device, a large array analyses are required. Hence, to overcome the standard full order computational difficulties in producing solutions in a rather fast time, a novel piezoelectric-acoustic ROM was derived and implemented into a Fortran custom code, in which the dofs are basically related to the size of the acoustic FEM domain. The comparison with the standard full order FEM approach shows faster computational time and very accurate results. Indeed, the solution strategy represents a suitable technique to simulate the in-water large array behaviour in the TX and RX phases. Therefore, the 11x11 PMUTs array focusing TX and the 7x7 cluster of PMUTs RX problems were properly studied.

Summarizing, the main novelties of the presented dissertation are:

1. The simulation of the in-air dissipative electro-mechanical-thermoacoustic dynamic behaviour of the transducer with the residual stresses.
2. The study of the in-air array of PMUTs performance compared with the stand-alone transducer one.
3. The study of the effects of the protecting package structure on the performances of the in-air array of PMUTs.
4. The simulation of the non-linear dynamic behaviour of the transducer under the effects of the residual stresses, the DC bias voltage and the coupled fluid.
5. The order reduction and the simulation of the in-water large array of PMUTs problem in the TX and RX phases.

In the end, further developments and future work are related to the extension of the MOR numerical technique to the non-linear dynamic regime, to study the acoustic cross-talk problem in the combined TX-RX phase, to solve the acoustic far-field problem in the TX phase, to design a proper transducers arrangement in accordance to the required pressure propagation and application and implement the pulse-echo procedure employed in the imaging reconstruction to fully simulate the ultrasound scan.

Bibliography

[1] A. Corigliano, R. Ardito, C. Comi, A. Frangi, A. Ghisi, and S. Mariani, *Mechanics of Microsystems*. John Wiley & Sons, 2018.

[2] A. Aydemir, Y. Terzioglu, and T. Akin, "A new design and a fabrication approach to realize a high performance three axes capacitive mems accelerometer," *Sensors and Actuators A: Physical*, vol. 244, pp. 324–333, 2016.

[3] V. Zega, C. Comi, P. Minotti, G. Langfelder, L. Falorni, and A. Corigliano, "A new mems three-axial frequency-modulated (fm) gyroscope: A mechanical perspective," *European Journal of Mechanics-A/Solids*, vol. 70, pp. 203–212, 2018.

[4] B. Liang, W. Chen, Z. He, R. Yang, Z. Lin, H. Du, Y. Shang, A. Cao, Z. Tang, and X. Gui, "Highly sensitive, flexible mems based pressure sensor with photoresist insulation layer," *Small*, vol. 13, no. 44, p. 1702422, 2017.

[5] S. A. F. Farshchi Yazdi, A. Corigliano, and R. Ardito, "3-d design and simulation of a piezoelectric micropump," *Micromachines*, vol. 10, no. 4, p. 259, 2019.

[6] M. Sautto, A. S. Savoia, F. Quaglia, G. Caliano, and A. Mazzanti, "A comparative analysis of cmut receiving architectures for the design optimization of integrated transceiver front ends," *IEEE transactions on ultrasonics, ferroelectrics, and frequency control*, vol. 64, no. 5, pp. 826–838, 2017.

[7] K. Smyth, C. Sodini, and S.-G. Kim, "High electromechanical coupling piezoelectric micromachined ultrasonic transducer (PMUT) elements for medical imaging," in *TRANSDUCERS 2017 - 19th International Conference on Solid-State Sensors, Actuators and Microsystems*, pp. 966–969, 2017.

[8] G. Feng, H.-J. Liu, and G.-R. Lai, "Piezoelectric micromachined ultrasonic transducer with a universal bottom-up fabrication approach implemented on a foil as doppler radar for gesture recognition," in *2019 IEEE 32nd International Conference on Micro Electro Mechanical Systems (MEMS)*, pp. 779–782, IEEE, 2019.

[9] R. Ardito, A. Corigliano, G. Gafforelli, C. Valzasina, F. Procopio, and R. Zafalon, "Advanced model for fast assessment of piezoelectric micro energy harvesters," *Frontiers in Materials*, vol. 3, pp. 17.1–17.9, 2016.

[10] H. Trieu, G. Blume, R. Pörtner, L. von Mirbach-Wahn, N. Meyne, A. Jacob, D. V. Rojas, M. Jücker, and K. Kalaydzhyan, "Biomems for sensing in cell characterization, drug screening and biofilm detection," 2017.

[11] T. L. Szabo, *Diagnostic ultrasound imaging: inside out*. Academic Press, 2004.

[12] K. K. Shung, *Diagnostic ultrasound: Imaging and blood flow measurements*. CRC press, 2015.

[13] H. Azhari, *Basics of biomedical ultrasound for engineers*. John Wiley & Sons, 2010.

[14] S. Bhansali and A. Vasudev, *MEMS for biomedical applications*. Elsevier, 2012.

[15] T. Tani, "Crystalline-oriented piezoelectric bulk ceramics with a perovskite-type structure," *Journal of the Korean Physical Society*, vol. 32, no. 9, p. 1217, 1998.

[16] M. Lukacs, M. Sayer, and S. Foster, "Single element and linear array pzt ultrasound biomicroscopy transducers," in *1997 IEEE Ultrasonics Symposium Proceedings. An International Symposium (Cat. No. 97CH36118)*, vol. 2, pp. 1709–1712, IEEE, 1997.

[17] A. Schroth, C. Lee, S. Matsumoto, and R. Maeda, "Application of sol-gel deposited thin PZT film for actuation of 1D and 2D scanners," *Sensors and Actuators, A: Physical*, vol. 73, pp. 144–152, 1999.

[18] A. Robichaud, P.-V. Cicek, D. Deslandes, and F. Nabki, "Ultrasonic transducer for high resolution imaging," *Substance ÉTS*, 2019.

[19] Y. Lu, H.-Y. Tang, S. Fung, B. E. Boser, and D. A. Horsley, "Short-range and high-resolution ultrasound imaging using an 8 mhz aluminum nitride pmut array," in *2015 28th IEEE International Conference on Micro Electro Mechanical Systems (MEMS)*, pp. 140–143, IEEE, 2015.

[20] B. E. Eovino, Y. Liang, and L. Lin, "Concentric pmut arrays for focused ultrasound and high intensity applications," in *2019 IEEE 32nd International Conference on Micro Electro Mechanical Systems (MEMS)*, pp. 771–774, IEEE, 2019.

[21] A. Webb and G. C. Kagadis, "Introduction to biomedical imaging," *Medical Physics*, vol. 30, no. 8, pp. 2267–2267, 2003.

[22] Z. Zhou, S. Yoshida, and S. Tanaka, "Monocrystalline pmnn-pzt thin film ultrasonic rangefinder with 2 meter range at 1 volt drive," in *2017 19th International Conference on Solid-State Sensors, Actuators and Microsystems (TRANSDUCERS)*, pp. 167–170, IEEE, 2017.

[23] O. Rozen, S. Block, X. Mo, W. Bland, P. Hurst, J. Tsai, M. Daneman, R. Amirtharajah, and D. Horsley, "Monolithic MEMS-CMOS ultrasonic rangefinder based on dual-electrode PMUTs," in *Proceedings of the IEEE International Conference on Micro Electro Mechanical Systems (MEMS)*, pp. 115–118, 2016.

[24] X. Chen, J. Xu, H. Chen, H. Ding, and J. Xie, "High-accuracy ultrasonic rangefinders via pmuts arrays using multi-frequency continuous waves," *Journal of Microelectromechanical Systems*, 2019.

[25] O. Rozen, S. T. Block, X. Mo, W. Bland, P. Hurst, J. M. Tsai, M. Daneman, R. Amirtharajah, and D. A. Horsley, "Monolithic mems-cmos ultrasonic rangefinder based on dual-electrode pmuts," in *2016 IEEE 29th International Conference on Micro Electro Mechanical Systems (MEMS)*, pp. 115–118, IEEE, 2016.

[26] P. Gijsenbergh, A. Halbach, Y. Jeong, G. B. Torri, M. Billen, L. Demi, C.-H. Huang, D. Cheyns, X. Rottenberg, and V. Rochus, "Characterization of polymer-based piezoelectric micromachined ultrasound transducers for short-range gesture recognition applications," *Journal of Micromechanics and Microengineering*, vol. 29, no. 7, p. 074001, 2019.

[27] X. Jiang, Y. Lu, H. Tang, J. M. Tsai, E. J. Ng, M. J. Daneman, B. E. Boser, and D. A. Horsley, "Monolithic ultrasound fingerprint sensor," *Microsystems & nanoengineering*, vol. 3, p. 17059, 2017.

[28] Y. Lu, H. Tang, S. Fung, Q. Wang, J. Tsai, M. Daneman, B. Boser, and D. Horsley, "Ultrasonic fingerprint sensor using a piezoelectric micromachined ultrasonic transducer array integrated with complementary metal oxide semiconductor electronics," *Applied Physics Letters*, vol. 106, no. 26, p. 263503, 2015.

[29] P. Filippi, A. Bergassoli, D. Habault, and J. P. Lefebvre, *Acoustics: basic physics, theory, and methods*. Elsevier, 1998.

[30] P. M. Morse and K. U. Ingard, *Theoretical acoustics*. Princeton university press, 1986.

[31] L. L. Thompson and P. M. Pinsky, "Acoustics," *Encyclopedia of Computational Mechanics Second Edition*, pp. 1–26, 2018.

[32] M. Bruneau, *Fundamentals of acoustics*. John Wiley & Sons, 2013.

[33] G. Kline and K. Lakin, "1.0-ghz thin-film bulk acoustic wave resonators on gaas," *Applied Physics Letters*, vol. 43, no. 8, pp. 750–751, 1983.

[34] M. A. Dubois and C. Muller, "Thin-film bulk acoustic wave resonators," in *MEMS-based Circuits and Systems for Wireless Communication*, pp. 3–28, Springer, 2013.

[35] Y. Qiu, J. V. Gigliotti, M. Wallace, F. Griggio, C. E. Demore, S. Cochran, and S. Trolier-McKinstry, "Piezoelectric micromachined ultrasound transducer (pmut) arrays for integrated sensing, actuation and imaging," *Sensors*, vol. 15, no. 4, pp. 8020–8041, 2015.

[36] Y. Q. Chen, Y. X. Li, Y. Chen, Z. Y. Ju, L. Q. Tao, Y. Pang, Y. Yang, and T. l. Ren, "Large-scale and high-density pmut array based on isolated sol-gel pzt membranes for fingerprint imaging," *Journal of The Electrochemical Society*, vol. 164, no. 7, pp. B377–B381, 2017.

[37] Y. Lu and D. Horsley, "Modeling, fabrication, and characterization of piezoelectric micromachined ultrasonic transducer arrays based on cavity SOI wafers," *Journal of Microelectromechanical Systems*, vol. 24, no. 4, pp. 1142–1149, 2015.

[38] J. N. Reddy, *Mechanics of laminated composite plates and shells: theory and analysis*. CRC press, 2003.

[39] P. Muralt, N. Ledermann, J. Paborowski, A. Barzegar, S. Gentil, B. Belgacem, S. Petitgrand, A. Bosseboeuf, and N. Setter, "Piezoelectric micromachined ultrasonic transducers based on pzt thin films," *IEEE transactions on ultrasonics, ferroelectrics, and frequency control*, vol. 52, no. 12, pp. 2276–2288, 2005.

[40] L. Kinsler, A. Frey, A. Coppens, and J. Sanders, *Fundamentals of Acoustics*. John Wiley & Sons, 2000.

[41] A. S. Savoia, E. Boni, M. Sautto, F. Quaglia, B. Mauti, A. Ramalli, G. Matrone, G. Caliano, L. Fanni, F. Guanziroli, *et al.*, "A 256-element spiral cmut array with integrated analog front end and transmit beamforming circuits," in *2018 IEEE International Ultrasonics Symposium (IUS)*, pp. 206–212, IEEE, 2018.

[42] A. S. Savoia, B. Mauti, G. Caliano, L. Maiolo, A. Minotti, A. Pecora, G. Fortunato, A. Bagolini, and P. Bellutti, "Optimization of the efficiency and reliability of reverse-fabricated cmut arrays," in *2017 IEEE International Ultrasonics Symposium (IUS)*, pp. 1–4, IEEE, 2017.

[43] A. S. Savoia, B. Mauti, G. Caliano, G. Matrone, M. Piastra, R. Bardelli, F. Toia, F. Quaglia, and A. Ramalli, "A 3d packaging technology for acoustically optimized integration of 2d cmut arrays and front end circuits," in *2017 IEEE International Ultrasonics Symposium (IUS)*, pp. 1–4, IEEE, 2017.

[44] B. Shieh and E. Stride, "Development of a cmut model for non-linear actuation and contact dynamics," in *2019 IEEE International Ultrasonics Symposium (IUS)*, pp. 754–757, IEEE, 2019.

[45] A. S. 176-1987, "Ieee standard on piezoelectricity," 1987.

[46] Y. Wang, H. Ding, X. Le, W. Wang, and J. Xie, "A mems piezoelectric in-plane resonant accelerometer based on aluminum nitride with two-stage microleverage mechanism," *Sensors and Actuators A: Physical*, vol. 254, pp. 126–133, 2017.

[47] R. Ardito, E. Bertarelli, A. Corigliano, and G. Gafforelli, "On the application of piezolaminated composites to diaphragm micropumps," *Composite Structures*, vol. 99, pp. 231–240, 2013.

[48] S. Khazaaleh, N. Saeed, I. Taha, M. T. Madzik, and J. Viegas, "Piezoelectric micromachined ultrasonic transducers and micropumps: from design to optomicrofluidic applications," in *Microfluidics, BioMEMS, and Medical Microsystems XV*, vol. 10061, p. 100610S, International Society for Optics and Photonics, 2017.

[49] X. Gao, J. Wu, Y. Yu, Z. Chu, H. Shi, and S. Dong, "Giant piezoelectric coefficients in relaxor piezoelectric ceramic pnn-pzt for vibration energy harvesting," *Advanced Functional Materials*, vol. 28, no. 30, p. 1706895, 2018.

[50] H. Kuttruff, *Room acoustics*. Crc Press, 2016.

[51] G. Massimino, "Modellazione e simulazione di un micro trasduttore ultrasonico piezoelettrico," *Politecnico di Milano, Italy*, 2016.

[52] M. Bonnet, A. Frangi, and C. Rey, *The finite element method in solid mechanics*. 2014.

[53] J. J. Bernstein, "Acoustic transducer," Sept. 8 1992. US Patent 5,146,435.

[54] H. Gao, P. Gijsenbergh, S. Mao, A. Halbach, Y. Jeong, D. Cheyns, X. Rottenberg, and V. Rochus, "Reconstructing mid-air acoustic holograms using pmut arrays: a simulation study," in *2019 20th International Conference on Thermal, Mechanical and Multi-Physics Simulation and Experiments in Microelectronics and Microsystems (EuroSimE)*, pp. 1–4, IEEE, 2019.

[55] W. Liu, L. He, X. Wang, J. Zhou, W. Xu, N. Smagin, M. Toubal, H. Yu, Y. Gu, J. Xu, *et al.*, "3d fem analysis of high-frequency aln-based pmut arrays on cavity soi," *Sensors*, vol. 19, no. 20, p. 4450, 2019.

[56] K. Smyth, C. Sodini, and S.-G. Kim, "High electromechanical coupling piezoelectric micromachined ultrasonic transducer (pmut) elements for medical imaging," in *2017 19th International Conference on Solid-State Sensors, Actuators and Microsystems (TRANSDUCERS)*, pp. 966–969, IEEE, 2017.

[57] S. Sadeghpour, M. Kraft, and R. Puers, "Pmuts array with dynamic directivity: A study of its underwater acoustic power intensity," in *2018 IEEE International Ultrasonics Symposium (IUS)*, pp. 1–9, IEEE, 2018.

[58] S. Akhbari, A. Voie, Z. Li, B. Eovino, and L. Lin, "Dual-electrode bimorph pmut arrays for handheld therapeutic medical devices," in *2016 IEEE 29th International Conference on Micro Electro Mechanical Systems (MEMS)*, pp. 1102–1105, IEEE, 2016.

[59] A. Guedes, S. Shelton, R. Przybyla, I. Izyumin, B. Boser, and D. Horsley, "Aluminum nitride pmut based on a flexurally-suspended membrane," in *2011 16th International Solid-State Sensors, Actuators and Microsystems Conference*, pp. 2062–2065, IEEE, 2011.

[60] R. J. Przybyla, S. E. Shelton, A. Guedes, I. I. Izyumin, M. H. Kline, D. A. Horsley, and B. E. Boser, "In-air rangefinding with an aln piezoelectric micromachined ultrasound transducer," *IEEE Sensors Journal*, vol. 11, no. 11, pp. 2690–2697, 2011.

[61] O. Rozen, S. T. Block, S. E. Shelton, R. J. Przybyla, and D. A. Horsley, "Air-coupled aluminum nitride piezoelectric micromachined ultrasonic transducers at 0.3 mhz to 0.9 mhz," in *2015 28th IEEE International Conference on Micro Electro Mechanical Systems (MEMS)*, pp. 921–924, IEEE, 2015.

[62] R. Bashir and A. Kabir, "High sensitivity micro-machined pressure sensors and acoustic transducers," Jan. 11 2000. US Patent 6,012,335.

[63] X. Chen, C. Liu, D. Yang, X. Liu, L. Hu, and J. Xie, "Highly accurate airflow volumetric flowmeters via pmuts arrays based on transit time," *Journal of Microelectromechanical Systems*, 2019.

[64] B. E. Eovino, Y. Liang, S. Akhbari, and L. Lin, "A single-chip flow sensor based on bimorph pmuts with differential readout capabilities," in *2018 IEEE Micro Electro Mechanical Systems (MEMS)*, pp. 1084–1087, IEEE, 2018.

[65] C. H. Huang, L. Demi, G. Torri, S. Mao, M. Billen, Y. Jeong, D. Cheyns, X. Rottenberg, V. Rochus, and C. Hsien, "Display compatible pmut device for mid air ultrasound gesture recognition," in *11th Annual TechConnect World Innovation Conference and Expo, Held Jointly with the 20th Annual Nanotech Conference and Expo, the 2018 SBIR/STTR Spring Innovation Conference, and the Defense TechConnect DTC Spring Conference*, pp. 161–164, TechConnect, 2018.

[66] S. Alasatri, L. Rufer, and J. E.-Y. Lee, "Aln-on-si square diaphragm piezoelectric micromachined ultrasonic transducer with extended range of detection," in *Multidisciplinary Digital Publishing Institute Proceedings*, vol. 2, p. 913, 2018.

[67] G. Massimino, L. D'Alessandro, F. Procopio, R. Ardito, M. Ferrera, and A. Corigliano, "Air-coupled PMUT at 100 kHz with PZT active layer and residual stresses: Multiphysics model and experimental validation," in *18th International Conference on Thermal, Mechanical and Multi-Physics Simulation and Experiments in Microelectronics and Microsystems, EuroSimE 2017*, p. 7926253, 2017.

[68] A. Vidoni, "Studio e progettazione di un amplificatore cmos a basso rumore per sistemi ecografici con pmut (piezoelectric micromachined ultrasonic transducers)," 2019.

[69] G. Lu, H. Dong, J. Chen, and J. Cheng, "Enhanced dielectric and ferroelectric properties of pzt thin films derived by an ethylene glycol modified sol–gel method," *Journal of Sol-Gel Science and Technology*, vol. 82, no. 2, pp. 530–535, 2017.

[70] D. Seregin, K. Vorotilov, A. Sigov, and N. Kotova, "Porous pzt films prepared by pvp assisted sol-gel process," *Ferroelectrics*, vol. 484, no. 1, pp. 43–48, 2015.

[71] Y. Cui, W. Gu, X. Kong, Z. Gao, and S. Yu, "Study of acetic acid addition on properties of pzt films prepared by sol–gel method," *Journal of Materials Science: Materials in Electronics*, vol. 30, no. 10, pp. 9194–9199, 2019.

[72] G. Massimino, A. Colombo, L. D'Alessandro, F. Procopio, R. Ardito, M. Ferrera, and A. Corigliano, "Multiphysics modelling and experimental validation of an air-coupled array of pmuts with residual stresses," *Journal of Micromechanics and Microengineering*, vol. 28, no. 5, p. 054005, 2018.

[73] G. Massimino, L. D'Alessandro, F. Procopio, R. Ardito, M. Ferrera, and A. Corigliano, "Multiphysics analysis and experimental validation of an air coupled piezoelectric micromachined ultrasonic transducer with residual stresses," *Procedia Engineering*, vol. 168, pp. 852–855, 2016.

[74] M. Malinen, M. Lyly, P. Råback, A. Kärkkäinent, and L. Kärkkäinen, "A finite element method for the modeling of thermo-viscous effects in acoustics," in *ECCOMAS 2004 - European Congress on Computational Methods in Applied Sciences and Engineering*, 2004.

[75] W. Beltman, P. Van Der Hoogt, R. Spiering, and H. Tijdeman, "Implementation and experimental validation of a new viscothermal acoustic finite element for acousto-elastic problems," *Journal of Sound and Vibration*, vol. 216, no. 1, pp. 159–178, 1998.

[76] K. Suzuki, Y. Nakayama, N. Shimizu, and T. Mizuno, "Study on wide-band piezoelectric micro-machined ultrasound transducers (pmut) by combined resonance frequencies and controlling poling directions," in *2018 IEEE International Ultrasonics Symposium (IUS)*, pp. 1–3, IEEE, 2018.

[77] C. Sun, Q. Shi, M. S. Yazici, T. Kobayashi, Y. Liu, and C. Lee, "Investigation of broadband characteristics of multi-frequency piezoelectric micromachined ultrasonic transducer (mf-pmut)," *IEEE Sensors Journal*, vol. 19, no. 3, pp. 860–867, 2018.

[78] K. Park, H. Lee, P. Crisman, M. Kupnik, O. Oralkan, and B. Khuri-Yakub, "Optimum design of circular CMUT membranes for high quality factor in air," in *Proceedings - IEEE Ultrasonics Symposium*, pp. 504–507, 2008.

[79] R. Ardito, L. D'Alessandro, G. Massimino, F. Procopio, and A. Corigliano, "Multiphysics analyses of the effect of package on the performances of PMUT transducers," in *Proceedings - Coupled Problems*, 2017.

[80] X. Jiang, H. Y. Tang, Y. Lu, X. Li, J. M. Tsai, E. J. Ng, M. J. Daneman, M. Lim, F. Assaderaghi, B. E. Boser, *et al.*, "Monolithic 591× 438 dpi ultrasonic fingerprint sensor," in *2016 IEEE 29th International Conference on Micro Electro Mechanical Systems (MEMS)*, pp. 107–110, IEEE, 2016.

[81] Y. Lu, H. Tang, S. Fung, Q. Wang, J. Tsai, M. Daneman, B. Boser, and D. Horsley, "Ultrasonic fingerprint sensor using a piezoelectric micromachined ultrasonic transducer array integrated with complementary metal oxide semiconductor electronics," *Applied Physics Letters*, vol. 106, no. 26, p. 263503, 2015.

[82] X. Jiang, H. Y. Tang, Y. Lu, E. J. Ng, J. M. Tsai, M. J. Daneman, B. E. Boser, and D. A. Horsley, "Inter-element coupling effects in pulse-echo ultrasonic fingerprint sensors," in *2017 IEEE 30th International Conference on Micro Electro Mechanical Systems (MEMS)*, pp. 1192–1195, IEEE, 2017.

[83] S. Sadeghpour, B. Lips, M. Kraft, and R. Puers, "Flexible soi-based piezoelectric micromachined ultrasound transducer (pmut) arrays," in *2019 20th International Conference on Solid-State Sensors, Actuators and Microsystems & Eurosensors XXXIII (TRANSDUCERS & EUROSENSORS XXXIII)*, pp. 250–253, IEEE, 2019.

[84] T. Wang, T. Kobayashi, B. Yang, H. Wang, and C. Lee, "Highly sensitive piezoelectric micromachined ultrasonic transducer (pmut) operated in air," in *2016 IEEE 11th Annual International Conference on Nano/Micro Engineered and Molecular Systems (NEMS)*, pp. 294–299, IEEE, 2016.

[85] C. Y. Cheng, A. Dangi, L. Ren, S. Tiwari, R. R. Benoit, Y. Qiu, H. S. Lay, S. Agrawal, R. Pratap, S.-R. Kothapalli, *et al.*, "Thin film pzt-based pmut arrays for deterministic particle manipulation," *IEEE transactions on ultrasonics, ferroelectrics, and frequency control*, vol. 66, no. 10, pp. 1606–1615, 2019.

[86] Y. Lu and D. A. Horsley, "Modeling, fabrication, and characterization of piezoelectric micromachined ultrasonic transducer arrays based on cavity soi wafers," *Journal of Microelectromechanical Systems*, vol. 24, no. 4, pp. 1142–1149, 2015.

[87] A. B. Amar, H. Cao, and A. B. Kouki, "Modeling and process design optimization of a piezoelectric micromachined ultrasonic transducers (pmut) using lumped elements parameters," *Microsystem Technologies*, vol. 23, no. 10, pp. 4659–4669, 2017.

[88] L. Sarkar, J. Joseph, S. G. Singh, and S. R. K. Vanjari, "Modeling and fabrication aspects of pvdf as a membrane material for air borne pmut applications," in *2018 IEEE SENSORS*, pp. 1–4, IEEE, 2018.

[89] Q. Zhu, T. Chen, H. Liu, L. Sun, T. Wang, C. Lee, X. Le, and J. Xie, "An aln-based piezoelectric micro-machined ultrasonic transducer (pmut) array," in *2016 IEEE 16th International Conference on Nanotechnology (IEEE-NANO)*, pp. 731–734, IEEE, 2016.

[90] N. Joly, "Finite element modeling of thermoviscous acoustics in closed cavities," in *Acoustics' 08 Paris*, pp. 2469–2474, 2008.

[91] P. B. Muller and H. Bruus, "Numerical study of thermoviscous effects in ultrasound-induced acoustic streaming in microchannels," *Physical Review E*, vol. 90, no. 4, p. 043016, 2014.

[92] E. Ledesma, V. Tzanov, I. Zamora, F. Torres, A. Uranga, N. Barniol, E. Marigó, and M. Soundara-Pandian, "Aln pmut with crossed-cavity for better acoustic pressure outputs in liquid at high frequency," in *2019 20th International Conference on Solid-State Sensors, Actuators and Microsystems & Eurosensors XXXIII (TRANSDUCERS & EUROSENSORS XXXIII)*, pp. 825–828, IEEE, 2019.

[93] D. A. Horsley, Y. Lu, H. Y. Tang, X. Jiang, B. E. Boser, J. M. Tsai, E. J. Ng, and M. J. Daneman, "Ultrasonic fingerprint sensor based on a pmut array bonded to cmos circuitry," in *2016 IEEE International Ultrasonics Symposium (IUS)*, pp. 1–4, IEEE, 2016.

[94] P. Fedeli, M. Kamlah, and A. Frangi, "Phase-field modeling of domain evolution in ferroelectric materials in the presence of defects," *Smart Materials and Structures*, vol. 28, 01 2019.

[95] S. Akhbari, F. Sammoura, S. Shelton, C. Yang, D. Horsley, and L. Lin, "Highly responsive curved aluminum nitride pmut," in *2014 IEEE 27th International Conference on Micro Electro Mechanical Systems (MEMS)*, pp. 124–127, IEEE, 2014.

[96] R. O. Cleveland, P. V. Chitnis, and S. R. McClure, "Acoustic field of a ballistic shock wave therapy device," *Ultrasound in medicine & biology*, vol. 33, no. 8, pp. 1327–1335, 2007.

[97] P. T. Christopher and K. J. Parker, "New approaches to the linear propagation of acoustic fields," *The Journal of the Acoustical Society of America*, vol. 90, no. 1, pp. 507–521, 1991.

[98] R. Ohayon and C. Soize, *Structural acoustics and vibration: Mechanical models, variational formulations and discretization*. Elsevier, 1997.

[99] K. Been, J. Lee, and W. Moon, "Helmholtz-kirchhoff integral formula for predicting the acoustic pressure from a radiator including irregular surface," *The Journal of the Acoustical Society of America*, vol. 146, no. 4, pp. 3074–3074, 2019.

[100] Y. Kusano, Q. Wang, G.-L. Luo, Y. Lu, R. Q. Rudy, R. G. Polcawich, and D. A. Horsley, "Effects of dc bias tuning on air-coupled pzt piezoelectric micromachined ultrasonic transducers," *Journal of Microelectromechanical Systems*, vol. 27, no. 2, pp. 296–304, 2018.

[101] S. Akhbari, F. Sammoura, C. Yang, M. Mahmoud, N. Aqab, and L. Lin, "Bimorph pmut with dual electrodes," in *2015 28th IEEE International Conference on Micro Electro Mechanical Systems (MEMS)*, pp. 928–931, IEEE, 2015.

[102] Q. Wang and D. A. Horsley, "Using a mutual acoustic impedance model to improve the time domain response of pmut arrays," in *2017 IEEE International Ultrasonics Symposium (IUS)*, pp. 1–4, IEEE, 2017.

[103] Q. Xu and D. Lai, "Piezoelectric micromachined ultrasonic transducers: Modeling and simulation of structural parameters on transmitting performance," in *2015 IEEE Advanced Information Technology, Electronic and Automation Control Conference (IAEAC)*, pp. 648–652, IEEE, 2015.

[104] S. Tiwari and R. N. Candler, "Using flexural mems to study and exploit nonlinearities: a review," *Journal of Micromechanics and Microengineering*, vol. 29, no. 8, p. 083002, 2019.

[105] M. Singha and R. Daripa, "Nonlinear vibration and dynamic stability analysis of composite plates," *Journal of Sound and Vibration*, vol. 328, no. 4-5, pp. 541–554, 2009.

[106] G. Massimino, A. Colombo, R. Ardito, F. Quaglia, F. Foncellino, and A. Corigliano, "Air-coupled array of pmuts at 100 khz with pzt active layer: Multiphysics model and experiments," in *2019 20th International Conference on Thermal, Mechanical and Multi-Physics Simulation and Experiments in Microelectronics and Microsystems (EuroSimE)*, pp. 1–5, IEEE, 2019.

[107] M. Amabili, *Nonlinear vibrations and stability of shells and plates*. Cambridge University Press, 2008.

[108] S. Kattimani and M. Ray, "Control of geometrically nonlinear vibrations of functionally graded magneto-electro-elastic plates," *International Journal of Mechanical Sciences*, vol. 99, pp. 154–167, 2015.

[109] M. Ducceschi and C. Touzé, "Modal approach for nonlinear vibrations of damped impacted plates: Application to sound synthesis of gongs and cymbals," *Journal of Sound and Vibration*, vol. 344, pp. 313–331, 2015.

[110] M. Liu and D. G. Gorman, "Formulation of rayleigh damping and its extensions," *Computers & structures*, vol. 57, no. 2, pp. 277–285, 1995.

[111] J.-S. Chen, W.-C. Ro, and J.-S. Lin, "Exact static and dynamic critical loads of a sinusoidal arch under a point force at the midpoint," *International Journal of Non-Linear Mechanics*, vol. 44, no. 1, pp. 66–70, 2009.

[112] L. Cedolin *et al.*, *Stability of structures: elastic, inelastic, fracture and damage theories*. World Scientific, 2010.

[113] G. J. Simitses, *Dynamic stability of suddenly loaded structures*. Springer Science & Business Media, 2012.

[114] A. H. Nayfeh and D. T. Mook, *Nonlinear oscillations*. John Wiley & Sons, 2008.

[115] A. Frangi and G. Gobat, "Reduced order modelling of the non-linear stiffness in mems resonators," *International Journal of Non-Linear Mechanics*, vol. 116, pp. 211–218, 2019.

[116] A. A. Muravyov and S. A. Rizzi, "Determination of nonlinear stiffness with application to random vibration of geometrically nonlinear structures," *Computers & Structures*, vol. 81, no. 15, pp. 1513–1523, 2003.

[117] L. Campos, "On linear and non-linear wave equations for the acoustics of high-speed potential flows," *Journal of sound and vibration*, vol. 110, no. 1, pp. 41–57, 1986.

[118] M. F. Hamilton, D. T. Blackstock, *et al.*, *Nonlinear acoustics*, vol. 237. Academic press San Diego, 1998.

[119] M. I. Younis, *MEMS linear and nonlinear statics and dynamics*, vol. 20. Springer Science & Business Media, 2011.

[120] M. I. Younis and A. Nayfeh, "A study of the nonlinear response of a resonant microbeam to an electric actuation," *Nonlinear Dynamics*, vol. 31, no. 1, pp. 91–117, 2003.

[121] R. Mestrom, R. Fey, J. Van Beek, K. Phan, and H. Nijmeijer, "Modelling the dynamics of a mems resonator: simulations and experiments," *Sensors and Actuators A: Physical*, vol. 142, no. 1, pp. 306–315, 2008.

[122] S. Krylov, B. R. Ilic, and S. Lulinsky, "Bistability of curved microbeams actuated by fringing electrostatic fields," *Nonlinear Dynamics*, vol. 66, no. 3, p. 403, 2011.

[123] R. Heuer, "Large flexural vibrations of thermally stressed layered shallow shells," *Nonlinear Dynamics*, vol. 5, no. 1, pp. 25–38, 1994.

[124] V. Zega, G. Langfelder, L. G. Falorni, and C. Comi, "Hardening, softening, and linear behavior of elastic beams in mems: An analytical approach," *Journal of Microelectromechanical Systems*, vol. 28, no. 2, pp. 189–198, 2019.

[125] M. I. Younis, H. M. Ouakad, F. M. Alsaleem, R. Miles, and W. Cui, "Nonlinear dynamics of mems arches under harmonic electrostatic actuation," *Journal of Microelectromechanical Systems*, vol. 19, no. 3, pp. 647–656, 2010.

[126] C. Touzé, O. Thomas, and A. Chaigne, "Hardening/softening behaviour in non-linear oscillations of structural systems using non-linear normal modes," *Journal of Sound and Vibration*, vol. 273, no. 1-2, pp. 77–101, 2004.

[127] R. Heuer, H. Irschik, and F. Ziegler, "Multi-modal approach for large natural flexural vibrations of thermally stressed plates," *Nonlinear Dynamics*, vol. 1, no. 6, pp. 449–458, 1990.

[128] M. Rafiee, X. He, and K. Liew, "Non-linear dynamic stability of piezoelectric functionally graded carbon nanotube-reinforced composite plates with initial geometric imperfection," *International Journal of Non-Linear Mechanics*, vol. 59, pp. 37–51, 2014.

[129] H. Farokhi and M. H. Ghayesh, "Nonlinear mechanics of electrically actuated microplates," *International Journal of Engineering Science*, vol. 123, pp. 197–213, 2018.

[130] R. Batra, M. Porfiri, and D. Spinello, "Vibrations of narrow microbeams predeformed by an electric field," *Journal of Sound and Vibration*, vol. 309, no. 3-5, pp. 600–612, 2008.

[131] M. Sathyamoorthy, "Nonlinear vibration analysis of plates: a review and survey of current developments," 1987.

[132] H. M. Ouakad and M. I. Younis, "The dynamic behavior of mems arch resonators actuated electrically," *International Journal of Non-Linear Mechanics*, vol. 45, no. 7, pp. 704–713, 2010.

[133] A. Leissa and A. Kadi, "Curvature effects on shallow shell vibrations," *Journal of Sound and Vibration*, vol. 16, no. 2, pp. 173–187, 1971.

[134] L. Librescu, "Refined geometrically nonlinear theories of anisotropic laminated shells," *Quarterly of Applied Mathematics*, vol. 45, no. 1, pp. 1–22, 1987.

[135] C. Y. Chia, "Geometrically nonlinear behavior of composite plates: a review," 1988.

[136] A. Dangi, S. Agrawal, S. Tiwari, S. Jadhav, C. Cheng, G. R. Datta, S. Trolier-McKinstry, R. Pratap, and S.-R. Kothapalli, "Ring pmut array based miniaturized photoacoustic endoscopy device," in *Photons Plus Ultrasound: Imaging and Sensing 2019*, vol. 10878, p. 1087811, International Society for Optics and Photonics, 2019.

[137] J. Kusch, G. M. Flockhart, R. Bauer, and D. Uttamchandani, "Application of mems enabled excitation and detection schemes to photoacoustic imaging," in *2019 20th International Conference on Solid-State Sensors, Actuators and Microsystems & Eurosensors XXXIII (TRANSDUCERS & EUROSENSORS XXXIII)*, pp. 829–832, IEEE, 2019.

[138] D. H. Evans and W. N. McDicken, *Doppler ultrasound: physics, instrumentation and signal processing*. John Wiley & Sons, 2000.

[139] F. V. Pop, B. Herrera, C. Cassella, G. Chen, E. Demirors, R. Guida, T. Melodia, and M. Rinaldi, "Novel pmut-based acoustic duplexer for underwater and intrabody communication," in *2018 IEEE International Ultrasonics Symposium (IUS)*, pp. 1–4, IEEE, 2018.

[140] W. Lee, S. Yoo, J. Jung, W. Kang, W. Wang, C. Moon, and H. Choi, "All-in-one low-intensity pulsed ultrasound stimulation system using piezoelectric micromachined ultrasonic transducer (pmut) arrays for targeted cell stimulation," *Biomedical microdevices*, vol. 19, no. 4, p. 86, 2017.

[141] J. Ling, Y. H. Wei, G. Y. Jiang, Y. Q. Chen, H. Tian, Y. Yang, and T. L. Ren, "Piezoelectric micromachined ultrasonic transducers for ultrasound imaging," in *2018 IEEE International Conference on Electron Devices and Solid State Circuits (EDSSC)*, pp. 1–2, IEEE, 2018.

[142] Y. Lu, H. Tang, Q. Wang, S. Fung, J. Tsai, M. Daneman, B. Boser, and D. Horsley, "Waveguide piezoelectric micromachined ultrasonic transducer array for short-range pulse-echo imaging," *Applied Physics Letters*, vol. 106, no. 19, p. 193506, 2015.

[143] H. Ding, S. Akhbari, B. E. Eovino, Y. Wu, J. Xie, and L. Lin, "Ultrasonic imaging of muscle-like phantoms using bimorph pmuts toward wearable muscle disorder diagnost ics," in *2018 IEEE Micro Electro Mechanical Systems (MEMS)*, pp. 396–399, IEEE, 2018.

[144] S. H. Chang, F. T. Wang, J. K. Wu, S. N. Shevtsov, I. V. Zhilyaev, and M. S. Shevtsova, "The multiobjective design optimization of pmut hydrophone," in *Applied Mechanics and Materials*, vol. 727, pp. 660–665, Trans Tech Publ, 2015.

[145] E. Ledesma, I. Zamora, F. Torres, A. Uranga, V. Tzanov, N. Barniol, E. Marigó, and M. Soundara-Pandian, "Squared pmut with enhanced pressure sensitivities," in *Multidisciplinary Digital Publishing Institute Proceedings*, vol. 2, p. 925, 2018.

[146] J. Li, W. Ren, G. Fan, and C. Wang, "Design and fabrication of piezoelectric micromachined ultrasound transducer (pmut) with partially-etched zno film," *Sensors*, vol. 17, no. 6, p. 1381, 2017.

[147] J. M. L. Tsai and M. Daneman, "Integrated piezoelectric microelectromechanical ultrasound transducer (pmut) on integrated circuit (ic) for fingerprint sensing," Dec. 10 2015. US Patent App. 14/829,404.

[148] H. Tang, Y. Lu, S. Fung, J. Tsai, M. Daneman, D. Horsley, and B. Boser, "Pulse-echo ultrasonic fingerprint sensor on a chip," in *2015 Transducers-2015 18th International Conference on Solid-State Sensors, Actuators and Microsystems (TRANSDUCERS)*, pp. 674–677, IEEE, 2015.

[149] H. Tang, Y. Lu, X. Jiang, E. J. Ng, J. M. Tsai, D. A. Horsley, and B. E. Boser, "3-d ultrasonic fingerprint sensor-on-a-chip," *IEEE Journal of Solid-State Circuits*, vol. 51, no. 11, pp. 2522–2533, 2016.

[150] M. Yaacob, M. Arshad, and A. A. Manaf, "Modeling of circular piezoelectric micro ultrasonic transducer using cual 10 ni 5 fe 4 on zno film for sonar applications," *Acoustical Physics*, vol. 57, no. 2, p. 151, 2011.

[151] M. Yaacob, M. Arshad, A. Manaf, and M. Rahman, "200 khz pmut using pzt on pdms membrane for sonar applications," in *Intelligent and Advanced Systems (ICIAS), 2012 4th International Conference on*, vol. 2, pp. 572–575, 2012.

[152] M. Yaacob, M. Arshad, A. Manaf, M. Rahman, and S. Samsuri, "Programmable pulse forming network for pmut underwater calibration in compact acoustic tank,"

[153] Z. Wang, Y. Luo, G. Zhao, B. Q. Xu, and F.-G. Yuan, "Design of an orthotropic piezoelectric composite material phased array transducer for damage detection in a concrete structure," *Research in Nondestructive Evaluation*, vol. 27, no. 4, pp. 204–215, 2016.

[154] X. Yu, Z. Fan, S. Puliyakote, and M. Castaings, "Remote monitoring of bond line defects between a composite panel and a stiffener using distributed piezoelectric sensors," *Smart Materials and Structures*, vol. 27, no. 3, p. 035014, 2018.

[155] J. Rao, M. Ratassepp, D. Lisevych, M. Hamzah Caffoor, and Z. Fan, "On-line corrosion monitoring of plate structures based on guided wave tomography using piezoelectric sensors," *Sensors*, vol. 17, no. 12, p. 2882, 2017.

[156] V. Y. Senyurek, A. Baghalian, S. Tashakori, D. McDaniel, and I. N. Tansel, "Localization of multiple defects using the compact phased array (cpa) method," *Journal of Sound and Vibration*, vol. 413, pp. 383–394, 2018.

[157] C. J. Borigo, S. E. Owens, and J. L. Rose, "Piezoelectric shear rings for omnidirectional shear horizontal guided wave excitation and sensing," Mar. 6 2018. US Patent 9,910,016.

[158] Z. Wang, Y. Luo, and T. Sun, "Design and validation of an orthotropic piezoelectric composite material phased array sensor used to nondestructive detection," *Sensor Letters*, vol. 13, no. 10, pp. 852–856, 2015.

[159] X. Dai, S. Gao, K. Pan, J. Zhu, and H. F. Rashvand, "Wireless piezoelectric sensor systems for defect detection and localization," in *Wireless Sensor Systems for Extreme Environments: Space, Underwater, Underground and Industrial*, pp. 201–219, John Wiley & Sons, 2017.

[160] C. Sun, Q. Shi, M. Yazici, C. Lee, and Y. Liu, "Development of a highly sensitive humidity sensor based on a piezoelectric micromachined ultrasonic transducer array functionalized with graphene oxide thin film," *Sensors*, vol. 18, no. 12, p. 4352, 2018.

[161] J. A. Jensen, *Estimation of blood velocities using ultrasound: a signal processing approach*. Cambridge University Press, 1996.

[162] Q. Li, J. Xing, D. Shang, and Y. Wang, "A flow velocity measurement method based on a pvdf piezoelectric sensor," *Sensors*, vol. 19, no. 7, p. 1657, 2019.

[163] D. P. Lannes, A. L. Gama, and T. F. B. Bento, "Measurement of flow rate using straight pipes and pipe bends with integrated piezoelectric sensors," *Flow Measurement and Instrumentation*, vol. 60, pp. 208–216, 2018.

[164] P. D. Corl, "Ultrasound catheter for imaging and blood flow measurement," Oct. 12 2017. US Patent App. 15/631,663.

[165] D. A. Horsley, R. J. Przybyla, M. H. Kline, S. E. Shelton, A. Guedes, O. Izyumin, and B. E. Boser, "Piezoelectric micromachined ultrasonic transducers in consumer electronics: The next little thing?," in *2016 IEEE 29th International Conference on Micro Electro Mechanical Systems (MEMS)*, pp. 145–148, IEEE, 2016.

[166] M. Chevrier and M. Weitz, "Single transceiver ultrasonic flow meter having an array of transducer elements," Feb. 23 2016. US Patent 9,267,829.

[167] H. Peters, N. Kessissoglou, and S. Marburg, "Modal decomposition of exterior acoustic-structure interaction problems with model order reduction," *The Journal of the Acoustical Society of America*, vol. 135, no. 5, pp. 2706–2717, 2014.

[168] Y. Chen, G. Huang, X. Zhou, G. Hu, and C.-T. Sun, "Analytical coupled vibroacoustic modeling of membrane-type acoustic metamaterials: Membrane model," *The Journal of the Acoustical Society of America*, vol. 136, no. 3, pp. 969–979, 2014.

[169] R. Ohayon and C. Soize, "Advanced computational dissipative structural acoustics and fluid-structure interaction in low-and medium-frequency domains. reduced-order models and uncertainty quantification," 2012.

[170] H. Ammari *et al.*, *Mathematical Modeling in Biomedical Imaging*. Springer, 2009.

[171] C. H. Nguyen, U. Hanke, and E. Halvorsen, "Constitutive equations of piezoelectric layered beams with interdigitated electrodes," *IEEE transactions on ultrasonics, ferroelectrics, and frequency control*, vol. 65, no. 9, pp. 1680–1694, 2018.

[172] J. Cao, M. Ling, D. J. Inman, and J. Lin, "Generalized constitutive equations for piezo-actuated compliant mechanism," *Smart Materials and Structures*, vol. 25, no. 9, p. 095005, 2016.

[173] M. Rao, S. Tarun, R. Schmidt, and K. Schröder, "Finite element modeling and analysis of piezo-integrated composite structures under large applied electric fields," *Smart Materials and Structures*, vol. 25, no. 5, p. 055044, 2016.

[174] P. Hess, "On the eigenvalue problem for weakly coupled elliptic systems," *Archive for Rational Mechanics and Analysis*, vol. 81, no. 2, pp. 151–159, 1983.

[175] S. Lychev, A. Manzhirov, and S. V. Joubert, "Closed solutions of boundary-value problems of coupled thermoelasticity," *Mechanics of solids*, vol. 45, no. 4, pp. 610–623, 2010.

[176] R. S. Cantrell and K. Schmitt, "On the eigenvalue problem for coupled elliptic systems," *SIAM journal on mathematical analysis*, vol. 17, no. 4, pp. 850–862, 1986.

[177] M. Ochmann and F. Mechel, "Analytical and numerical methods in acoustics," in *Formulas of acoustics*, pp. 930–1023, Springer, 2004.

[178] R. Citarella and L. Federico, "Advances in vibroacoustics and aeroacustics of aerospace and automotive systems," 2018.

[179] C. Soize, "Uncertainty quantification in computational structural dynamics and vibroacoustics," in *Uncertainty Quantification*, pp. 155–216, Springer, 2017.

[180] A. Van De Walle, "Parallel time-domain simulations for vibro-acoustics using krylov subspace projections and linear-phase filters," in *INTER-NOISE and NOISE-CON Congress and Conference Proceedings*, vol. 253, pp. 349–360, Institute of Noise Control Engineering, 2016.

[181] E. Creixell Mediante, J. S. Jensen, J. Brunskog, and M. Larsen, "Reduced order modeling in topology optimization of vibroacoustic problems," *The Journal of the Acoustical Society of America*, vol. 141, no. 5, pp. 4035–4035, 2017.

[182] J.-F. Deü, W. Larbi, R. Ohayon, and R. Sampaio, "Piezoelectric shunt vibration damping of structural-acoustic systems: finite element formulation and reduced-order model," *Journal of Vibration and Acoustics*, vol. 136, no. 3, p. 031007, 2014.

[183] S. Marburg and B. Nolte, *Computational acoustics of noise propagation in fluids: finite and boundary element methods*, vol. 578. Springer, 2008.

[184] J. F. Deü, W. Larbi, and R. Ohayon, "Structural-acoustic vibration reduction using piezoelectric shunt techniques: Fe formulation and reduced order model," in *Proc. of the 3rd International Conference on Computational Methods in Structural Dynamics and Earthquake Engineerin, COMPDYN*, pp. 25–28, 2011.

[185] U. Hetmaniuk, R. Tezaur, and C. Farhat, "Review and assessment of interpolatory model order reduction methods for frequency response structural dynamics and acoustics problems," *International Journal for Numerical Methods in Engineering*, vol. 90, no. 13, pp. 1636–1662, 2012.

[186] R. S. Puri, D. Morrey, A. J. Bell, J. F. Durodola, E. B. Rudnyi, and J. G. Korvink, "Reduced order fully coupled structural–acoustic analysis via implicit moment matching," *Applied Mathematical Modelling*, vol. 33, no. 11, pp. 4097–4119, 2009.

[187] D. Bortz, A. Rubio, H. Banks, A. Cain, and R. Smith, "Reduced order modeling in control of open cavity acoustics," tech. rep., 2000.

[188] B. K. Kim and J.-G. Ih, "On the reconstruction of the vibro-acoustic field over the surface enclosing an interior space using the boundary element method," *The Journal of the Acoustical Society of America*, vol. 100, no. 5, pp. 3003–3016, 1996.

[189] M. Fischer and L. Gaul, "Fast bem–fem mortar coupling for acoustic–structure interaction," *International Journal for Numerical Methods in Engineering*, vol. 62, no. 12, pp. 1677–1690, 2005.

[190] P. Banerjee, S. Ahmad, and H. Wang, "A new bem formulation for the acoustic eigenfrequency analysis," *International Journal for Numerical Methods in Engineering*, vol. 26, no. 6, pp. 1299–1309, 1988.

[191] T. Ha Duong, B. Ludwig, and I. Terrasse, "A galerkin bem for transient acoustic scattering by an absorbing obstacle," *International Journal for Numerical Methods in Engineering*, vol. 57, no. 13, pp. 1845–1882, 2003.

[192] D. Fritze, S. Marburg, and H.-J. Hardtke, "Fem–bem-coupling and structural–acoustic sensitivity analysis for shell geometries," *Computers & structures*, vol. 83, no. 2-3, pp. 143–154, 2005.

[193] A. Nandy, S. Mullick, S. De, and D. Datta, "Numerical simulation of ultrasonic wave propagation in flawed domain," *National Siminar & Exhibition on NDE, India*, 2009.

[194] Z. You, M. Lusk, R. Ludwig, and W. Lord, "Numerical simulation of ultrasonic wave propagation in anisotropic and attenuative solid materials," *IEEE transactions on ultrasonics, ferroelectrics, and frequency control*, vol. 38, no. 5, pp. 436–445, 1991.

[195] R. Lerch and W. Friedrich, "Ultrasound fields in attenuating media," *The Journal of the Acoustical Society of America*, vol. 80, no. 4, pp. 1140–1147, 1986.